Theoretical Studies of Optical Metamaterials

Jianji Yang

UNIVERSITÉ PARIS XI

UFR SCIENTIFIQUE D'ORSAY

École Doctorale Ondes et Matières

Laboratoire Charles Fabry

THÈSE

Présentée pour obtenir le grade de

DOCTEUR EN SCIENCES DE

L'UNIVERSITÉ PARIS-SUD XI

Spécialité : Optique et Photonique

par

Jianji YANG (杨建基)

Theoretical studies of optical fishnet metamaterials

Soutenue le 14 Septembre 2012 devant la commission d'examen composée de:

M.	Stéphane	COLLIN	Membre invité
M.	Julien	DE LA GORGUE DE ROSNY	
M.	Philippe	LALANNE	Directeur de thèse
M.	Didier	LIPPENS	
M.	Luis	MARTIN-MORENO	Rapporteur
M.	Christophe	SAUVAN	Co-encadrant invité
M.	Jean-Claude	WEEBER	Rapporteur
M.	Saïd	ZOUHDI	

Table of content

Acknowledgements

First and foremost, I am deeply grateful to my advisors Dr. Philippe Lalanne and Dr. Christophe Sauvan, under whose patient guidance my work has been moving forward in the right direction.

I also would like to thank Dr. Jean-Paul Hugonin, who is an excellent expert of computational electrodynamics, for his generous technical support in my PhD work.

I am also thankful to Prof. Haitao Liu at University of Nankai, Dr. Stéphane Collin and Dr. Jean-Luc Pelouard at Laboratoire de Photonique et de Nanostructures (LPN-CNRS), Prof. Falk Lederer and Prof. Carsten Rockstuhl at the University of Jena for their collaboration and input.

I learned enormously from other members of the Nanophotonics and Electromagnetism Group, particularly those who I have worked or discussed with: Dr. Wojciech Smigaj, Anthony Jouanin, Dr. Yvan Maksymov, Dr. Choonhow Gan, Dr. Age Biehs and Dr. Nir Dahan.

I would like to thank the committee members for comments.

Thanks to all my Chinese friends, as they share with me many happy moments during these years.

Finally, I thank my parents, Pengwei and Gang, my brother Jiandu and other family members. Without their love and support, I would have never finished the journey of a Ph.D. candidate.

Jianji YANG (**杨建基**),

Palaiseau, July 2012

Introduction

Physicist Richard Feynman gave a remarkable talk in 1959 [Gil61], entitled ''*there's plenty of room at the bottom*'', during which he foresaw that the manipulation of objects at the atomic or molecular scale will be realized and mentioned some possible physical effects related to this amazing advancement. After this visionary idea, Norio Taniguchi defined in the 1970s, for the first time, the term 'nanotechnology' [Tan74]. Then, with the emergence of scanning tunneling microscopes and microelectronics, all the ingredients were gathered for the development of nanotechnology and nanoscience in the 1980s. Since then, micro and nanofabrication processes have experiences a continuing growth. After first applications in electronics, nanotechnology provides today various applications in all domains of fundamental and applied science, including optics and optoelectronics. This particular sub-field of photonics, studying light propagation at the scale of a few tens of nanometers, is named as *nanophotonics*.

The control and manipulation of electromagnetic waves at the micro to nanometer scale can be realized by artificially structuring the materials with characteristic dimensions smaller than the wavelength. As a special class of structured electromagnetic materials, *metamaterials* exhibit new electromagnetic properties that cannot be found in natural materials. Indeed, the accessible values of material parameters ε_r (electric permittivity) and μ_r (magnetic permeability) in nature are highly limited. In particular, at optical frequencies, large positive values of ε_r are uncommon (but appealing for many applications), and the permeability is equal to unity, $\mu_r = 1$, for any natural material. There are some fundamental physical constraints accounting for these limitations, see for instance [Lan60, Jac98]. However, as argued by many researchers [Pen99, Mer09], these constraints could be overcome in the case of composite structures based on mesoscopic (intermediate scale between the wavelength and the atomic size) unit cells. Those arguments in fact provide a theoretical basis to the unusual properties of electromagnetic

metamaterials. The most emblematic is perhaps the realization of a negative refractive index, which may enable the development of new imaging systems with a resolution that could beat the diffraction limit [Pen00].

Negative-index metamaterials have been originally demonstrated in the microwaves [She01]. After these first achievements, people immediately tried to take advantage of the invariance of Maxwell equations when the wavelength and the structures size are both scaled the same way. Metallic split ring resonators (SRRs), the meta-atoms imagined for microwave frequencies [Pen99], were thus scaled down to a scale of a few tens of nanometer [Kat05, Kle06, Liu08a, Ser09]. However, although Maxwell equations do not depend on the wavelength, provided that the objects are scaled accordingly, the optical properties of metals do. As a consequence, at high frequencies such as visible and near-infrared, the magnetic response of SRRs degrades [Zho05, Ish05, Lin06, Pen10]. This failure can be understood as a combination of several factors: the high absorption losses, the strong dispersion of the metal permittivity and the fact that at least one dimension of the SRR becomes now comparable with the skin depth in the metal (several tens of nanometers).

As a consequence of these theoretical difficulties, to which technological issues can be added, novel designs had to be proposed for pushing negative-index metamaterials toward optical frequencies. Most of the new geometries that have been proposed to meet this goal were imagined with the same conceptual guideline that gave birth to SRRs: to realize a small resonant structure in which a current loop can be induced by the incident light – the signature of a magnetic response. The validity of this current loop picture can probably be questioned at optical frequencies, but one cannot deny that such concepts, inspired by the only work by J. Pendry on SRRs [Pen99], allowed one to imagine innovative designs for negative-index metamaterials working at high frequencies. The so-called fishnet structure is one of them [Zha05, Dol07, Val08], which consists of a periodic stack of metallic and dielectric layer perforated by an array of holes. Fishnet metamaterials can be regarded as promising candidates for realizing negative refraction at optical frequencies, since broadband negative refractive indices with reasonably low losses have been reproducibly demonstrated by several groups for bulky fishnet structures with multiple functional layers [Val08, Cha11, Gar11]. It is clear that, even if the picture of independent current loops acting as magnetic dipoles has lead to imagine

the fishnet geometry, one has to go beyond this concept to get a quantitative picture of light propagation inside a fishnet metamaterial. Indeed, the meta-atoms composing the fishnet are connected and their interaction should be taken into account to understand the optical response of the whole structure. In addition, these meta-atoms are only slightly subwavelength and considering a fishnet metamaterial as a homogeneous effective medium can reasonably be called into question.

In this thesis, we go beyond the usual concepts of meta-atoms and homogenization with the objective to improve the understanding of light propagation in negative-index fishnet metamaterials. We try to answer the following questions that are of major importance for the development of negative refractive indices at optical frequencies: (1) How does light propagate inside a fishnet metamaterial and scatter at its interface with a positive-index material? (2) How do this propagation and this scattering compare to those of a homogeneous medium and what can we learn from this comparison concerning homogenization? (3) What is the physical origin of negative index in the fishnet metamaterial? (4) How can one engineer the properties of fishnet metamaterials accurately? (5) Although negative-index fishnet metamaterials exhibit relatively low losses, can we further reduce them for practical applications?

The aim of this thesis is to address those questions with an emphasis on physics of optical fishnet metamaterials. In particular, we have derived an accurate semi-analytical model for the effective index of fishnets, which constitutes an important breakthrough in the modeling of optical metamaterials. The thesis can be divided into four parts.

In the *first* part (Chapter 2), we study the light scattering at an interface between a uniform half-space (air for instance) and a semi-infinite periodic photonic structure (a fishnet metamaterial for instance). With a three-dimensional (3D) fully-vectorial method, we calculate the scattering coefficients of the interface and evidence that, for some design, the energy transport inside the metamaterial can be due to a single mode, the fundamental Bloch mode supported by the periodic structure. Based on the knowledge of the single-interface scattering coefficients and of the effective index n_{eff} of the fundamental Bloch mode, we propose an innovative method for retrieving the effective optical parameters of the metamaterial. The

approach emphasizes the key role played by the fundamental Bloch mode and provides retrieved parameters that are more accurate or stable than those obtained by classical methods based only on far-field quantities, i.e. light reflection and transmission through finite-thickness metamaterial slabs.

Because of the importance of the fundamental Bloch mode in the light transport inside metamaterials, in the *second* part (Chapter 3), we derive closed-form expressions for the scattering coefficients (r and t) at an interface between two periodic media. This is a computationally demanding problem that can be lifted only with powerful numerical tools, and it is of major importance to derive accurate approximate expressions. In the derivation that relies on the Bloch mode orthogonality, we assume that only the fundamental Bloch modes of the two periodic media are known, all higher-order Bloch modes being unknown. Under the hypothesis that the two periodic media have only slightly different geometrical parameters, we show that the closed-form expressions are very accurate for various geometries, including dielectric waveguides and metallic metamaterials. They can thus be used with confidence for designing and engineering stacks of periodic structures.

As shown in the first part, the fundamental Bloch mode fully determines the optical property of fishnet metamaterials. In the *third* part (Chapters 4 and 5), we derive an accurate semi-analytical model for the fundamental Bloch mode of fishnets, which quantitatively predicts the effective index (including both the real-negative and imaginary parts). The model is based on the analysis of the energy flow through the fishnet mesh. This flow is supported by two perpendicular arrays of plasmonic waveguides and we track the plasmonic modes as they propagate and scatter in the structure. Since our approach obviously handles elementary processes that take place at a scale smaller than the metamaterial period, we describe our model as *microscopic*. The model explicitly shows that the origin of a broad-band negative index in fishnets can be mainly understood as the result of the resonant excitation of plasmonic modes propagating transversally along the dielectric layers. These modes present an anti-symmetric electric field distribution that recalls the current loop picture [Mar08]. The model goes beyond the simple picture since it quantifies the resonance and highlights the geometrical parameters that impact it. Finally, we extend the semi-analytical model to the important problem of loss-compensation

with gain media. We show that with a moderate gain, the absorption losses in the metamaterial can be almost completely compensated, leaving the negative real part of the effective index unchanged. Another salient feature of the model is that, as there are only a few free physical parameters in it, it allows for an easy and precise geometrical tailoring of the fishnet without resorting to cumbersome full-wave calculations.

As evidenced by the microscopic model, it is the "magnetic" resonance of plasmons in Metal-Insulator-Metal structures that creates the negative index of fishnet metamaterials. In the *fourth* part (Chapter 6), we study the asymptotic behavior of 3D Metal-Insulator-Metal nanoresonators as the resonator size is shrunk to very small dimensions well below the diffraction limit. In particular, we show that the quality factor of the resonance increases from 10 to 100 when the resonator volume is scaled from $(\lambda/2n^{\dagger})^3$ to $(\lambda/50)^3$ in the quasi-static regime. We provide a comprehensive study of the resonance scaling with a semi-analytical Fabry-Perot model. The latter quantitatively predicts the absorption and radiation losses of the nanoresonator and provides an in-depth understanding of the resonance lifetime that cannot be obtained with brute-force computations. In particular, it highlights the impact of slow-wave effects on the quality factor as the size of the resonator is decreased. The model remains accurate over the whole size scale even in the quasi-static regime for which retardation effects are not expected. This important and counterintuitive result indicates that both strongly localized resonances in plasmonic nanoparticles and delocalized resonance in elongated plasmonic nanowires can be possibly understood under the same conceptual umbrella, a wave-retardation based antenna problem.

†: *n denotes the refractive index of the dielectric spacer in MIM resonators*.

This work has been partly published in the following references:

[1] J. Yang, C. Sauvan, T. Paul, C. Rockstuhl, F. Lederer and P. Lalanne, ''Retrieving the effective parameters of metamaterials from the single interface scattering problem'', Appl. Phys. Lett. **97**, 061102 (2010).

[2] J. Yang, C. Sauvan, H.T. Liu and P. Lalanne, ''Theory of fishnet negative-index optical metamaterials'', Phys. Rev. Lett. **107**, 043903 (2011).

[3] W. Śmigaj, P. Lalanne, J. Yang, T. Paul, C. Rockstuhl and F. Lederer, ''Closed-form

expression for the scattering coefficients at an interface between two periodic media'', Appl. Phys. Lett. **98**, 111107(2011).

[4] J. Yang, C. Sauvan, P. Lalanne and H.T. Liu, ''Bloch modes of optical fishnets'', Proc. SPIE **8070**, 807006 (2011).

[5] J. Yang, C. Sauvan, A. Jouanin, S. Collin, J.-L. Pelouard and P. Lalanne, ''Ultrasmall metal-insulator-metal nanoresonators: impact of slow-wave effects on the quality factor'', Opt. Express **20**, 16880-16891 (2012)

Chapter 1

Introduction to metamaterials

Materials with various exotic electromagnetic characteristics have been extensively studied in past decades in order to satisfy the growing interest in different fields including imaging, telecommunication, energy-harnessing and so on. As an especially promising candidate, electromagnetic metamaterials exhibit electromagnetic properties that are not available in naturally occurring materials. Metamaterials gain their remarkable properties from artificially structuring at the subwavelength scale, not directly from the constituent materials. Numerous tempting effects and applications related with metamaterials have been investigated, including negative refraction [Sha07], intense optical activities in chiral metamaterials [Pap03], invisibility cloaks [Pen06] and perfect lens [Pen00]. With many favorable properties, the concept of metamaterials has been also extended to research areas outside electromagnetism, like acoustics [Fan06, Zha11] or mechanics [Kad12].

In this thesis I particularly focus on developing theories for optical (visible and near-infrared) negative index metamaterials (with effective refractive index $n_{\text{eff}} < 0$). This chapter introduces the basic concepts and the underlying fundamental electromagnetic theory. Also, an overview of the whole thesis is provided at the end.

1.1 Maxwell equations and material parameters

Within the framework of classical electrodynamics, which was established by James Clerk Maxwell [Max73], the interaction of electromagnetic fields with matter is described by *macroscopic* Maxwell equations in time domain [Jac98]:

$$\nabla\times\mathbf{E}(\boldsymbol{r}, t)= -\partial\mathbf{B}(\boldsymbol{r}, t)/\partial t, \tag{1-1a}$$

$$\nabla\times\mathbf{H}(\boldsymbol{r}, t)= \partial\mathbf{D}(\boldsymbol{r}, t)/\partial t + \mathbf{J}_f(\boldsymbol{r}, t), \tag{1-1b}$$

$$\nabla\bullet\mathbf{B}(\boldsymbol{r}, t)= 0, \tag{1-1c}$$

$$\nabla\bullet\mathbf{D}(\boldsymbol{r}, t)= \rho_f(\boldsymbol{r}, t), \tag{1-1d}$$

where $\mathbf{E}(\boldsymbol{r}, t)$ is the electric field and $\mathbf{B}(\boldsymbol{r}, t)$ is the magnetic induction. $\mathbf{J}_f(\boldsymbol{r}, t)$ and $\rho_f(\boldsymbol{r}, t)$ are the density of free electric currents and charges, respectively. For a *linear homogeneous* material, the electric displacement $\mathbf{D}(\boldsymbol{r}, t)$ and the magnetic field $\mathbf{H}(\boldsymbol{r}, t)$ are related to $\mathbf{E}(\boldsymbol{r}, t)$ and $\mathbf{B}(\boldsymbol{r}, t)$ via simple constitutive relations:

$$\mathbf{D}(\boldsymbol{r}, t)= \varepsilon_0\mathbf{E}(\boldsymbol{r}, t) + \mathbf{P}(\boldsymbol{r}, t)=\varepsilon_0\varepsilon_r\mathbf{E}(\boldsymbol{r}, t), \tag{1-2a}$$

$$\mathbf{B}(\boldsymbol{r}, t)= \mu_0\mathbf{H}(\boldsymbol{r}, t) + \mu_0\mathbf{M}(\boldsymbol{r}, t)=\mu_0\mu_r\mathbf{H}(\boldsymbol{r}, t), \tag{1-2b}$$

where ε_0 and μ_0 denote the vacuum electric permittivity and magnetic permeability. The material is characterized by the relative electric permittivity tensor ε_r and relative magnetic permeability μ_r, which are defined from the electric polarization $\mathbf{P}(\boldsymbol{r}, t)$ and the magnetization $\mathbf{M}(\boldsymbol{r}, t)$. It is usually assumed that the electric quadrupole moment and even higher order electric or magnetic moments are negligible compared with electric dipole moment and magnetic dipole moment. In fact (1-2a) and (1-2b) contain this assumption implicitly.

The set of *macroscopic* Maxwell equations in Eq. (1-1) can be deduced starting from procedures of averaging *microscopic* quantities. $\mathbf{E}(\boldsymbol{r}, t)$, $\mathbf{B}(\boldsymbol{r}, t)$, $\mathbf{P}(\boldsymbol{r}, t)$ and $\mathbf{M}(\boldsymbol{r}, t)$ are obtained by averaging their *microscopic* counterparts — *microscopic* electric and magnetic fields, and *microscopic* electric and magnetic dipoles — on an intermediate scale that is much greater than the spacing between the *microscopic* particles (atoms and molecules), yet still much smaller than the wavelength of the corresponding electromagnetic wave. The detailed derivation of *macroscopic* Maxwell equations

from *microscopic* equations can be found in classical textbooks, see for example [Jac98]. What is important to keep in mind is that, the *macroscopic* material parameters ε_r and μ_r, defined in Eqs. (1-2a) and (1-2b), are obtained by averaging the *microscopic* electromagnetic multipole moments.

The accessible values of material parameters ε_r and μ_r in nature are highly limited. In particular at optical frequencies, large positive ε_r is uncommon (but appealing for many applications), and $\mu_r = 1$ for any natural material. There are some physical constraints accounting for that. The fact that electric permittivity ε_r tends to unity when the frequency ω increases can be understood easily: when the field varies rapidly in time, the polarization process that is responsible for a non-unitary ε_r cannot happen at all. Additionally, the relative permeability μ_r of common materials is restricted by the lack of high frequency magnetic response of materials. This effect is examined by Landau quantitatively [Lan60]. However, this may not be the case for composite structures based on mesoscopic unit cells, as argued by many researchers [Pen99, Mer09]. Those arguments in fact provide a sound theoretical basis for electromagnetic metamaterials.

To summarize this section, the constituent parameters of natural electromagnetic materials derive from the averaged response of atoms or molecules to external field. What is more, those parameters are highly limited by physical constraints, particularly at optical frequencies. This is the impetus for intensive investigations on structured artificial materials.

1.2 Structured electromagnetic materials: metamaterials

1.2.1 *Development of structured electromagnetic materials*

Structured electromagnetic materials that offer special optical properties are a rather broad concept and they are actually not rare. A famous instance is butterfly wings, which are iridescent due to interferences in the tree-like nanostructures covering the wings [Vuk03], see Fig. 1-1(a). Additionally, it is also well-known that people have utilized structured electromagnetic materials for long time, though unaware of the underlying physical mechanisms. Metallic nanoparticles were used by the Roman craftsmen to color glass. A fantastic example is the Lycurgus Cup, which looks red [Fig. 1-1 (b)i] for illumination from inside and green [Fig. 1-1(b) ii]

for illumination from outside [Leo07, Web01]. This peculiar behavior results from gold and silver nanoparticles embedded in the glass.

From the 19th century people started to study artificial electromagnetic materials systematically [Fru23, Str87, Eme97]. An outstanding achievement is the photonic crystals firstly proposed by E. Yablonovith and S. John independently, as inspired by the semiconductor physics. The proposal states that photons in dielectric periodic structures can behave in analogy to electrons in semiconductors, allowing unprecedented manipulation of photons [Yab87, Joh87]. Since then much progress has been made in this field [Yab91, Kra96, Mei99, Rus03, Bab08, Joa08]. *A remark must be made here, that the size of unit cell in photonic crystals is usually on the wavelength scale, while the unit cell in metamaterials is in principle much smaller than the wavelength.*

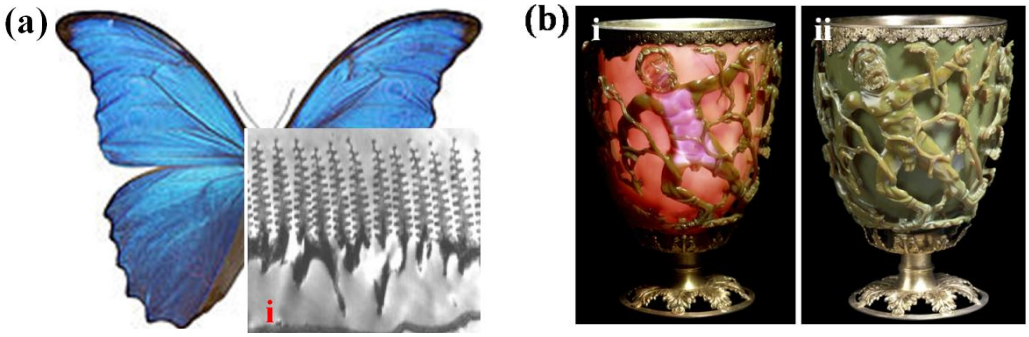

Figure 1-1. (**a**) One of the most iridescent butterflies: Morpho Rhetenor [Web02]. The inset shows the transmission electron micrograph (TEM) images of wing-scale cross-sections of this butterfly [Vuk03]. (**b**) The image of Lycurgus Cup that exhibits dichroism [Web01].

1.2.2 *Metamaterials*

With the fast development of nano/micrometric fabrication technologies, the recently emerging metamaterials have triggered tremendous effort in looking for extraordinary electromagnetic properties. *On the contrary to photonic crystals, metamaterials are constructed by subwavelength functional inclusions.* With those mesoscopic units, metamaterials can in principle remove the constraints on the relative permittivity ε_r and relative permeability μ_r that limit the properties of natural materials. Metamaterials are usually realized by assembling small electromagnetic resonators in subwavelength-scale periodicity lattices. Around the

resonant frequency, electric and magnetic responses of the resonators result in exotic macroscopic material parameters. The unit cells of metamaterials are often referred to as metaatoms, by analogy with atoms in natural materials.

The exact electromagnetic response of metamaterials to external excitation has to be obtained using a fully-vectorial solver of Maxwell equations. However, in order to gain more physical insight, it is always beneficial to describe the optical properties of metamaterials in a similar manner as the natural media, i.e., in terms of macroscopic effective optical parameters such as the refractive index n, the electric permittivity ε_r, and the magnetic permeability μ_r. In principle those effective parameters allow people to consider the composite materials as a homogeneous medium that can reproduce the same optical response as the actual structured material. The derivation of macroscopic effective parameters (n_{eff}, ε_{eff}, μ_{eff} …) of a composite is called homogenization. Researchers have proposed several different homogenization methods, relaying on field averaging [Smi06], Bloch mode approaches [Zha06, Roc08, Śmi08, Yan10], multipole expansion [Pet08, Vyn09], inversion of scattering parameters (S-parameters) [Smi02, Kos05]. In this work, we also contribute to the homogenization of metamaterials, see Chapter 2 and 4.

An important goal of metamaterial studies is to look for artificial materials with a negative refractive index ($n_{eff} < 0$). Negative-index materials could allow the creation of superlens [Pen00], which may have sub-diffraction-limited resolutions. It should be clarified that in this work, the concept of metamaterials *completely excludes* the composite materials that are adopted in the field of *transformation optics* [Leo06, Pen06], which possesses permittivity and permeability varying continuously in space. In the field of *transformation optics*, the functional devices or materials are not necessarily based on subwavelength resonators as ''classical'' metamaterials.

1.3 A brief history of negative refractive-index metamaterials

1.3.1 *Negative refraction and the perfect lens*

In 1967, Veselago proposed the concept of a medium with both negative permittivity ε_r and negative permeability μ_r [Ves68]. He found that the refractive index of this medium $n = (\varepsilon_r \mu_r)^{1/2}$ is surprisingly negative also! By applying macroscopic Maxwell

equations to this negative index medium, he predicted a series of interesting and unusual electrodynamics phenomenon: such as negative refraction [Fig. 1-2(a)], reversed Cerenkov radiation and reversed Doppler shift [Mar08a]. In negative index media, the electric field vector **E**, magnetic field vector **H** and wave vector ***k*** follow a left-handed triplet [Fig. 1-2(b)], in contrast to conventional medium in which **E**, **H** and ***k*** comprise a right-handed triplet. This is why negative index media are also called left-handed media. The Poynting vector **S** associated to the plane wave in left-handed medium is anti-parallel to the wave vector ***k***. So negative index media are also called backward-wave media sometimes.

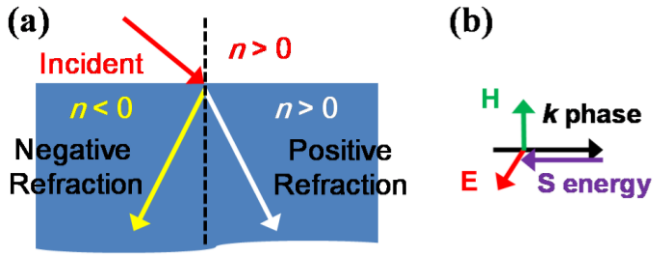

Figure 1-2. (**a**) Comparison between negative refraction and conventional (positive) refraction phenomenon. Negative (positive) refraction occurs at interfaces between materials at which one has an ordinary positive phase velocity (refractive index $n > 0$), and the other has the negative (positive) phase velocity with $n < 0$ ($n > 0$). (**b**) In negative index materials, the electric field vector **E**, magnetic field vector **H** and wave vector ***k*** form a left-handed triplet. The wave vector ***k*** and poyting vector **S** are anti-parallel.

What is more, based on negative refraction, Veselago further and for the first time proposed a novel type of lens made of a flat slab consisting of a medium with $\varepsilon_r = \mu_r = -1$, see Fig. 1-3. This lens directs all the rays originating from the object to the focus. Note that the separation between object and focus is twice the lens thickness. Because of the lack of any realistic medium with $\varepsilon_r = \mu_r = -1$, Veselago's paper was unnoticed for almost 30 years.

Recently in a seminal paper [Pen00], Pendry reconsidered the Veselago flat lens with an isotropic materials $\varepsilon_r = \mu_r = -1$ (refractive index $n = -1$). He surprisingly showed that the light transmission of the radiation from an object is unity for all Fourier components, even including evanescent waves that carry the information of high spatial frequency. In other words, this flat lens can in principle form a perfect image of a point source. Now the flat lens with $\varepsilon_r = \mu_r = -1$ can be possibly realized since the development of negative-index metamaterials [Smi00]. This perfect lens

proposal is one of the emblematic applications that initiated the research field of metamaterials.

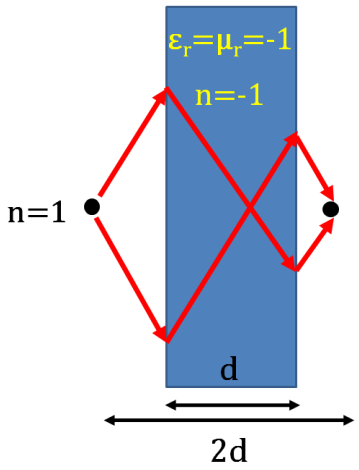

Figure 1-3. A flat lens made of a negative refractive index material with $n = -1$ ($\varepsilon_r = \mu_r = -1$) suspended in air ($n = 1$). As mentioned by Veselago [Ves68], an image is formed as all the light rays originating from an object are refocused on the other side of the slab. Later J. Pendry found that this lens can form a perfect image of a point source [Pen00].

1.3.2 *Ingredients for realizing a negative refractive index*

There was basically no progress on negative refraction until J. Pendry et al. [Pen99] and D. Smith et al. [Smi00, She01] published seminal papers to claim the creation of artificial material with simultaneously negative permittivity ε_r and permeability μ_r. Those remarkable advancements drew a lot of interest and provided a rich ground for not only theoretical but also experimental researches, thanks to the tremendous development of micro- and nano-technologies in past decades. The key to realize negative index is to make the material to exhibit both negative ε_r and negative μ_r effectively. The first negative-index metamaterial consisted in an ensemble of an array of metallic wires, which supports negative permittivity, and an array of split-ring resonators that offers negative permeability [She01, Pen99]. The working principles of those two types of functional inclusions are presented in this subsection.

***Diluted Metal* (*negative permittivity*)**. In nature any good conductive metal has a negative ε_r below its plasma frequency ω_p, which is regularly in the very high

frequency (ultraviolet) spectrum. The plasma frequency ω_p is a fixed parameter for each kind of metal with a simple equation $\omega_p = (ne^2/\varepsilon_0 m_{eff})^{1/2}$ [Kit05], where n is the conduction electron density, e is the electron charge and m_{eff} is its effective electron mass. In the lower frequency (microwave) spectrum, a mesh of conducting wires effectively behaves like a metal with a reduced effective plasma frequency $\omega_{p,\,eff}$ [Pen96]. The reason responsible for the reduction of ω_p is twofold: firstly the conduction electron density of the artificial metal is reduced; secondly the effective electron mass is also improved when electrons are confined in thin wires [Pen96]. Although this second reason is controversial [Pok02], the reduced plasma frequency was clearly demonstrated by both simulation and experiments [Pen98, Smi99]. More details can be found in references [Sie96, Pok02, Bel03, Pok04]. Figure 1-4 shows a simple example of such a metallic wire medium in the 2D case [Sol09, Ram05]. The metallic wires have a radius $\boldsymbol{r}$ and are placed in a square lattice with the same $\boldsymbol{x}$ and $\boldsymbol{y}$ period $\boldsymbol{a}$ ($\boldsymbol{a} >> \boldsymbol{r}$). When the 2D wire medium is illuminated by a $\boldsymbol{z}$-polarized electromagnetic wave, the electrons oscillating along the $\boldsymbol{z}$ direction have a diluted density $n_{eff} = (\pi \boldsymbol{r}^2/\boldsymbol{a}^2)n$. In the infinitely-thin-wire limit ($\boldsymbol{r} \to 0$), the effective electron mass is $m_{eff} = \ln(\boldsymbol{a}/\boldsymbol{r})\mu_0 \boldsymbol{r}^2 n e^2/2$. For aluminum ($n = 5.675\times10^{17}\text{m}^{-3}$) wires with parameters $\boldsymbol{r} = 1\mu\text{m}$ and $\boldsymbol{a} = 500\mu\text{m}$, the resulting effective plasma frequency is $\omega_{p,eff} = 8.2\text{GHz}$.

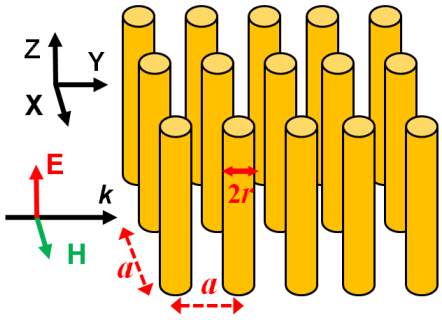

Figure 1-4. Sketch of a 2D metallic wire array. The wire is infinitely long (along **z**) and its radius is $\boldsymbol{r}$. Inter-wire distance is $\boldsymbol{a}$ along $\boldsymbol{x}$ and $\boldsymbol{y}$ directions (square lattice).

Since the metallic wire medium possesses much less conduction electrons than its constituent metal and can mimic a metal with a reduced plasma frequency, it is also called *diluted metal*. It is important note that the effective plasma frequency of the wire array can be tuned by varying the filling factor of metallic wires $\boldsymbol{r}/\boldsymbol{a}$.

Artificial Magnetism* (*negative permeability*)**. Compared with achieving a negative permittivity ε_r which is available in nature, achieving a negative permeability μ_r is a much more difficult task. As proposed by J. Pendry, a collection of metallic split ring resonators (SRRs) with subwavelength size can provide significant magnetic response, and particularly negative-valued μ_r in a spectral domain which can be tuned by engineering the resonator geometry [Pen99]. The fundamental mechanism for this magnetic response of SRRs is following. When a SRR [Fig. 1-5(a)] is excited by TM polarized (with **H** perpendicular to the ring) electromagnetic field, it can sustain rotating currents, which in turn generate a magnetic flux that can boost (paramagnetism) or oppose (diamagnetism) to the magnetic flux of the incident field. The current loop is complemented in the ring gap by a displacement current. In this sense, a SRR can mimic a magnetic dipole ***m.

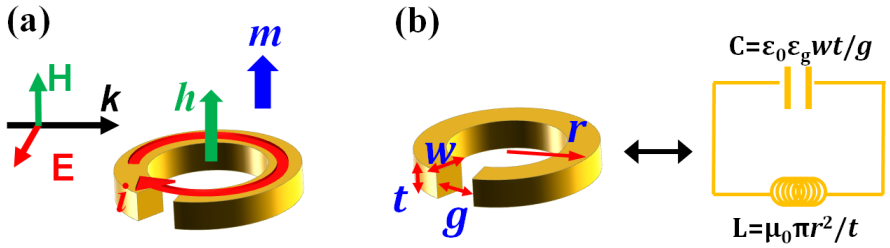

Figure 1-5. LC model for a metallic split-ring resonator (SRR). (**a**) Interaction between a metallic SRR and external electromagnetic wave. When **H** component of the incident field is perpendicular to the ring, rotating currents can be induced and accordingly mimic a magnetic dipole. (**b**) LC model for a circular SRR with radius *r*, width *w*, thickness *t* and gap size *g*. The capacitance C and inductance L are approximately derived as $C = \varepsilon_0\varepsilon_g wt/g$ and $L = \mu_0\pi r^2/t$ with the relative permittivity of the matter in the ring gap denoted as ε_g.

The ring has a self-inductance and the ring gap can be considered as a capacitor, so a SRR can be treated as a LC (inductor-capacitor) resonator [see Fig. 1-5(b)] with a resonance wavelength much longer than its size. As each SRR is a resonant LC circuit, that presents a dispersive magnetic response. The effective magnetic property, i.e. the effective permeability μ_{eff}, of a collection of SRRs can be described by referring to the classical *Drude-Lorentz theory*. The latter is well established for describing the electric permittivity ε_r of natural matter, where electrons and ions are regarded as elementary electric dipolar oscillators subject to the motive force of external electromagnetic field. The frequency-dependent dielectric function of a system composed of elementary electric harmonic oscillators with an inherent oscillation frequency ω_0 and a damping term γ is

$\varepsilon_r(\omega)=1+\omega_p^2/(\omega_0^2-\omega^2-i\gamma\omega)$. A lengthy proof for this expression and a more detailed discussion on its validity can be found in [Boh83, Kit05]. Similarly, the effective permeability μ_{eff} of a SRR array can be described as [Pen 99, Smi00, Ish05]

$$\mu_{eff} = 1 + f\omega^2/(\omega_0^2 - \omega^2 - i\gamma\omega), \tag{1-3}$$

where ω_0 is the inherent resonant frequency of LC-typed SRR, γ is the associated damping and f is the filling factor of SRRs in the composite. Around the LC resonance, the effective permeability μ_{eff} exhibits a Lorentzian shaped spectrum and it can reach negative value [$\mathrm{Re}(\mu_{eff})<0$] for $\omega > \omega_0$ when the damping is not too large. It should be highlighted that, within the simple LC model, the resonant wavelength λ_R is simply proportional to the SRR size [Smi00, Bri02, Bri04, Zho05, Ish05, Jep11]. For instance, the resonance wavelength of the circular SRR as sketched in Fig. 1-5 can be approximately expressed as

$$\lambda_R = 2\pi c\sqrt{LC} = 2\pi^{3/2} r\sqrt{\varepsilon_g w / g}, \tag{1-4}$$

where c denotes the speed of light in vacuum, ε_g denotes the relative permittivity of the material in the gap, w denotes the width of the ring and g denotes gap size. The capacitance C and inductance L are given in Fig. 1-5(b). Equation (1-4) clearly indicates that λ_R is proportional to the resonator radius r. Also the ring width and gap size can also be tuned in order to shift the functional wavelength of a SRR [Dol05].

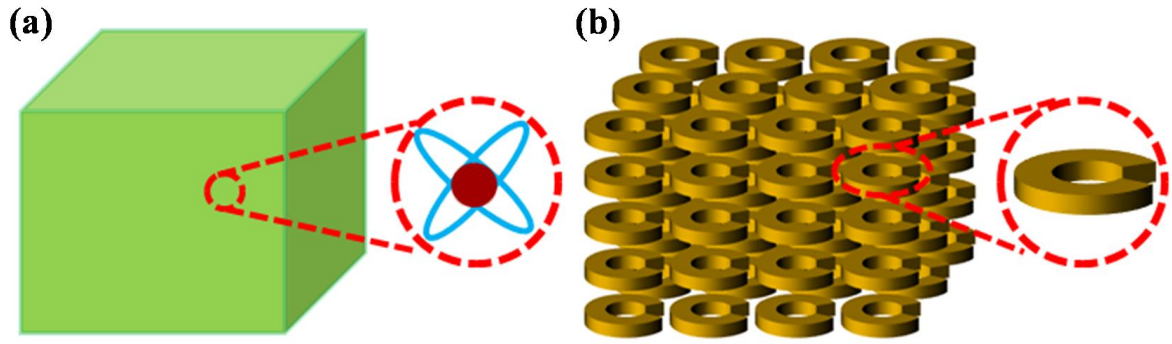

Figure 1-6. Comparison between conventional materials (**a**) and metamaterials (**b**). Properties of conventional materials derive from their constituent atoms or molecules, whereas properties of metamaterials originate from functional subwavelength resonators (metaatoms), which can be engineered at will.

The *Drude-Lorentz theory* offers an intuitive picture for the artificial magnetism of an engineered medium consisting of SRRs (or other functional mesoscopic resonators), see Fig. 1-6. In this sense, a mesoscopic SRR can be considered as a magnetic metaatom.

1.3.3 *Early experimental demonstration of negative-index metamaterials*

In 2000, D. Smith and colleagues [Smi00] fabricated a composite medium consisting of metallic wires and metallic SRRs, and observed a wave transmission phenomenon, which was understood by considering that the composite is equivalent to a homogeneous medium with simultaneously negative ε_r and μ_r for a frequency interval in the microwave spectrum. In a subsequent experiment [She01], a prism made of the wire and SRR composite was illuminated by an incident electromagnetic wave normal to the bottom of the prism, see Fig. 1-7. The (effective) refractive index was derived using Snell's law from the angle of output beam and was shown to be negative. The measured negative index was also fitted with a *Drude-Lorentz* model for ε_r and μ_r that exhibited negative values. This prism experiment however raised debates [Gar02, Val02] on its interpretation, because of the large absorption and of the possible existence of near-field effect due to the close detector-prism distance in the experiment.

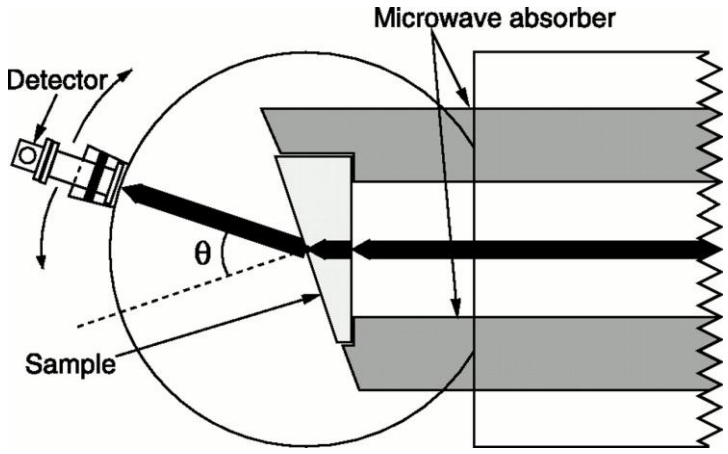

Figure 1-7. Setup used in Smith's prism experiment [She01] to show negative refraction. The incident microwave beam hits the prism sample from the right side and the angle of output beam is measured by a detector on the left side.

Negative refraction was further verified by similar prism experiments [Par03, Gre03], where the measurement was performed in the far field of negative-index metamaterials (NIMs) with less absorption losses. These experiments explicitly evidenced the existence of NIM with negative ε_r and μ_r [Pen03].

1.4 Negative-index metamaterials at optical frequencies

As previously explained, the key to realize negative-index metamaterials (NIMs) is to attain negative permeability at desired frequencies. At low frequencies, including THz and GHz, split-ring resonators (SRRs), see Fig. 1-5, can be utilized as a favorable magnetic metaatom. At higher frequencies, a direct solution for creating artificial magnetism is to scale down the size of the SRR since the LC resonant frequency scales reciprocally with the SRR size as shown in Eq. (1-4). With this method, people successfully observed magnetic response from SRR arrays in THz spectrum [Kat05] and later in near-infrared spectrum [Liu08a, Ser09]. However, at high frequencies, such as visible and near-infrared, the magnetic response of SRRs degrades [Zho05, Ish05, Lin06, Pen10]. The failure of SRRs at optical frequencies can be understood as a combination of several facts: the high absorption losses in metal, the strong dispersion of the metal permittivity and the fact that at least one dimension of the SRR becomes comparable with the skin depth in the metal (several tens of nanometers). In addition, significant fabrication challenges make the scaling of SRRs down to optical frequencies difficult, until now there has been no report on experimental demonstration of bulky NIMs based on SRRs, though SRRs can be assembled into a bulk-like magnetic metamaterial through a layer-by-layer stacking-up technique [Liu08a]. The main consequence of all these theoretical and technological issues is that novel designs have been proposed for pushing negative-index metamaterials toward optical frequencies.

In 2005, two new types of NIMs operating at near infrared frequencies were fabricated (only single layer): the so-called fishnet structure [Zha05] and a cut-wire pair array [Sha05], see Figs. 1-8(a) and (b). In fact, both geometries are based on the same concept, namely taking advantage of the current loop that can be supported by metal-dielectric (insulator)-metal (MIM) stacks [Pod03, Pen10]. The validity of this current loop picture can probably be questioned at optical frequencies, but one cannot deny that such concepts, inspired by the only work by J. Pendry on SRRs

[Pen99], allowed one to imagine innovative designs for negative-index metamaterials working at high frequencies. In the case of cut-wire pair arrays, the MIM stack providing the current loop is etched by two perpendicular arrays of wide slits. This results in disconnected metaatoms that consist of subwavelength MIM rectangular particles, see Fig. 1-8(b). On the other hand, the metaatoms composing a fishnet metamaterial are all connected because the MIM stack is simply etched by a 2D array of holes, see Fig. 1-8(a).

Phase measurements at near-infrared wavelengths showed a negative phase delay for light that passes through a single layer of fishnet or cut-wire pair array. In these metamaterials, note that, there is at least one dimension which is close to the half of the operating wavelength, on the contrary to microwave metamaterials, where all dimensions are deep subwavelength. In 2010 another NIM design, with negative index at visible frequencies was proposed. It is based on plasmonic coaxial waveguides [Bur10], see Fig. 1-8(c). In this design, the negative index directly originates from the plasmonic coaxial waveguide, which is non-resonant and supports a waveguide mode with a negative-valued effective index ($n_{\text{eff}} < 0$). Coaxial waveguide arrays are thus beyond the concept of metamaterials that we have adopted in this thesis, namely an array of resonant metaatoms, see Fig. 1-6.

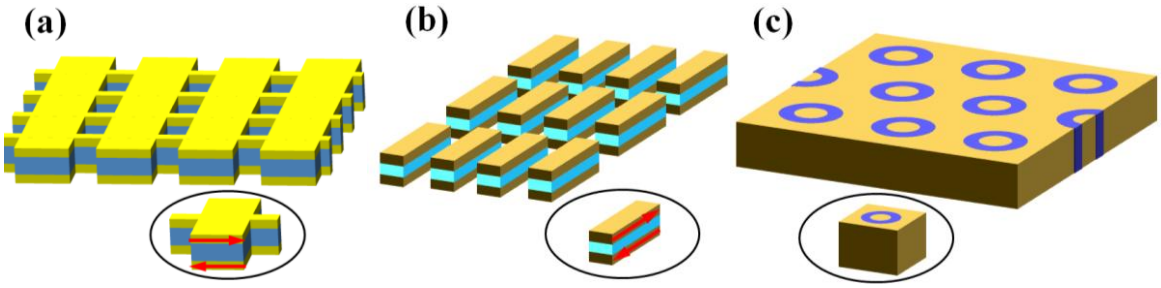

Figure 1-8. Negative index metaterial designs for optical frequencies and their corresponding metaatoms (in the circles). (**a**) Sketch of fishnet metamaterial that consists of alternating layers of metallic and dielectric thin films perforated by a hole array [Zha05]. (**b**) Cut-wire pair array as negative index metamaterial. Cut-wire pair array composed of pairs of metallic cut-wires separated by an insulator [Sha05, Lin05]. (**c**) Hexagonal array of subwavelength coaxial waveguides. The coaxial waveguide consists of a dielectric annular channel embedded in metal [Bur10]. In (a) and (b), the red arrows indicate the intuitive picture of current loops that are supported by the functional unit.

From a conceptual point of view, cur-wire pair arrays are extremely appealing, since they can clearly be identified as a collection of individual subwavelength

resonators, like SRR arrays in the microwave spectrum. However, until now, such structures have only shown weak negative indices with large absorption losses. On the contrary, much more experimental demonstrations have been achieved with fishnet metamaterials. Indeed, apart from the proof of concept in 2005 [Zha05], the negative-valued index of fishnet metamaterials was further verified by a prism experiment [Val08] similar to the one carried out in 2001 [She01] for microwave metamaterials. Moreover, broadband negative refractive indices with reasonably low losses have been reproducibly demonstrated by several groups for bulky fishnet structures with multiple functional layers [Val08, Cha11, Gar11]. Fishnet metamaterials have therefore been regarded as a highly promising candidate for realizing negative refractive index at optical frequencies. Much research effort has been exerted on the design and fabrication [Zha05, Zha06, Pau10, Val08, Cha11, Gar11], and on the understanding of the physics governing the light propagation inside fishnet structures [Roc08, Mar08b, Men10]. More recently, gain-assisted fishnet metamaterials have also been studied as a solution for reducing the absorption losses [Wue09, Fan10, Xia10, Ham11].

1.5 Outline of the thesis

The aim of this thesis is to address those questions with an emphasis on physics of optical fishnet metamaterials. In particular, we have derived an accurate semi-analytical model for the effective index of fishnets, which constitutes an important breakthrough in the modeling of optical metamaterials. The thesis can be divided into four parts.

In the *first* part (Chapter 2), we study the light scattering at an interface between a uniform half-space (air for instance) and a semi-infinite periodic photonic structure (a fishnet metamaterial for instance). With a three-dimensional (3D) fully-vectorial method, we calculate the scattering coefficients of the interface and evidence that, for some design, the energy transport inside the metamaterial can be due to a single mode, the fundamental Bloch mode supported by the periodic structure. Based on the knowledge of the single-interface scattering coefficients and of the effective index n_{eff} of the fundamental Bloch mode, we propose an innovative method for retrieving the effective optical parameters of the metamaterial. The approach emphasizes the key role played by the fundamental Bloch mode and

provides retrieved parameters that are more accurate or stable than those obtained by classical methods based only on far-field quantities, i.e. light reflection and transmission through finite-thickness metamaterial slabs.

Because of the importance of the fundamental Bloch mode in the light transport inside metamaterials, in the *second* part (Chapter 3), we derive closed-form expressions for the scattering coefficients (*r* and *t*) at an interface between two periodic media. This is a computationally demanding problem that can be lifted only with powerful numerical tools, and it is of major importance to derive accurate approximate expressions. In the derivation that relies on the Bloch mode orthogonality, we assume that only the fundamental Bloch modes of the two periodic media are known, all higher-order Bloch modes being unknown. Under the hypothesis that the two periodic media have only slightly different geometrical parameters, we show that the closed-form expressions are very accurate for various geometries, including dielectric waveguides and metallic metamaterials. They can thus be used with confidence for designing and engineering stacks of periodic structures.

As shown in the first part, the fundamental Bloch mode fully determines the optical property of fishnet metamaterials. In the *third* part (Chapters 4 and 5), we derive an accurate semi-analytical model for the fundamental Bloch mode of fishnets, which quantitatively predicts the effective index (including both the real-negative and imaginary parts). The model is based on the analysis of the energy flow through the fishnet mesh. This flow is supported by two perpendicular arrays of plasmonic waveguides and we track the plasmonic modes as they propagate and scatter in the structure. Since our approach obviously handles elementary processes that take place at a scale smaller than the metamaterial period, we describe our model as *microscopic*. The model explicitly shows that the origin of a broad-band negative index in fishnets can be mainly understood as the result of the resonant excitation of plasmonic modes propagating transversally along the dielectric layers. These modes present an anti-symmetric electric field distribution that recalls the current loop picture [Mar08]. The model goes beyond the simple picture since it quantifies the resonance and highlights the geometrical parameters that impact it. Finally, we extend the semi-analytical model to the important problem of loss-compensation with gain media. We show that with a moderate gain, the absorption losses in the metamaterial can be almost completely compensated, leaving the negative real part of the effective index unchanged. Another salient feature of the model is that, as there are only a few free physical parameters in it, it allows for an easy and precise

geometrical tailoring of the fishnet without resorting to cumbersome full-wave calculations.

As evidenced by the microscopic model, it is the "magnetic" resonance of plasmons in Metal-Insulator-Metal structures that creates the negative index of fishnet metamaterials. In the *fourth* part (Chapter 6), we study the asymptotic behavior of 3D Metal-Insulator-Metal nanoresonators as the resonator size is shrunk to very small dimensions well below the diffraction limit. In particular, we show that the quality factor of the resonance increases from 10 to 100 when the resonator volume is scaled from $(\lambda/2n^{\dagger})^3$ to $(\lambda/50)^3$ in the quasi-static regime. We provide a comprehensive study of the resonance scaling with a semi-analytical Fabry-Perot model. The latter quantitatively predicts the absorption and radiation losses of the nanoresonator and provides an in-depth understanding of the resonance lifetime that cannot be obtained with brute-force computations. In particular, it highlights the impact of slow-wave effects on the quality factor as the size of the resonator is decreased. The model remains accurate over the whole size scale even in the quasi-static regime for which retardation effects are not expected. This important and counterintuitive result indicates that both strongly localized resonances in plasmonic nanoparticles and delocalized resonance in elongated plasmonic nanowires can be possibly understood under the same conceptual umbrella, a wave-retardation based antenna problem.

†: *n denotes the refractive index of the dielectric spacer in MIM resonators*.

Chapter 2

Retrieving the effective parameters of metamaterials from the single interface scattering problem

Since the early proposals [Pen96, Pen99], the concepts of homogenization and effective parameters play a central role in the theoretical description of metamaterials. If the concept of homogenization is well established for metamaterials composed of deep subwavelength structures, it becomes more questionable as one approaches to mesoscopic regime where the metaatoms are only slightly subwavelength. In order to better understand when man-made structures may be considered as metamaterials with effective properties at optical frequencies, we study the scattering (reflection, transmission) of light at a single interface between a uniform half-space and a bulk metamaterial. We accurately compute the scattering coefficients between plane waves and the Bloch modes propagating inside the metamaterials. The knowledge of the single-interface scattering coefficients allows us to propose an innovative method for deriving effective optical parameters.

2.1 Introduction

Since the first realization of negative-refractive-index metamaterials for microwaves [She01], intensive work has been performed on this promising topic for ultimately controlling the electric and magnetic components of electromagnetic waves [Sha07, Sou07]. As the quest for metamaterials has been moving towards the optical spectral range, various theoretical issues have received considerable attention. The homogenization of artificially structured materials and the computation of their effective properties is one of them [Smi02, Kos05, See05, Smi06, Zha06, Roc08, Śmi08, Pet08, Vyn09]. Indeed, because the characteristic length of the functional unit is only slightly smaller than the wavelength, i.e. the metamaterial is mesoscopic, the homogenization of optical metamaterials is challenging [Kos05, See05] and various numerical techniques have been developed, including field averaging [Smi06], Bloch mode approaches [Zha06, Roc08, Śmi08], multipole expansion [Pet08, Vyn09], and inversion of scattering parameters (S-parameters) [Smi02, Kos05]. The latter consists of comparing the scattered waves from a metamaterial slab, which is inherently inhomogeneous, to those scattered from a hypothetical homogeneous slab with both an effective permittivity ε_{eff} and permeability μ_{eff}. The effective properties are thus derived from calculations or measurements of the S-parameters for finite-thickness samples. Owing to its generality that makes it applicable to virtually any structure, the S-parameter retrieval method has rapidly become the most commonly used tool for characterizing artificially structured metamaterials. But the generality of the method has a downside; since only the far-field response of the metamaterial matters, the retrieval procedure fully ignores the near-field response and the actual light propagation inside the structure. The fact that the light scattered by a complex structure is the same as that scattered by a homogeneous medium does not mean that light propagation *inside* the structure is similar to the propagation of a planewave in this homogeneous medium.

In order to better understand when man-made structures may be homogenized, we study the scattering of light at a single interface between a uniform half-space (air) and a semi-infinite three-dimensional (3D) periodic structure (the bulk metamaterial), see Fig.2-1(a). Taking advantage of an efficient fully-vectorial numerical method, we show that the knowledge of the single-interface scattering coefficients allows for an in-depth test of the validity of the metamaterial homogenization and we propose a new retrieval approach that relies on physical

quantities that are attached to the fine structure of the bulk metamaterial.

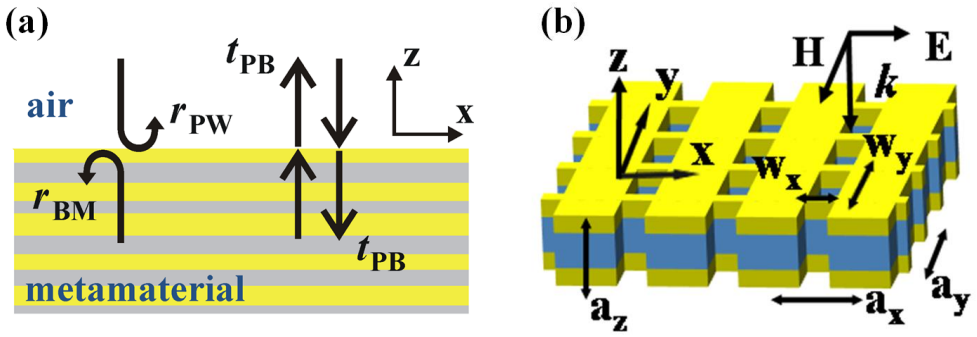

Figure 2-1. Scattering at a single interface between air and a bulk metamaterial. (**a**) Definition of the main scattering coefficients: r_{PW} is the specular reflection of the plane wave in air, r_{BM} is the reflection of the fundamental Bloch mode, and t_{PB} is the transmission from the fundamental Bloch mode to the plane wave and vice-versa. (**b**) One fishnet period in z-direction. A square lattice ($a_x = a_y = 860$nm) of rectangular holes ($w_x = 295$nm and $w_y = 595$nm) is etched into an Ag(15nm)-MgF_2(50nm)-Ag(15nm) periodic stack ($a_z = 80$nm).

2.2 Light scattering at an air/metamaterial interface

We consider hereafter the fishnet structure, which is one of the most promising optical metamaterials as explained in Chapter 1, composed of rectangular air holes etched in a metal/dielectric periodic stack. For the set of geometrical parameters defined in Fig. 2-1(b), the structure offers negative refraction at near-infrared wavelengths (1.4 μm < λ < 2 μm) with low losses [Val08], an achievement frequently interpreted as resulting from the realization of a metamaterial with both negative permeability and permittivity.

Light scattering at a single interface between a homogeneous half-space and a 3D periodic half-space, see Fig. 2-1(a), represents a generalization of the textbook case of scattering at a flat interface between two homogeneous media. The calculation of the generalized Fresnel coefficients requires a correct handling of outgoing wave conditions in a semi-infinite periodic medium. Only a few numerical methods are presently available to calculate those coefficients and only 2D geometries have been considered so far, mostly with dielectric materials [Śmi08, Dos06, Fal10]. Hereafter, we calculate the scattering coefficients by using a 3D fully-vectorial formalism that is an extension of a previous work on periodic waveguides [Lec07] to structures that are periodic in both transverse (x, y)

directions. For the sake of consistency, we concisely recall the main lines of the approach; more details can be found in [Lec07].

In a first step, we determine the complete set of metamaterial Bloch modes for a given in-plane wave vector (k_x, k_y) and at a given frequency by calculating the S-matrix relating the field amplitudes in two planes separated by a single metamaterial period a_z. The calculation is performed with the Rigorous Coupled-Wave Analysis (RCWA) [Li97]. Then the Bloch modes and their propagation constants $k_{z,BM}$ are obtained by solving for a generalized eigenmode problem. This procedure removes potential numerical instabilities [Cao02], even if a large number of Fourier harmonics is retained for the calculation or if thick and/or metallic layers are considered. The last step consists in matching the tangential field components at the air/metamaterial interface to derive the associated scattering matrix, i.e. transmission and reflection coefficients of all Bloch modes and plane waves. For that purpose, we use a Bloch mode and a plane wave (or Rayleigh) expansion in the metamaterial and in the upper uniform half-space, respectively.

For a metamaterial slab to be reasonably considered as a homogeneous effective medium, *the energy transfer through the slab has to be mediated dominantly by a single Bloch mode* that is bouncing between the two interfaces, like a single plane wave is bouncing forth and back in a homogeneous film [Zha06, Roc08, Śmi08, Lal98]. This Bloch mode will be referred to as the *fundamental Bloch mode* hereafter. We first calculate this fundamental mode in Section 2.2.1 and its scattering coefficients at the air/fishnet interface in Section 2.2.2. We finally test in Section 2.2.3 that the energy transfer through a fishnet slab composed of several periods can indeed be accurately described by the fundamental Bloch mode.

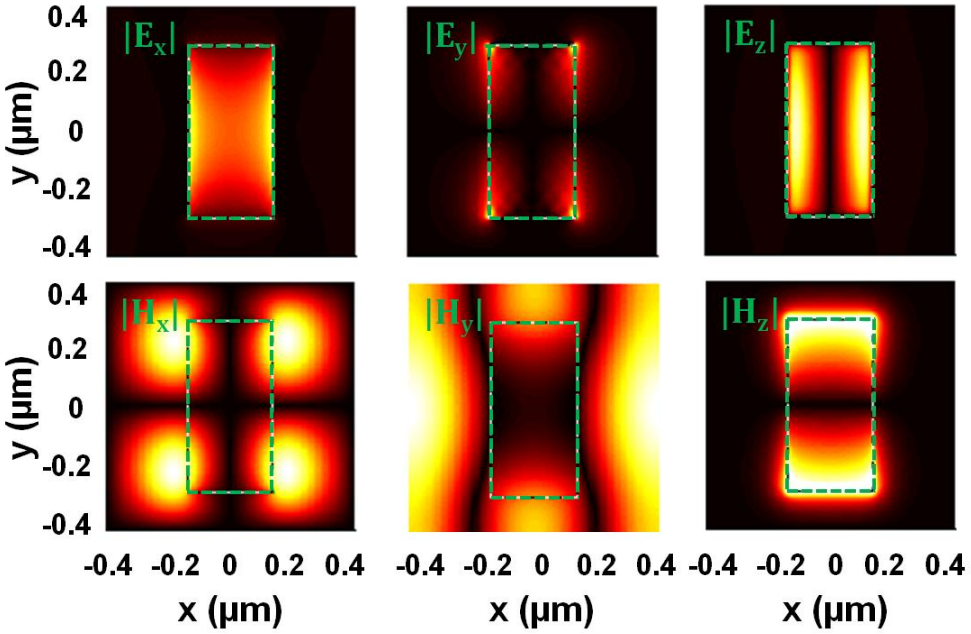

Figure 2-2. Profile of the six field components of the fundamental Bloch mode of the fishnet defined in Fig. 2-1. The calculation has been performed at $\lambda = 1.8\mu m$ and the field cross-section is taken in the middle of metallic layer at $z = ma_z$ with $m = 0,1,2...$ The green rectangle indicates the air hole.

2.2.1 *Fundamental Bloch mode of a fishnet metamaterial*

The fundamental Bloch mode can be identified from the infinite set of Bloch modes by considering either its effective index, $n_{BM} = k_{z,BM}/k_0$ with $k_0 = 2\pi/\lambda$, which possesses one of the smallest imaginary part, or its field distribution. For the fishnet, the field distribution inside the holes of the metallic layers much resembles that of the fundamental TE_{01}-like mode [Gor05] of an infinite rectangular air-waveguide in silver. As can be seen from Fig. 2-2, the E_x, E_y, E_z and H_z components of the fundamental Bloch mode are very similar as the ones of TE_{01}-like mode [Gor05].

The real and imaginary parts of calculated n_{BM} are shown in Fig. 2-3. In agreement with the experimental and theoretical data in [Val08], it is found that $\mathrm{Re}(n_{BM}) < 0$ for $\lambda > 1.5$ μm and that the Bloch mode attenuation is remarkably weak, $\mathrm{Im}(n_{BM}) < 0.18$ for $1.5 < \lambda < 1.8$ μm. The calculation has been performed at normal incidence ($k_x = k_y = 0$). The refractive index of the MgF_2 films is $n = 1.38$ and the frequency-dependent permittivity of silver is taken from [Pal85]. A total number of $N = (2m_x+1)(2m_y+1) = 1681$ Fourier harmonics has been used in the calculation, $m_x = m_y = 20$ being the truncation ranks in both transverse directions.

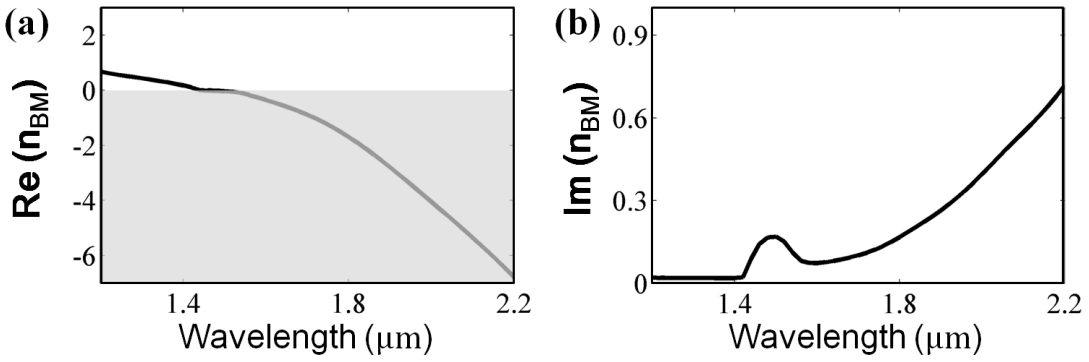

Figure 2-3. Effective index n_{BM} of the fundamental Bloch mode. (**a**) Real part. (**b**) Imaginary part. In (a) the region where Re(n_{BM})<0 is colored in gray.

2.2.2 *Scattering coefficients at the air/fishnet interface*

At a single interface, the coupling between the zeroth-order plane wave and the fundamental Bloch mode defines three independent scattering coefficients, the specular reflection of the plane wave in air, r_{PW}, the reflection of the fundamental Bloch mode inside the metamaterial, r_{BM}, and the transmission between the fundamental Bloch mode and the plane wave, t_{PB}, see Fig. 2-1(a). Reciprocity imposes that the latter is equal to the transmission coefficient between the incident plane wave and the fundamental Bloch mode. The moduli of the scattering coefficients are shown by red curves in Fig. 2-4 for the spectral range of interest and for normal incidence. Several interesting features are observed. First, we note that the spectra of every scattering coefficient exhibit a resonance for $1.4 < \lambda < 1.6$ μm. This can be understood as the signature of the excitation of a surface mode at the air/fishnet interface. Second, after entering the negative-index regime ($\lambda > 1.5$ μm), every scattering coefficient smoothly varies with the wavelength, attesting that the negative index is not due to any acute resonance.

Finally, it is interesting to check whether the calculated reflection coefficients satisfy the usual Fresnel relation at an interface between two homogeneous media, $r_{PW} = -r_{BM}$. As shown in Fig. 2-4(a), the moduli of the scattering coefficients are almost equal over the full spectral range ($|r_{PW}| \approx |r_{BM}|$), but the phases of the coefficients are not opposite, $|r_{PW}+r_{BM}| \neq 0$. This shows that the air/metamaterial interface cannot be fully understood as an interface between two uniform media.

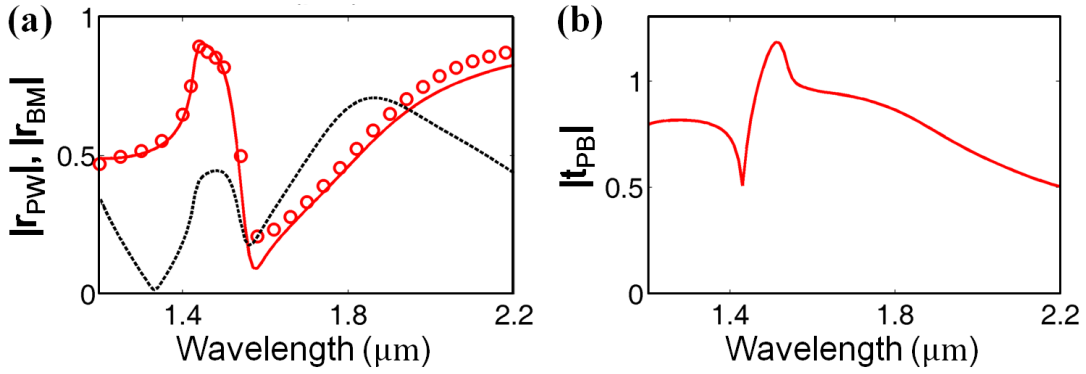

Figure 2-4. Scattering coefficients at the air/fishnet interface. (**a**) Red solid curve, $|r_{PW}|$, red circles, $|r_{BM}|$, and black dashed curve, $|r_{PW} + r_{BM}|$. (**b**) Red solid curve, $|t_{PB}|$.

2.2.3 *Single Bloch mode approximation*

The single interface scattering coefficients being determined, we now test if the energy transfer through a fishnet slab can be accurately described solely by the fundamental Bloch mode bouncing back and forth between the two interfaces. This is the single-Bloch-mode approximation. Under the assumption that the energy transport is mediated only by one mode, the reflection r and transmission t of a fishnet slab of thickness d are given by

$$r = r_{PW} + \frac{r_{BM} t_{PB}^2 u^2}{1 - r_{BM}^2 u^2}, \tag{2-1a}$$

$$t = \frac{t_{PB}^2 u}{1 - r_{BM}^2 u^2}, \tag{2-1b}$$

with $u = \exp(ik_0 n_{BM} d)$. Note that these Fabry-Perot equations hold for any Bloch mode, propagating or damped. The latter can be encountered for instance in tunneling transmissions. Figure 2-5 compares the specular transmission and reflection efficiencies (solid curves) calculated with the RCWA [Li97] for three slab thicknesses, d = 3, 5, and 10 a_z, with those (squares) obtained from Eqs. (2-1a) and (2-1b). The very good agreement observed leads us to the conclusion that, for this fishnet geometry, the light propagation can be mainly described by a single dominant Bloch mode.

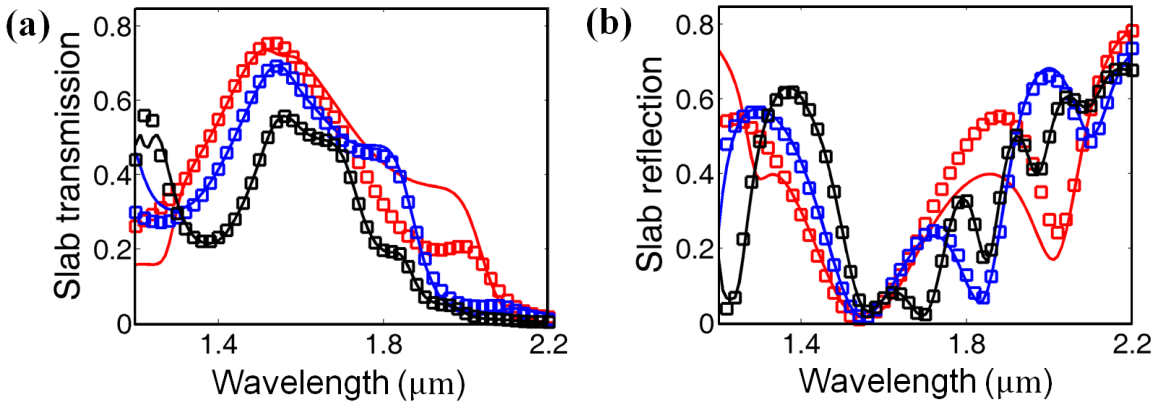

Figure 2-5. Transmission (**a**) and reflection (**b**) efficiencies of fishnet slabs with thicknesses of 3 (red), 5 (blue) and 10 (black) periods in the *z*-direction for normal incidence. Fully-vectorial RCWA data are shown by solid curves, and results obtained with the single-Bloch-mode approximation from Eqs. (2-1a) and (2-1b) are indicated by squares.

2.3 From the single interface to the retrieval of effective parameters

It is instructive to consider what the single interface problem teaches us on the homogenization problem. For that purpose, we propose a novel retrieval method for the effective parameters (n_{eff}, ε_{eff} and μ_{eff}) based on the scattering problem at the air/metamaterial interface. The results of the single-interface retrieval are compared to those of the classical S-parameter method [Smi02].

2.3.1 *Proposal of a retrieval method based on single interface scattering*

In our opinion, only metamaterials that satisfy the single-Bloch-mode approximation may be homogenized. Moreover any homogenization method should guarantee that the retrieved parameters, n_{eff}, ε_{eff} and μ_{eff}, are directly linked to the fundamental Bloch mode propagation constant by the relation

$$n_{\text{BM}} = n_{\text{eff}} = \sqrt{\varepsilon_{\text{eff}}\mu_{\text{eff}}}\,, \tag{2-2}$$

at least with a good approximation. If not, the effective parameters necessarily depend on the slab thickness.

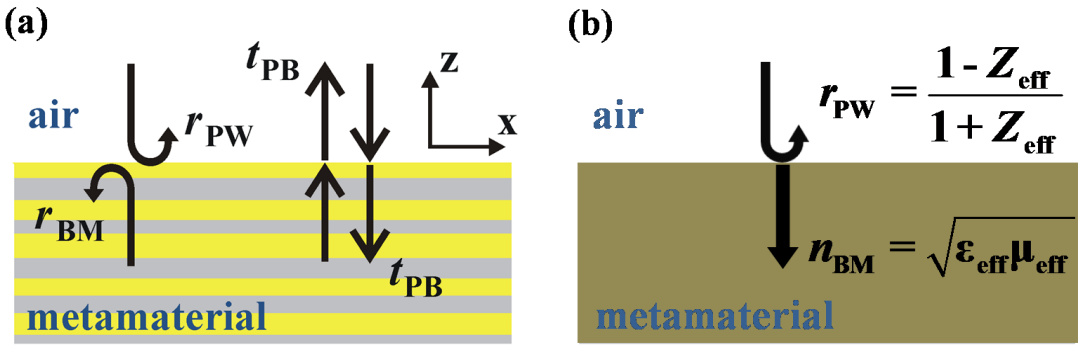

Figure 2-6. Scheme of the retrieval procedure of the effective parameters from the single interface scattering. (**a**) Actual scattering processes at the air/metamaterial interface. (**b**) Homogenizable metamaterial. The planewave reflectivity r_{PW} offers the information of the effective impedance of metamaterial Z_{eff} and the normalized Bloch mode propagation constant n_{BM} provides the effective refractive index n_{eff} of metamaterials.

Equation (2-2) alone does not allow to fully determine the effective parameters. In addition, we propose to use the Fresnel relation for the reflection between two homogeneous media as a function of the impedance. For normal incidence, $Z_{eff} = \sqrt{\mu_{eff}/\varepsilon_{eff}}$ and one gets

$$\sqrt{\frac{\mu_{eff}}{\varepsilon_{eff}}} = \frac{1 + r_{PW}}{1 - r_{PW}}. \qquad (2\text{-}3)$$

Equations (2-2) and (2-3) can be directly solved for ε_{eff} and μ_{eff}, without any ambiguity due to the square root. This retrieval scheme is summarized in Fig. 2-6. It has to be pointed out that, we select the planewave reflectivity r_{PW}, instead of the Bloch mode reflectivity r_{BM}, to derive the effective impedance Z_{eff}, because r_{PW} is experimentally measurable.

2.3.2 *Comparison between the S-parameter method and the proposed method*

We test our novel retrieval procedure by comparing its results with the predictions of the conventional S-parameter retrieval algorithm [Smi02]. We begin with the effective refractive index n_{eff}. We apply the S-parameter method to the RCWA data obtained for the scattering coefficients of the finite-thickness slab. The effective permittivity ε_{eff} and permeability μ_{eff} are retrieved for three slab thicknesses and the retrieved effective indices, $n_{eff} = \pm\sqrt{\varepsilon_{eff}\mu_{eff}}$, are compared with the fundamental Bloch

mode effective index n_{BM} in Fig. 2-7. An overall qualitative agreement is achieved. However, there are also some discrepancies, especially for large wavelengths, where one observes a spurious oscillatory behavior for n_{eff}, with minima or maxima that depend on the fishnet thickness. Let us emphasize that since all computations are performed with the same number of Fourier harmonics, the discrepancy between n_{eff} and n_{BM} is not due to any numerical artifact. It is rather unexpected, especially for thick slabs ($d = 5$ and $10\,a_z$), for which the single-Bloch-mode approximation is highly accurate (Fig. 2-5). As explained before, the reason for this discrepancy comes from the fact that the scattering properties at the air/metamaterial interface differ from those between two uniform media, in particular $r_{PW} \neq -r_{BM}$. Since our retrieval method directly calculates the light propagation inside the metamaterial (the fundamental Bloch mode), it avoids this detrimental oscillatory behavior.

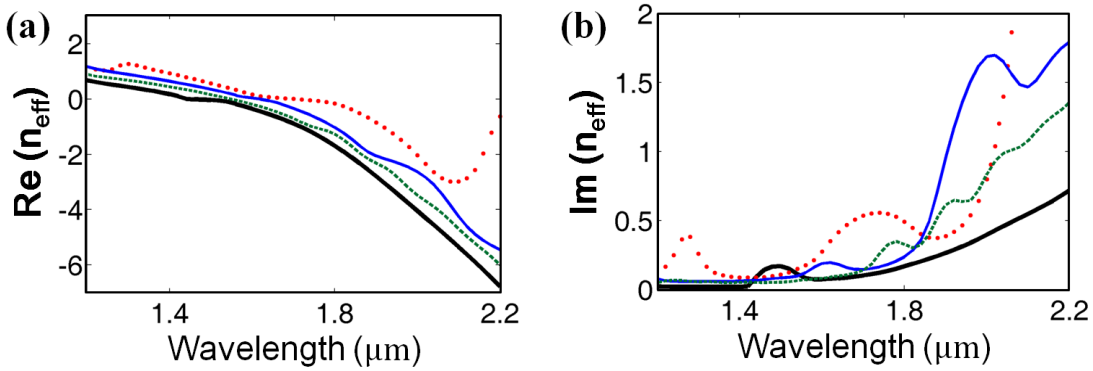

Figure 2-7. Retrieved effective index n_{eff} of a fishnet slab. (**a**) Real part. (**b**) Imaginary part. In (**a**)-(**b**) the Bloch-mode effective index (thick-solid black curves) is compared with the effective refractive index n_{eff} retrieved with the S-parameter method [Smi02] for several fishnet thicknesses, $d = 3a_z$ (dotted red), $5a_z$ (solid blue) and $10a_z$ (dashed green).

Figure 2-8 compares the effective parameters ε_{eff} and μ_{eff} with those obtained from a finite-thickness slab with the S-parameter retrieval algorithm [Smi02] and the proposed method based on the single interface scattering. Again, the unphysical oscillatory behavior is fully removed with the present approach. Formally, this procedure can be extended towards oblique incidence. The retrieved parameters ε_{eff} and μ_{eff} will then depend on the angle of incidence as a result of spatial dispersion due to the mesoscopic nature of metamaterials at optical frequencies [Men10]. In this case, description of light propagation would require particular care.

In practice, the proposed retrieval procedure based on Eqs. (2-2) and (2-3) can be applied to experimental data for thick metamaterials. In this limit, $|u| << 1$ and the

scattering coefficients of Eqs. (2-1a) and (2-1b) become $r = r_{PW}$ and $t = t_{PB}^2\, u$; r_{PW} is thus directly measured and n_{BM} can be indirectly (but unambiguously) determined by measuring the transmission coefficients of two metamaterial slabs with different thicknesses for instance.

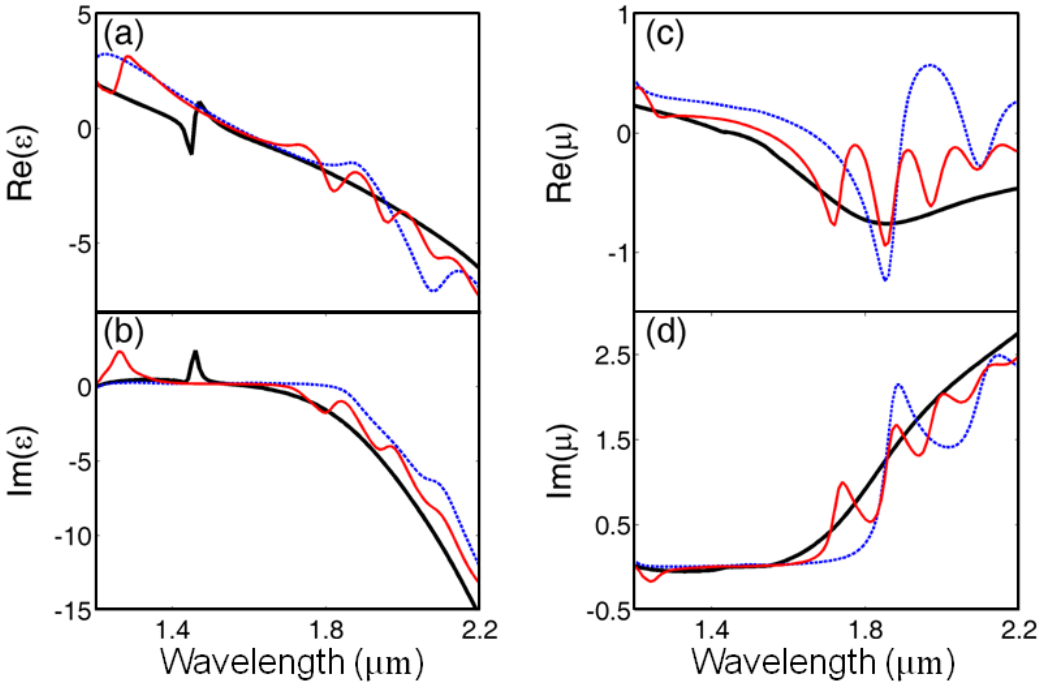

Figure 2-8. Retrieved effective permittivities ε_{eff} and permeabilities μ_{eff}. The dashed blue and solid red curves represent the retrieved parameters obtained with the S-parameter method [Smi02] using the RCWA data obtained for $d = 5$ and $10a_z$, respectively. The thick-solid black curve is obtained by solving Eqs. (2-2) and (2-3).

2.4 Conclusion

In conclusion, we have studied the scattering at an air/metamaterial interface. We have shown that the knowledge of the single-interface scattering coefficients allows for an in-depth test of the homogenization validity. Moreover, we have proposed an innovative approach for deriving the effective parameters. The method emphasizes the key role played by the fundamental Bloch mode and provides retrieved parameters that are more accurate or stable than those obtained by general methods based on far-field physical quantities.

Chapter 3

Closed-form expression for the scattering coefficients at an interface between two periodic media

We use the Bloch-mode orthogonality to derive simple closed-form expressions for the scattering coefficients at an interface between two periodic media, a computationally-challenging electromagnetic scattering problem that can be solved only with advanced numerical tools. The derivation relies on the assumptions that the interface is illuminated by the fundamental Bloch mode and that the two media have only slightly different geometrical parameters. Through comparison with fully-vectorial three-dimensional computations, the analytical expressions are shown to be highly predictive for various geometries, including dielectric waveguides and metallic metamaterials. They can thus be used with confidence for designing and engineering stacks of periodic structures.

3.1 Introduction and classical least mean square solution

Due to the possibility of controlling light at the wavelength scale in the optical domain, periodic nanostructures, such as photonic crystals and metamaterials, have attracted a considerable deal of interest within the last decades. Scientific breakthroughs have been enabled by the significant progress of nanotechnologies, which now allows the fabrication of dielectric or metallic periodic nanostructures with feature sizes down to several tens of nanometers. Although periodicity is indeed important, many devices are not fully periodic and include either local defects or tapers with a gradient of the geometrical parameters. Thus understanding wave scattering at an interface between two slightly different periodic structures has become a major issue.

Fully-vectorial, three-dimensional (3D) calculations of the scattering coefficients of such interfaces also represent a challenging electromagnetic problem, for which very few numerical tools are presently available in 3D [Lec07, Fal10]. In this chapter, we derive analytical expressions for the scattering coefficients between the fundamental Bloch modes of two periodic media. Under the assumption that the media differ only weakly, we show that very simple, but accurate, closed-form expressions can be derived for the scattering coefficients of the fundamental Bloch modes. Furthermore if we assume that the fundamental Bloch mode represents the main channel for the energy transport (single Bloch mode approximation), the propagation in stacks of periodic media can then be handled analytically by multiplication of 2 × 2 transfer matrices involving those coefficients, like in thin film stacks. The present derivation is motivated by the fact that simple intuitive theoretical formalisms have not been presented yet and that realistic expressions for coupling strengths at periodic interfaces may be useful for designing photonic devices, such as mode converters in periodic waveguides [Wei92, Lal02, Cak09], tapered photonic-crystal (PhC) mirrors [Lal08, Zai08], or graded index beamers [Cen05, Kur07], for defining the impedance of PhCs [Śmi08], or for the theoretical study of the impact of fabrication imperfections in slow-light PhC waveguides [Maz09], to quote a few of them.

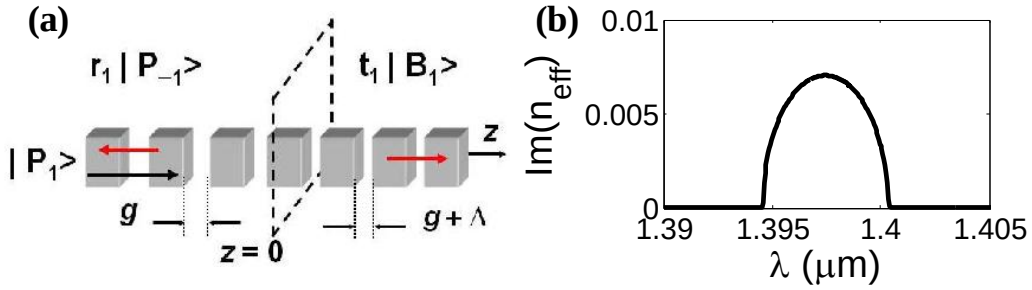

Figure 3-1. Scattering at the interface of two *z*-periodic media. In the transverse *x*- and *y*-directions the media can be periodic (fishnet metamaterial), or aperiodic [*z*-periodic GWs shown in (**a**)]. Only the fundamental Bloch modes, $|\mathbf{P}_1\rangle$ (incident), $|\mathbf{P}_{-1}\rangle$ (reflected), and $|\mathbf{B}_1\rangle$ (transmitted), are shown. (**b**) Imaginary part of the effective index of $|\mathbf{P}_1\rangle$.

3.2 Electromagnetic theory of light scattering at the interface between two periodic structures

Let us consider the scattering problem shown in Fig. 3-1, where the incident fundamental Bloch mode $|\mathbf{P}_1\rangle$ in the left periodic medium impinges on an interface separating two periodic structures. We adopt a Cartesian system hereafter with axes *x*, *y* and *z*, the axis *z* being normal to the interface. The field on both sides of the interface can be expanded into a Bloch mode basis, and using the field continuity relations at $z = 0$, we have

$$|\mathbf{P}_1\rangle + r_1|\mathbf{P}_{-1}\rangle + \sum_{m>1} r_m|\mathbf{P}_{-m}\rangle = t_1|\mathbf{B}_1\rangle + \sum_{m>1} t_m|\mathbf{B}_m\rangle. \qquad (3\text{-}1)$$

Equation (3-1), which is valid for the tangential field components, defines the reflection and transmission scattering coefficients r_m and t_m. Note that, on both sides of the equation, we have isolated the predominant outgoing fundamental Bloch modes, labeled $|\mathbf{P}_{-1}\rangle$ and $|\mathbf{B}_1\rangle$. The positive and negative subscripts refer to Bloch modes propagating towards the positive and negative *z*-directions, respectively. Our goal is to derive approximate expressions for the reflection and transmission coefficients, r_1 and t_1, by relying on the sole knowledge of the fundamental Bloch modes of the periodic media, the higher-order Bloch modes being assumed to be unknown. Because a rigorous solution of Eq. (3-1) with fully-vectorial software is

computationally expensive, approximate expressions are anticipated to facilitate the preliminary stages of the design of complicated components involving stacks of periodic structures.

As done in earlier works [Śmi08, Mom07, Bis04], it is first tempting to neglect all the unknown quantities, i.e., the higher-order Bloch modes, to end up with a simplified version of Eq. (3-1) that reads as

$$|\mathbf{P}_1\rangle + r_1|\mathbf{P}_{-1}\rangle = t_1|\mathbf{B}_1\rangle. \tag{3-2}$$

Assuming that $|\mathbf{P}_1\rangle$, $|\mathbf{P}_{-1}\rangle$ and $|\mathbf{B}_1\rangle$, are known at $z = 0$, the coefficients r_1 and t_1 can be obtained by projecting Eq. (3-2) on a complete set of functions $|\mathbf{F}_n\rangle$ – for instance Fourier harmonics – and solving the resulting system of equations in the least-mean-squares (LMS) sense. As will be shown, however, the accuracy of the LMS solution is very weak. This is because Eq. (3-2) authoritatively states an over-simplified expression for the fields on both sides of the interface and completely ignores the role of higher-order Bloch modes in the coupling mechanism. Actually, it is possible to take them into account, at least approximately, without explicitly calculating them, and one may derive analytical expressions for r_1 and t_1 that are more accurate than those obtained with the LMS approach, as will be shown hereafter. The elimination of the unknown higher-order Bloch modes in Eq. (3-1) can be achieved, under the sole assumption that the materials are reciprocal, by using Bloch mode orthogonality.

3.3 Bloch mode orthogonality

The derivation of Bloch mode orthogonality relays on *Lorentz reciprocity relation* [Sny83] for z-periodic structures, where z is the propagation direction of electromagnetic wave. Hereafter we establish this relation briefly, and more details can be found in [Lec07]. We consider two types of z-periodic structures, one is periodic in the transverse directions (x, y) [Fig. 3-2 (a)], and the other one not [Fig. 3-2 (b)]. For the first case, the Bloch modes under consideration only propagate in $\pm z$ direction, i.e. $k_x = k_y = 0$ but the analysis can be extended to “oblique” beams.

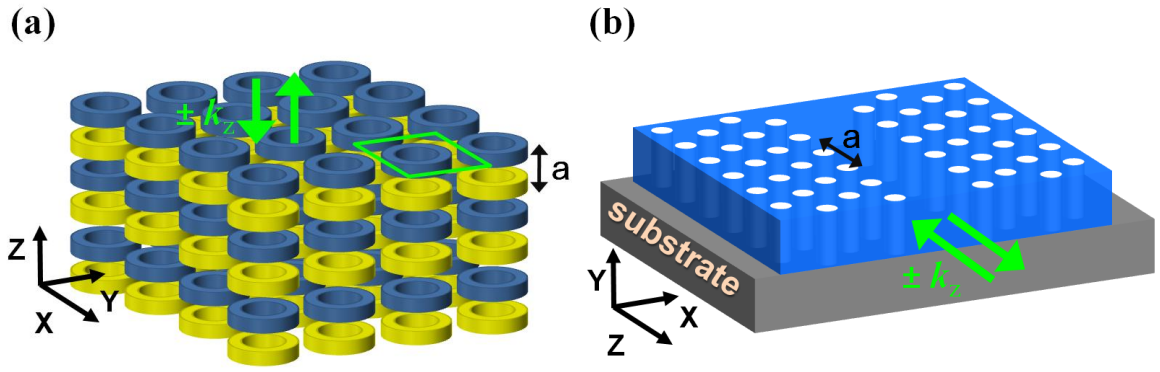

Figure 3-2. Sketches of two kinds of *z*-periodic structures. (**a**) A transversely-periodic photonic structure (e.g. a fishnet metamaterial). The associated Bloch modes under consideration only propagate along *z* direction, i.e. $k_x = k_y = 0$. The green square delimitates the unit cell in the transverse directions. (**b**) A *z*-periodic waveguide (e.g. a photonic crystal waveguide).

In the Cartesian coordinate (*x*, *y*, *z*) system and in the absence of any source, the curl Maxwell's equations are

$$\nabla \times \mathbf{E} = i\omega\mu_0\mu_r\mathbf{H} \text{ and } \nabla \times \mathbf{H} = -i\omega\varepsilon_0\varepsilon_r\mathbf{E}, \tag{3-3}$$

where **H** and **E** are the magnetic and electric fields at a given frequency ω, ε_r and μ_r are the relative permittivity and permeability tensors, and $i^2=-1$. In the following, we assume that the constituent materials of the photonic structures under consideration are reciprocal and possibly anisotropic. Thus everywhere we have $\mu_r = \mu_r^T$ and $\varepsilon_r = \varepsilon_r^T$, where the superscript T denotes matrix-transposition. We consider two solutions (labeled with the subscripts 1 and 2) at the same frequency ω,

$$\nabla\times\mathbf{E}_1 = i\omega\mu_0\mu_r\mathbf{H}_1 \text{ and } \nabla\times\mathbf{H}_1 = -i\omega\varepsilon_0\varepsilon_r\mathbf{E}_1, \tag{3-4a}$$

$$\nabla\times\mathbf{E}_2 = i\omega\mu_0\mu_r\mathbf{H}_2 \text{ and } \nabla\times\mathbf{H}_2 = -i\omega\varepsilon_0\varepsilon_r\mathbf{E}_2. \tag{3-4b}$$

Applying the Green-Ostrogradski formula to the vector $\mathbf{E}_2 \times \mathbf{H}_1$ on a closed surface S of volume V, one gets

$$\iint_S (\mathbf{E}_2\times\mathbf{H}_1)\bullet\mathbf{d}\boldsymbol{S} = \iiint_V i\omega(\mathbf{E}_2^T\varepsilon_0\varepsilon_r\,\mathbf{E}_1 + \mathbf{H}_1^T\mu_0\mu_r\mathbf{H}_2)\mathrm{d}V. \tag{3-5}$$

More remark on the closed surface S should be made here. For a transversely-periodic structure [Fig. 3-2 (a)], due to the transverse periodicity, the S can be restricted within a unit cell; for a waveguiding structure [Fig. 3-2 (b)], in principle S

should extend to infinity in transverse directions, however in practice for the purpose of computation it is bounded by perfectly-matched absorbers (PMLs) [Lec07]. By subtracting to Eq. (3-5) the related relation obtained by exchanging the indices 1 and 2, we further obtain

$$\iint_S (\mathbf{E}_2\times\mathbf{H}_1 - \mathbf{E}_1\times\mathbf{H}_2)\bullet d\mathbf{S} = \iiint_V i\omega(\mathbf{E}_2^T\varepsilon_0\varepsilon_r\mathbf{E}_1 + \mathbf{H}_1^T\mu_0\mu_r\mathbf{H}_2 - \mathbf{E}_1^T\varepsilon_0\varepsilon_r\mathbf{E}_2 - \mathbf{H}_2^T\mu_0\mu_r\mathbf{H}_1)dV. \quad (3\text{-}6)$$

In the following, we will consider closed surfaces formed by two *x*-*y* cross-sections in the *z*-periodic structures A_1 and A_2, defined by $z = z_1$ and $z = z_2 > z_1$. The surface integral in the left-side of Eq. (3-6) reduces to two surface integrals over A_1 and A_2. The reason is that, for the transversely periodic structure, due to its transverse periodicity, the integral over all the surface parallel to the *z*-axis is null; for the waveguide structure surrounded by PML, due to the PML damping, the field can be assumed to be negligible on the outer boundary surface of the PML, on which the integral is null. Additionally, noting that $\mathbf{E}_2^T\varepsilon_0\varepsilon_r\mathbf{E}_1 = \mathbf{E}_1^T\varepsilon_0\varepsilon_r\mathbf{E}_2$ and that $\mathbf{H}_2^T\mu_0\mu_r\mathbf{H}_1 = \mathbf{H}_1^T\mu_0\mu_r\mathbf{H}_2$ since the materials are reciprocal, we obtain from Eq. (3-6)

$$\iint_{z=z2} (\mathbf{E}_2\times\mathbf{H}_1 - \mathbf{E}_1\times\mathbf{H}_2)\bullet\mathbf{z}dS - \iint_{z=z1} (\mathbf{E}_2\times\mathbf{H}_1 - \mathbf{E}_1\times\mathbf{H}_2)\bullet\mathbf{z}dS = 0. \quad (3\text{-}7)$$

Equation (3-7) represents the Lorentz reciprocity relation applied to a *z*-periodic photonic structure. Denoting by $\mathbf{B}_1 = |\mathbf{E}_1, \mathbf{H}_1\rangle$ and by $\mathbf{B}_2 = |\mathbf{E}_2, \mathbf{H}_2\rangle$ the vector formed by the 6-components of the electric and magnetic fields, we define

$$\langle\mathbf{B}_1|\mathbf{B}_2\rangle_z = \iint_S (\mathbf{E}_2\times\mathbf{H}_1 - \mathbf{E}_1\times\mathbf{H}_2)\bullet\mathbf{z}dS. \quad (3\text{-}8)$$

With this notation, Eq. (3-7) is conveniently rewritten as

$$\langle\mathbf{B}_1|\mathbf{B}_2\rangle_{z_2} - \langle\mathbf{B}_1|\mathbf{B}_2\rangle_{z_1} = 0. \quad (3\text{-}9)$$

Equation (3-9) clearly indicates that $\langle\mathbf{B}_1|\mathbf{B}_2\rangle_z$ is independent on *z*. We denote the m^{th} forward-propagating Bloch mode in the *z*-periodic structure as $\mathbf{B}_m = |\mathbf{E}_m, \mathbf{H}_m\rangle\exp(ik_m z)$. Its associated backward-propagating mode is $\mathbf{B}_{-m} = |\mathbf{E}_{-m}, \mathbf{H}_{-m}\rangle\exp(-ik_m z)$. We assume the *z*-period of the structure is *a*, and we take $z_2 = z_1 + a$. We substitute n^{th} mode and m^{th} mode into Eq. (3-9), and obtain

$$\langle\mathbf{B}_n|\mathbf{B}_m\rangle_{z_1+a} - \langle\mathbf{B}_n|\mathbf{B}_m\rangle_{z_1} = 0. \quad (3\text{-}10)$$

It can be easily shown that $\langle\mathbf{B}_n|\mathbf{B}_m\rangle_{z_1+a} = \exp[i(k_m + k_n)a]\langle\mathbf{B}_n|\mathbf{B}_m\rangle_{z_1}$ and $\exp[i\mathrm{Re}(k_m + k_n)a] = 1$ (Floquet-Bloch condition), so Eq. (3-10) becomes,

$$\{\exp[-\mathrm{Im}(k_m+k_n)a] - 1\} \langle \mathbf{B}_n|\mathbf{B}_m\rangle_{z_1} = 0, \tag{3-11}$$

As long as in Eq. (3-11) there is *at least* one lossy or evanescent mode [$\mathrm{Im}(k) \neq 0$], which is always true for a monomode dielectric waveguide (higher-order modes are evanescent) or metallo-dielectric metamaterials or waveguide, when $m \neq -n$ (i.e. $k_m + k_n \neq 0$), $\exp[-\mathrm{Im}(k_m + k_n)a] \neq 1$, so $\langle \mathbf{B}_n|\mathbf{B}_m\rangle_{z_1} = 0$. Therefore, we obtain the Bloch mode orthogonality,

$$\langle \mathbf{B}_n|\mathbf{B}_m\rangle = \iint_S [\mathbf{E}_m \times \mathbf{H}_n - \mathbf{E}_n \times \mathbf{H}_m] \bullet \boldsymbol{z}\, \mathrm{d}S = 0 \text{ if } m \neq -n, \tag{3-12}$$

where we remove the subscript z, because Eq. (3-12) is z-independent. Additionally, Eq. (3-12) defines an antisymmetric bilinear form: $\langle \mathbf{B}_m|\mathbf{B}_n\rangle = -\langle \mathbf{B}_n|\mathbf{B}_m\rangle$. Hereafter, the Bloch modes are normalized so that $\langle \mathbf{B}_n|\mathbf{B}_{-n}\rangle = 4$, implying that non-evanescent Bloch modes propagating in lossless periodic media have unit power flow along the z axis.

In the present work, we only consider the scattering problem with a normal incident Bloch mode. More generally, for oblique incidence fixed by the in-plane Bloch-wavevector $[k_x, k_y] \neq 0$, the orthogonality relation of Eq. (3-12) must be modified to involve modes $|\mathrm{B}_n\rangle$ and $|\mathrm{B}_m\rangle$ with opposite in-plane Bloch-wavevectors $[k_x, k_y]$ and $[-k_x, -k_y]$ respectively, as stated by reciprocity arguments.

3.4 Closed-form expressions for the scattering coefficients of the fundamental Bloch modes

Coming back to Eq. (3-1), we start by deriving an approximate closed-form expression for r_1. Under the assumption that the periodic media are only slightly different, it is expected that the scattering process predominantly consists in exciting the fundamental Bloch modes, $|\mathbf{P}_{-1}\rangle$ and $|\mathbf{B}_1\rangle$, the excitation of the higher-order Bloch modes being a weaker process induced by the transverse mode-profile mismatch between the fundamental Bloch modes $|\mathbf{P}_1\rangle$ and $|\mathbf{B}_1\rangle$ [Pal01]. Therefore, an accurate expression for the reflection coefficient r_1 can be derived by neglecting the high-order transmitted Bloch modes, and we obtain

$$|\mathbf{P}_1\rangle + r_1|\mathbf{P}_{-1}\rangle + \sum_{m>1} r_m|\mathbf{P}_{-m}\rangle \approx t_1|\mathbf{B}_1\rangle. \tag{3-13}$$

Then, without any further approximation, we use the Bloch mode orthogonality and project the previous equation onto $<\mathbf{P}_1|$ and $<\mathbf{P}_{-1}|$, to get

$$r_1<\mathbf{P}_1|\mathbf{P}_{-1}> = t_1<\mathbf{P}_1|\mathbf{B}_1> \text{ and } <\mathbf{P}_{-1}|\mathbf{P}_1> = t_1<\mathbf{P}_{-1}|\mathbf{B}_1>, \quad (3\text{-}14)$$

from which we eliminate t_1 to obtain

$$r_1 = - <\mathbf{P}_1|\mathbf{B}_1>/<\mathbf{P}_{-1}|\mathbf{B}_1>. \quad (3\text{-}15)$$

Consistently, to calculate t_1, we first neglect the high-order reflected Bloch modes and, after projecting onto $<\mathbf{B}_1|$ and $<\mathbf{B}_{-1}|$, we obtain

$$r_1<\mathbf{B}_{-1}|\mathbf{P}_{-1}> + <\mathbf{B}_1|\mathbf{P}_1> = t_1<\mathbf{B}_1|\mathbf{B}_1> \text{ and } <\mathbf{B}_1|\mathbf{P}_1> + r_1<\mathbf{B}_1|\mathbf{P}_{-1}> = 0. \quad (3\text{-}16)$$

The elimination of r_1 leads to

$$4t_1 = <\mathbf{B}_{-1}|\mathbf{P}_1> - <\mathbf{B}_{-1}|\mathbf{P}_{-1}><\mathbf{B}_1|\mathbf{P}_1>/<\mathbf{B}_1|\mathbf{P}_{-1}>. \quad (3\text{-}17)$$

The closed-form expressions of Eqs. (3-15) and (3-17) constitute the main results of the present work. Henceforth, their accuracy will be tested for various geometries, such as dielectric waveguides and metallic metamaterials.

3.5 Test of the close-form expressions

Grating Waveguides. Let us first consider an interface [Fig. 3-1(a)] between two sub-λ grating waveguides (GWs). Every GW is a composite medium formed by periodically interlacing Si (n=3.48) segments embedded in a SiO_2 (n=1.44) host medium. Remarkably low propagation loss of 2.1 dB/cm in the telecom C-band has been recently reported [Boc10] for this geometry. The segment dimensions of the GW on the left side of the interface are c_x = 300 nm, c_y = 260 nm and c_z = 300 nm, and the grating period is a_z = 400 nm, corresponding to a SiO_2 gap length g = 100 nm.

We have calculated the band structure of the fundamental TE-like Bloch mode (with $E_y = 0$ for $y = 0$) with the aperiodic Fourier Modal Method (a-FMM) [Lec07]. The Bloch mode is truly guided in the spectral range of interest. Figure 3-1(b) shows the imaginary part of its effective index n_{eff}, i.e., its normalized wave vector. Note that, for 1.394 μm < λ < 1.404 μm, a band gap opens and Im(n_{eff}) is positive: the fundamental Bloch mode becomes evanescent. The GW on the right-hand side of the

interface [see Fig. 3-1(a)] has similar dimensions, except that the SiO_2 gap width is augmented by an incremental value Δ subject to variations.

We have computed the scattering coefficients at the interface with the a-FMM. We first determine the complete set of Bloch modes in the two media by diagonalizing the scattering matrix relating the field amplitudes in two planes separated by a_z. In a second step, we expand the field in each periodic medium in a Bloch mode basis, and by using Fourier-series expansions to match the tangential field components at the interface, we compute the scattering coefficients of all Bloch modes, i.e. all the r_m and t_m in Eq. (3-1). Figure 3-3 compares the scattering coefficients, $|r_1|^2$ and $|t_1|^2$, obtained with the a-FMM (black dots) and with Eqs. (3-15) and (3-17) (red curves).

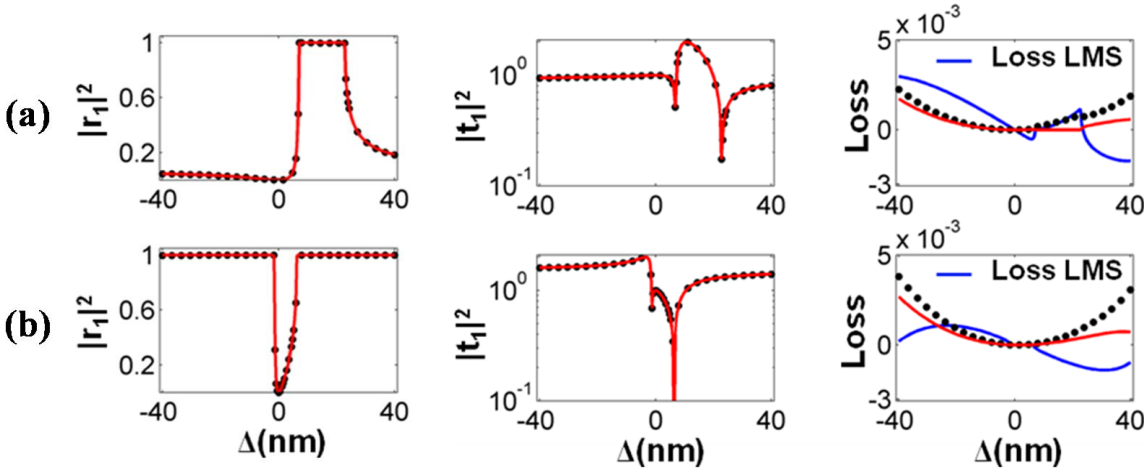

Figure 3-3. Test of the closed form expressions for an interface between two subwavelength GWs. Red curves: Predictions of Eq. (3-15) and (3-17). Black dots: fully-vectorial calculations obtained with the a-FMM by solving Eq. (3-1). The blue curves in the right panel represent the out-of-plane losses calculated by solving Eq. (3-2) in the LMS sense. (**a**) λ = 1.41 μm, (the incident Bloch mode $|\mathbf{P}_1\rangle$ is a propagating Bloch mode). (**b**) λ = 1.398 μm ($|\mathbf{P}_1\rangle$ is a gap evanescent Bloch mode).

The upper plots in Fig. 3-3(a) are obtained for λ = 1.41 μm; $|\mathbf{P}_1\rangle$ is propagating and $|\mathbf{B}_1\rangle$ can be either propagating or evanescent. Evanescent $|\mathbf{B}_1\rangle$ corresponds to a mirror behaviour. For the lower curves, λ = 1.398 μm, the incident Bloch mode is evanescent, and in the spectral region where $|r_1|^2$ is significantly smaller than one, $|\mathbf{B}_1\rangle$ is evanescent too. Let us emphasize that all the fundamental Bloch modes

operate below the light line of the SiO_2; they are not leaky, but are bounded modes. Therefore when they are evanescent, they do not carry any energy.

We note that an excellent agreement is achieved for all plots; for instance in Fig. 3-3(b), the maximum deviation between the a-FMM data and the approximate expressions is only 0.009 and 0.004 for $|t_1|^2$ and $|r_1|^2$, respectively.

The right panel shows the out-of-plane losses L at the interface for an incident Bloch mode normalized so that $<\mathbf{P}_1|\mathbf{P}_{-1}> = 4$. L can be simply calculated as the difference between the longitudinal (along z) power flow of $|\mathbf{P}_1> + r_1|\mathbf{P}_{-1}>$ and that of $t_1|\mathbf{B}_1>$. Note that when both $|\mathbf{P}_1>$ and $|\mathbf{P}_{-1}>$ are evanescent like in Fig. 3-3(b), the standing evanescent field, $|\mathbf{P}_1> + r_1|\mathbf{P}_{-1}>$, carries some net power flow, although the power flow of every individual Bloch mode is zero. It is worth emphasizing that the loss predictions obtained with the closed-form expressions of Eqs. (3-15) and (3-17) are much more accurate than those obtained by calculating r_1 and t_1 with Eq. (3-2) with the LMS approach (blue curves). Additionally note that the LMS values are inconsistently found to be negative for some values of Δ. It is also important to realize that the our-of-plane losses corresponds to the excitation of higher-order Bloch modes, and these Bloch modes are not calculated in the analytical treatment.

Fishnet metamaterials. The accuracy of Eqs. (3-15) and (3-17) has also been tested for completely different structures, by considering an interface between two fishnets. The reference fishnet consists of an array of rectangular air-holes etched in an Ag(15 nm)-MgF_2(50 nm)-Ag(15 nm) periodic stack [see inset in Fig. 3-4(a)], with the parameters reported in [Val08], see details in the caption of Fig. 3-4. This important geometry has been thoroughly analyzed in Chapter 2, where we have shown that the energy transfer through the fishnet is predominantly due to a single Bloch mode. The second fishnet is identical to the reference one, except that the MgF_2-layer thickness is increased by Δ.

Figure 3-4 compares the scattering coefficients, $|r_1|^2$ and $|t_1|^2$, obtained with the a-FMM [Lec07] (black dots) and with Eqs. (3-15) and (3-17) (red curves). The computation is performed for a normally-incident Bloch mode and $\lambda = 1.9$ μm, corresponding to a negative effective index $n_{\text{eff}} = -2.93+0.34\text{i}$ for $|\mathbf{P}_1>$. Again the predictions obtained with Eqs. (3-15) and (3-17) are quantitative and much more accurate than those obtained with the LMS approach (blue curves). The latter provides completely erroneous result, except for $|\Delta| < 5$ nm. Indeed, the fishnet problem represents a challenging test, much more difficult than the GW geometry, for which the fundamental Bloch mode is essentially a superposition of two

counter-propagating fundamental guided modes of the silicon ridges [Pal01]. For the fishnet, a 40-nm incremental value represents a substantial perturbation (remember that the reference dielectric thickness is 50 nm), and because the thickness of the metallic layer (30 nm) is comparable to the skin depth, higher-order Bloch modes are excited at the interface. This explains why the LMS approach completely fails for incremental values larger than a few nanometers.

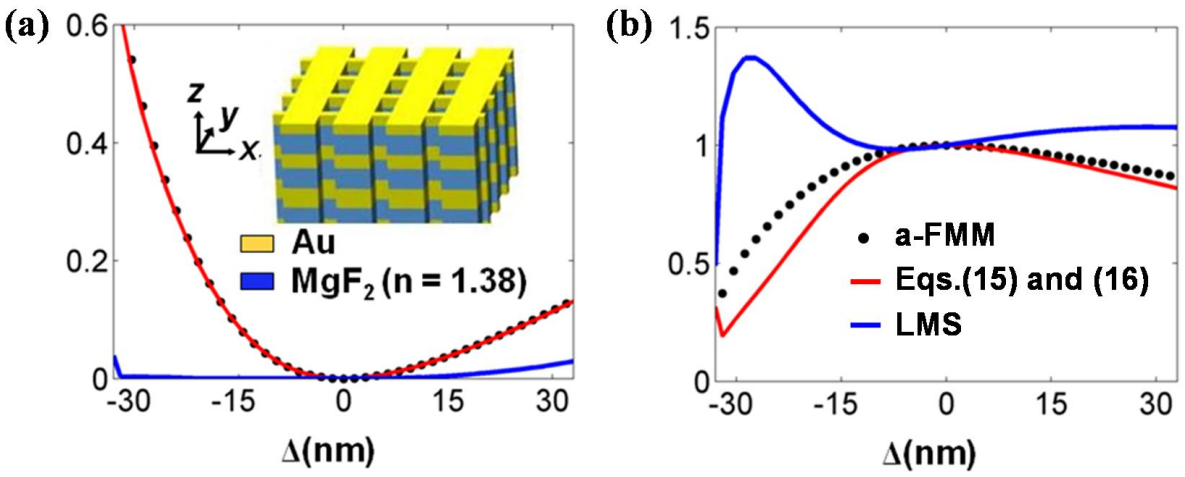

Figure 3-4. Test of closed-form expressions for an interface between two fishnet metamaterials. (**a**) $|r_1|^2$. (**b**) $|t_1|^2$. The fishnet parameters are those in [Val08]: the periodicity in the x- and y-directions is $a_x = a_y = 860$ nm, the rectangular hole dimensions are $w_x = 295$ and $w_y = 595$ nm. The refractive index of MgF_2 is 1.38 and the gold permittivity is –142+18.7i at $\lambda = 1.9$ μm. The calculation is performed for Bloch modes with $H_y(x) = H_y(-x)$. The inset sketches the fishnet geometry.

The accuracy improvement brought about by the present Bloch mode orthogonality approach can be understood as follows. For small increments Δ the overlap integrals $\langle \mathbf{P}_n | \mathbf{B}_m \rangle$ are $O(\Delta)$ for $n \neq \pm m$ and the higher-order coefficients r_m and t_m are also $O(\Delta)$ for $m > 1$. Therefore by neglecting the terms $r_m \langle \mathbf{B}_{\pm 1} | \mathbf{P}_{-m} \rangle$ and $t_m \langle \mathbf{P}_{\pm 1} | \mathbf{B}_m \rangle$ ($m > 1$) in the derivation of Eqs. (3-15) and (3-17) one commits an error of only $O(\Delta^2)$. In contrast, when we solve Eq. (3-2) in the LMS sense, the terms $r_m \langle \mathbf{F}_n | \mathbf{P}_{-m} \rangle$ and $t_m \langle \mathbf{F}_n | \mathbf{B}_m \rangle$ ($m > 1$) are neglected and, since the coefficients $\langle \mathbf{F}_n | \mathbf{P}_{-m} \rangle$ and $\langle \mathbf{F}_n | \mathbf{B}_m \rangle$ are $O(1)$ in general, the error is of the order $O(\Delta)$.

3.6 Conclusion

Simple and accurate closed-form expressions for the scattering at an interface between two slightly different periodic media can be derived using the Bloch mode orthogonality, even if one assumes that only the fundamental Bloch modes of the two media are known. The accuracy of the expressions have been thoroughly tested for several distinct geometries, including purely dielectric periodic waveguides offering large variations of the scattering coefficients in the vicinity of the band edges and metallo-dielectric structures providing rapid changes of the Bloch mode transverse profiles as one slightly tunes the geometrical parameters. High accuracy has been obtained in all cases, letting us expect that the expressions are reliable and can be used with confidence to design graded periodic structures.

Chapter 4

Microscopic model for fishnet metamaterials

At optical frequencies, fishnet metamaterials are one of the most promising geometries to realize low-loss negative refractive index. In this chapter, we abandon usual homogenization approaches and study in details how light propagates inside a fishnet structure. In sharp contrast with previous work, we theoretically investigate negative-index fishnet metamaterials with a "microscopic" model. The latter consists in tracking the transversal and longitudinal flows of energy through the fishnet mesh with a semi-analytical surface-plasmon coupled-mode theory. The microscopic model provides an accurate closed-form expression for the fishnet refractive index, including the real (negative-valued) and imaginary parts. The model provides a simple understanding of how the surface plasmon modes couple in the structure and it shines new light on the fishnet negative-index paradigm at optical frequencies. In this chapter, we formulate the microscopic model in a detailed manner.

4.1 Introduction

In the recently emerged fields of metamaterials, the possibility of creating optical negative-index metamaterials using nanostructured metallo-dielectric composites has triggered intense basic and applied research over the past several years [Sha07, Sou07, Zha05, Val08]. In the view of potential applications of such structures in a variety of areas ranging from subwavelength imaging [Sha07] to cloaking [Sch06], it is important to understand the underlying physics in detail. Until now, our common understanding of optical negative-index metamaterial is entirely based on various homogenization techniques including field averaging [Smi06], Bloch mode approaches [Zha06, Roc08, Yan10], multipole expansion [Pet08, Vyn09], and inversion of scattering parameters [Smi02], which are all based on fully-vectorial electromagnetic calculations of the whole structure. As a consequence, even if these approaches can quantitatively predict both the light transport inside the structure and its electromagnetic response, they are often non-intuitive, thus weakly supporting the design process required to apply metamaterials into new optical technologies. At microwave frequencies, lumped-elements circuit models provide a reliable framework for understanding and designing the properties of negative-index metamaterials [Sol09, Mar09]. Unfortunately, such a framework is lacking in the optical domain.

Inspired by a previous work that successfully explained the extraordinary optical transmission through metallic grating [Liu08b], we study fishnet negative-index metamaterials by adopting a "microscopic" point of view. We fully abandon classical homogenization approaches and instead we track the energy as it propagates and scatters through the fishnet mesh, like a fluid flowing in a multi-channel system. The dynamics involves two intersecting subwavelength channels and their coupling, see Fig. 4-1. The longitudinal (z-direction) channel consists of air holes in a metal film and the transversal (x-direction) channel is formed by metal-insulator-metal (MIM) waveguides that support the propagation of surface plasmon polariton modes, named as gap-SPPs hereafter. Through simple coupled-mode equations that describe how both channels exchange energy via plasmon scattering, we derive semi-analytical formulas for the fishnet refractive index and explain why negative values appear over a broad spectral range. In addition to corroborating previous analysis, the model shines new light on the physical origin of negative refraction in fishnets by analytically handling the key parameters that impact the resonant excitation of gap-SPPs.

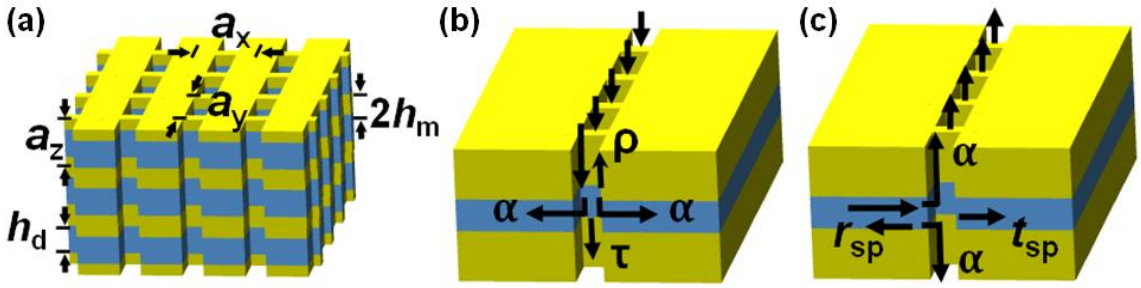

Figure 4-1. Elementary scattering events involved in a fishnet. (**a**) The fishnet under study is a two-dimensional array (period $a_x = a_y = 860$ nm) of rectangular holes (width $w_x = 295$ nm and $w_y = 595$ nm) etched into an Ag ($h_m = 50$ nm)-MgF_2 ($h_d = 50$ nm)–Ag ($h_m = 50$ nm) periodic stack. The refractive index of MgF_2 is $n_d = 1.38$ and the frequency-dependent permittivity of silver is taken from [Pal85]. (**b**) Scattering of the super-mode of a 1D metallic hole chain. (**c**) Scattering of the gap-SPP mode supported by a MIM waveguide. The scattering processes depicted in (b) and (c) define five elementary scattering coefficients, the reflection ρ and transmission τ of the super-mode, the reflection r_{sp} and transmission t_{sp} of the gap-SPP, and the coefficient α of coupling between the gap-SPP and the super-mode.

It is worth emphasizing that all the important optical properties of a fishnet negative-index metamaterial are driven by its fundamental Bloch mode. This statement was firstly observed in [Val08], where the measured refractive index was found to be equal to the calculated effective index n_{eff} of the fundamental Bloch mode. We have confirmed this point by numerical results showing that energy transport inside the fishnet is only mediated by the fundamental Bloch mode, as presented in Chapter 2 and in [Yan10]. Therefore, the following analysis will be mainly devoted to understanding the origin of the negative values of the normalized propagation constant n_{eff} of this Bloch mode. The latter have been calculated with a Fourier Bloch-mode method [Yan10] at normal incidence ($k_x = k_y = 0$). The simulation results (Fig. 4-2) predict a broad negative-index band for $\lambda > 1.7$ μm, with low loss around 1.8 μm, where the peak value (about 6) of figure of merit (FOM) is reached. FOM is a widely used concept to evaluate the loss in the metamaterials community; it is given by the ratio of the real part of the effective index to the imaginary part, $FOM = |\mathrm{Re}(n_{eff})|/\mathrm{Im}(n_{eff})$.

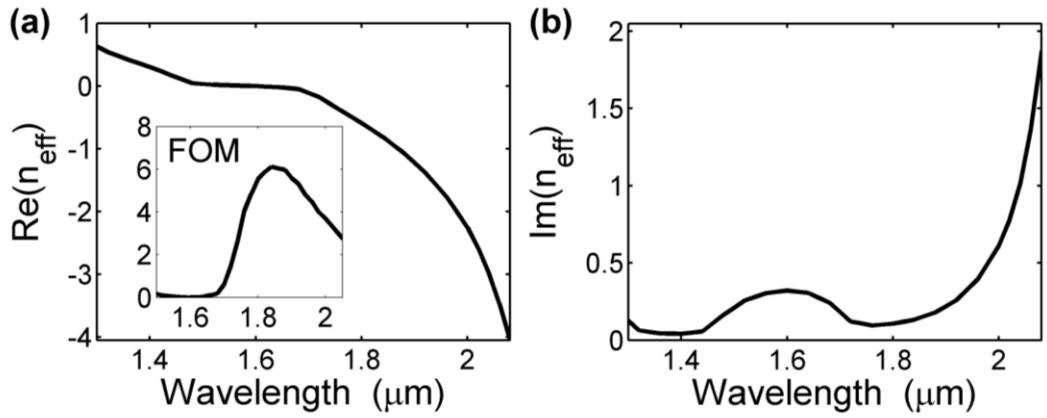

Figure 4-2. (**a**) The real part and (**b**) the imaginary part of the effective index of fishnet structure obtained by fully-vectorial calculation. The figure of merit FOM = $|\mathrm{Re}(n_{\mathrm{eff}})|/\mathrm{Im}(n_{\mathrm{eff}})$ is shown in the inset of (a). We have used the fishnet parameters used in [Val08] with an increased metal thickness, see the caption of Fig. 4-1.

We first describe in Section 4.2 the waveguides that form the longitudinal and transversal channels, respectively a rectangular metallic waveguide and a dielectric slab surrounded by metal (MIM waveguide). We then present the elementary scattering events that take place at the intersection between both waveguides, the reflection/transmission in each channel and the coupling between the longitudinal and transversal channels. In Section 4.3, we gather the ingredients to build a "microscopic" theory of light propagation that uses surface plasmon coupled-mode equations. Thanks to the semi-analytical expression of the fishnet effective index provided by the model, we give in Section 4.4 a comprehensive and quantitative understanding of the appearance of a broadband and low-loss negative index. We finally provide in section 4.5 a detailed overview of the numerical methods used to calculate the scattering coefficients and of its accuracy.

4.2 Elementary waveguide structures and scattering events

We model the energy transport in the fishnet mesh as resulting from the flow of surface plasmon modes through two intersecting subwavelength channels. Both channels, along with the definition of the relevant scattering coefficients, are depicted in Fig. 4-1. Hereafter, we first describe the waveguide geometries involved

in this description before calculating the scattering coefficients associated to their intersection.

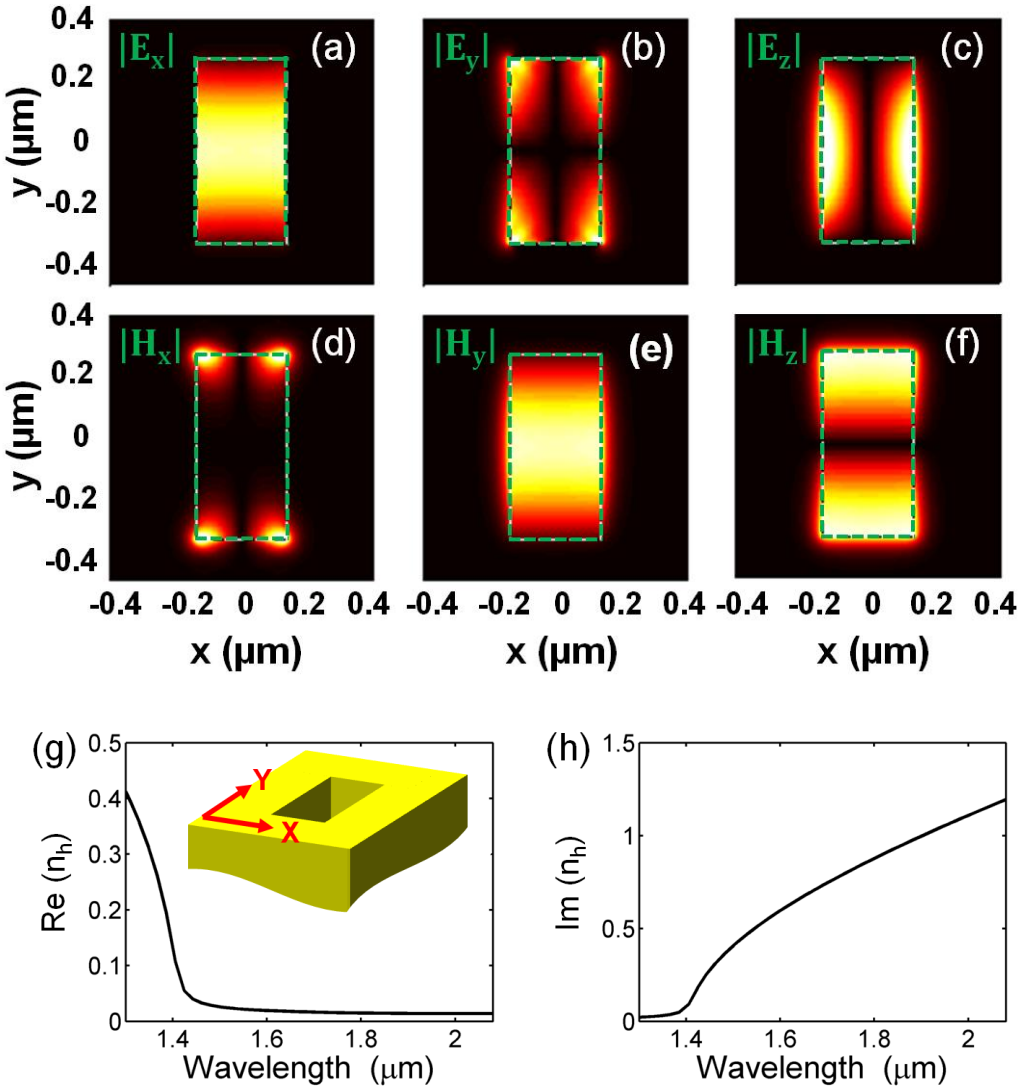

Figure 4-3. TE_{01}-like mode of a *single* metallic hole (inset) with the same parameters as the fishnet hole. (**a**) - (**f**) Profile of the six field components calculated at $\lambda = 1.8\mu m$ (below cut-off frequency). The real part (**g**) and imaginary part (**h**) of the effective index n_h. Inset: a single rectangular metallic waveguide.

4.2.1 *Two elementary waveguide structures in fishnet*

Longitudinal channel: 1D metallic hole chain. The longitudinal (*z*-direction) channel consists of a one-dimensional (1D) hole chain in a metal film; it supports the propagation of a super-mode, which is formed by the in-phase superposition of the

fundamental TE_{01}-like mode of every single hole [Fig. 4-3]. There is no coupling because the holes are isolated by their large separation: 565nm in *x*-direction and 265nm in *y*-direction. We assume that only this TE_{01} super-mode undertakes the vertical transport, since the higher-order modes of the metallic hole are more attenuated. What is more, as pointed out in Chapter 2, the field of the fundamental Bloch mode of the fishnet inside the metallic holes resembles the field of the TE_{01}-like mode. As shown in Figs.4-3(g) and (h), the TE_{01}-like mode becomes cut-off when $\lambda > 1.4\mu m$, where $\mathrm{Re}(n_h)$ drops to nearly zero and $\mathrm{Im}(n_h)$ increases rapidly.

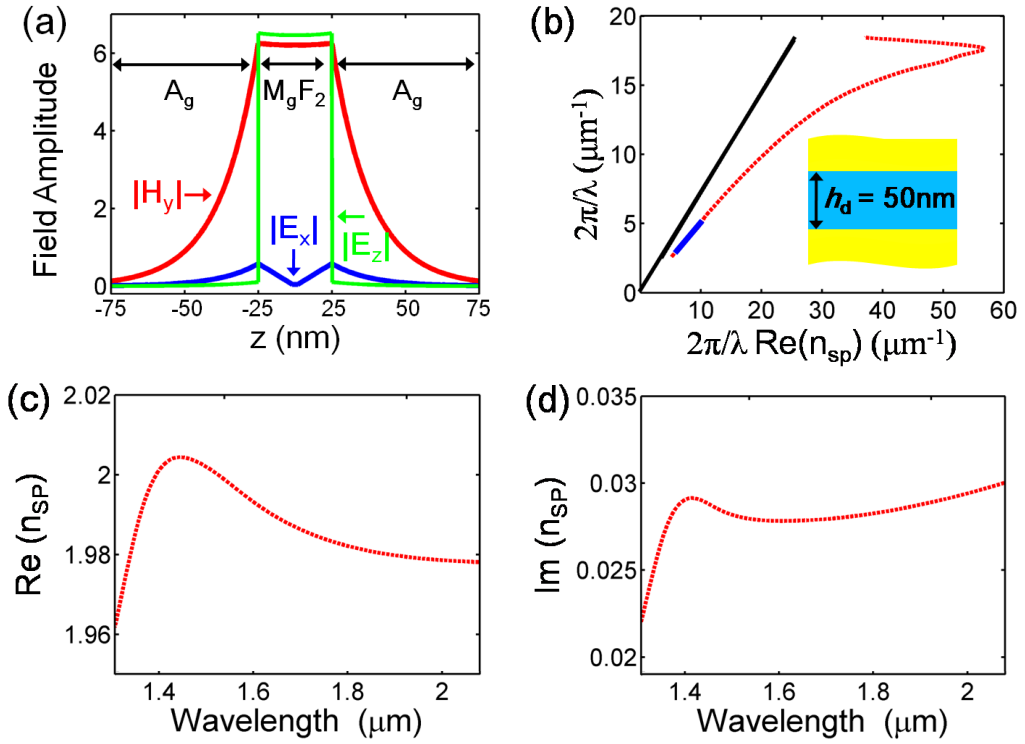

Figure 4-4. Gap-SPP mode of a MIM waveguide with a 50nm MgF_2 core and an infinite silver cladding. (**a**) Profile of the three field components of the gap-SPP calculated at $\lambda = 1.8\mu m$. (**b**) Dispersion diagram (red curve) of the gap-SPP mode. The black line is the light line in MgF_2 (n=1.38). The blue curve superimposed on the red one indicates the spectrum of interest. Inset: a sketch of the MIM waveguide. The real part (**c**) and imaginary part (**d**) of the effective index n_{SP} of the gap-SPP in the spectrum of interest ($\lambda = 1.2\sim2.2\mu m$).

Transversal channel: MIM waveguide. The transversal (*x*-direction) channel is formed by a metal-insulator-metal (MIM) waveguide that supports the propagation of gap-SPPs. The fundamental gap-SPP mode has a symmetric transverse magnetic field profile, $H_y(-z) = H_y(z)$, and an anti-symmetric electric field profile, $E_x(-z) = -E_x(z)$ [Eco69], see Fig. 4-4(a). In the spectrum of interest ($\lambda = 1.2\sim2.2\mu m$),

the effective index of gap-SPP is almost constant $n_{sp} \approx 1.98+0.028i$, see Figs.4-4(b), (c) and (d). Note that, the metallic cladding of MIM waveguide in the model is infinitely thick (not true for a realistic fishnet); this in fact is a source of inaccuracy of the model which will be analyzed thoroughly in Section 5.4 of the next Chapter.

4.2.2 *Elementary plasmon scattering processes*

At the intersection between both waveguides, the incident TE_{01} super-mode is partly transmitted (coefficient τ), reflected (coefficient ρ) or scattered (coefficient α) into the gap-SPP mode of the transversal MIM channel, see Fig. 4-1(b). Similarly an incident gap-SPP mode is scattered by the dielectric hole chain, see Fig. 4-1(c). Because of Lorentz reciprocity theorem, the transversal scattering process only defines two additional coefficients denoted by r_{sp} and t_{sp}. All the scattering coefficients, τ, ρ, α, r_{sp} and t_{sp} have been calculated by using a fully-vectorial frequency-domain modal method, the aperiodic Fourier Modal Method (a-FMM) [Sil01]. Note that the phase origins are all fixed at the center of the scatterer, which is the intersection between a metallic hole chain and a MIM waveguide.

TE_{01} supermode scattering. $|\tau|^2$ and $|\rho|^2$ [Fig.4-5(a)] exhibits clearly resonance feature at λ = 1.4μm, which corresponds to the cut-off the TE_{01}-like mode. Note that the TE_{01}-like mode is mainly transmitted, $|\tau|^2 >> |\rho|^2$

Gap-SPP scattering. $|t_{sp}|^2$ and $|r_{sp}|^2$ [Fig.4-5(b)] exhibit a resonance feature around λ = 1.7μm, which in fact is due to a Rayleigh anomaly event. The normally incident ($k_y = 0$, propagating along *x*-direction) gap-SPP hits hole chain with a period $a_y = 0.86\mu m$ and scatters. In our model, we solely consider the specular modal reflection and transmission of the 0-order gap-SPP. However the excitation of ±1-orders gap-SPP (Rayleigh anomaly) happens when the wavelength is smaller than the critical wavelength λ_c, which satisfies $\lambda_c = \mathrm{Re}(n_{sp})\, a_y$ at normal incidence ($k_y = 0$). As stated in Section 4.2.1, $\mathrm{Re}(n_{sp}) \approx 1.98$, thus the critical wavelength $\lambda_c \approx 1.98 a_y \approx 1.72\mu m$, which agrees with our observation. One may wonder whether the excitation of ±1-orders gap-SPP affects the energy transport in the fishnet. We will show in Section 4.3, we can safely neglect the ±1-orders gap-SPP even when they are propagative while preserving a highly accurate model. The reason is mainly that, for the fishnet structure under consideration and in the spectral range of negative index [$\mathrm{Re}(n_{eff}) < 0$ for $\lambda > 1.7\mu m$, entirely beyond the critical wavelength λ_c], the 0-order gap-SPP is resonantly excited, see Section 4.4.2. Notwithstanding, recently

people have observed the negative index fishnet structure, for which ±1-orders gap-SPPs play a key role [Gar09, Gar11].

Coupling between TE_{01} supermode and gap-SPP. TE_{01} supermode and gap-SPP mode can excite each other when they scatter at the waveguide intersection. In Fig. 4-5(c), the coupling coefficient α is plotted, where α_1 denotes the coupling coefficient calculated for the scattering process depicted in Fig. 4-1(b), and α_2 denotes the one calculated in the case of Fig. 4-1(c). According to Lorentz reciprocity theorem, the coupling coefficients in those two scattering events are the same, i.e., $\alpha_1=\alpha_2$. Obviously this relation is verified numerically as shown by Fig. 4-5(c), which confirms the accuracy of computation.

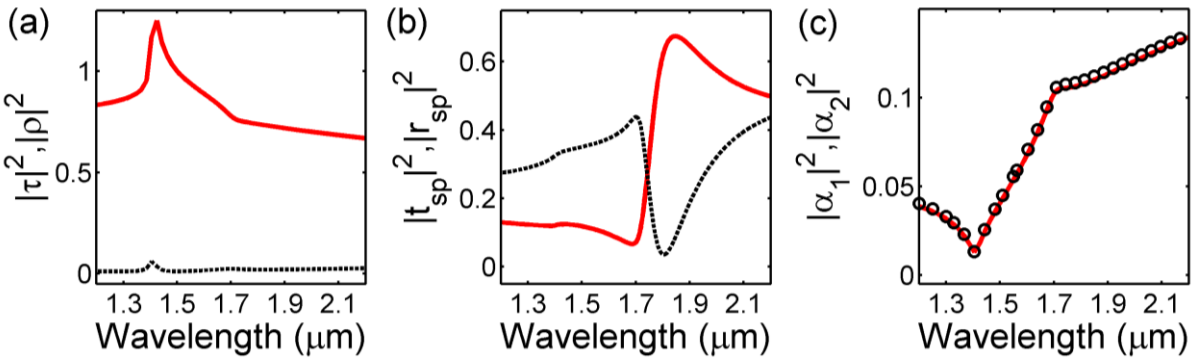

Figure 4-5. Spectra of the scattering efficiencies. (**a**) $|\tau|^2$ (red solid) and $|\rho|^2$ (black dashed). (**b**) $|t_{sp}|^2$ (red solid) and $|r_{sp}|^2$ (black dashed). (**c**) $|\alpha_1|^2$ (red solid) and $|\alpha_2|^2$ (black circles), with α_1 the $TE_{01} \rightarrow$ gap-SPP coupling coefficient and α_2 the gap-SPP $\rightarrow TE_{01}$ coupling coefficient. Owing to Lorentz reciprocity theorem, $\alpha_1 = \alpha_2 = \alpha$.

4.3 Microscopic model: a coupled mode formalism

Starting from the sole knowledge of the elementary scattering coefficients, in the following, we provide a step-by-step analysis that brings us to an analytical expression for the effective index of fishnet metamaterials. Firstly we start by considering the most elementary building-block of the fishnet, the metallic hole chain depicted in the inset (i1) of Fig. 4-6. In a second step, we analyze a more complex structure, namely a single hole chain etched into a Ag-MgF_2-Ag periodic stack (named as *z*-periodic hole-chain hereafter), see the inset (i2) in Fig. 4-6. Finally we analyze the complete fishnet structure, which can be viewed as an array of *z*-periodic

hole-chains, see inset (i3) in Fig. 4-6. In Figs.4-6(a) and (b), the effective indices of the modes mentioned above are all contained. Clearly, the microscopic model (red curve in Fig.4-6) can accurately predict the effective index (both real and imaginary parts) and the figure of merit (FOM) of the fundamental fishnet Bloch mode (black circles in Fig.4-6). This step-by-step build-up process with the microscopic model, allows us to disclose the origin of negative index of fishnet metamaterials, as will be discussed in Section 4.4.

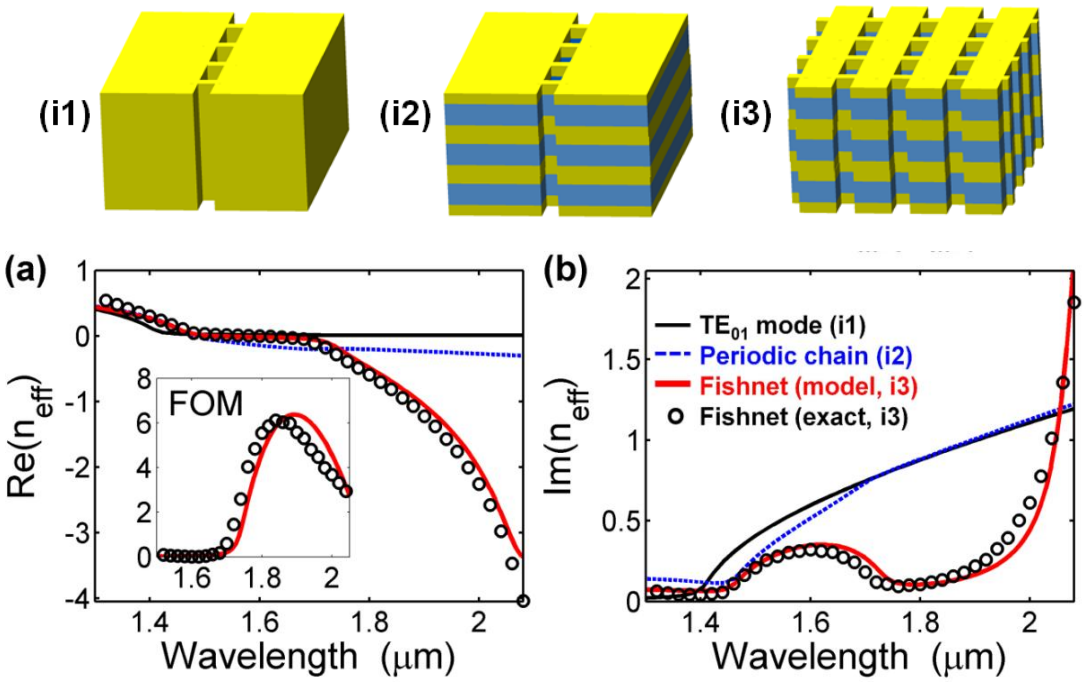

Figure 4-6. Model predictions for (**a**) the real part and (**b**) the imaginary part of the effective index. For building up the negative index of the fishnet, we study successively with the model the TE_{01} super-mode of a 1D hole chain [inset (**i1**)], solid black curves], the Bloch mode of a single z-periodic hole-chain [inset (**i2**), dashed blue curves] and the Bloch mode of the fishnet [inset (**i3**), solid red curves]. Results of fully-vectorial calculations of the fishnet Bloch mode are marked with circles. The figure of merit (FOM) $|\mathrm{Re}(n_{\mathrm{eff}})|/\mathrm{Im}(n_{\mathrm{eff}})$ is shown in the inset of (a).

4.3.1 *Metallic hole-chain: TE_{01} supermode*

The effective index n_{h} of the fundamental super-mode supported by the metallic hole chain [inset (i1) in Fig.4-6] is shown with the solid black curves in Fig. 4-6. The mode is evanescent at long wavelengths; $\mathrm{Im}(n_{\mathrm{h}})$ rapidly increases as the wavelength

exceeds the cut-off value of 1.4 μm, while Re(n_h) remains nearly null. As mentioned recently in [Mar08b, Gar09], a two-dimensional metallic hole array can be described by an effective permittivity governed by the cutoff frequency of the waveguide mode supported by the holes. For wavelengths above the cutoff, the effective permittivity is negative. This statement is consistent with our observation: in Fig.4-6 the spectral range of evanescence of the TE_{01}-like mode coincides with that of the fishnet negative index.

4.3.2 *Z-periodic hole-chain*

We next consider a more involved structure, namely a *single* hole chain etched into a Ag-MgF_2-Ag periodic stack, see inset (i2) in Fig. 4-6 and Fig. 4-7(a). The fundamental Bloch mode of this *z*-periodic hole-chain can be analytically derived by assuming that the field in the metallic holes is only formed by the superposition of two counter-propagating TE_{01} super-modes. Under the single-mode assumption, which is legitimate for tiny holes, the transfer matrix that links the amplitudes of the forward and backward super-modes, the A_m's and B_m's in Fig. 4-7(a), is a 2×2 matrix that solely depends on the scattering coefficients ρ and τ. The subscript *m* refers to the order of period in *z*-direction (m^{th} metallic layer and m^{th} dielectric layer), and it is incremented from top to bottom. Note that the coefficients A_m and B_m correspond to the amplitudes at the center of the m^{th} metallic layer.

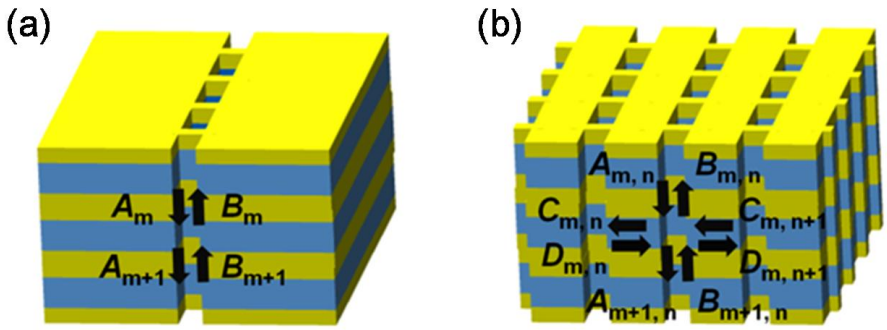

Figure 4-7. Definition of the modal amplitudes in the z-periodic hole chain (**a**) and in the fishnet (**b**). In the *z*-periodic hole chain (a), the light transport in the longitudinal channel (*z*-direction) is only mediate by counter-propagating TE_{01} super-modes (amplitudes A_m and B_m). In the fishnet (b), light transport in the longitudinal (*z*-direction) and transversal (*x*-direction) channels is only mediated by counter-propagating TE_{01} super-modes (amplitudes $A_{m,n}$ and $B_{m,n}$) and gap-SPPs (amplitudes $C_{m,n}$ and $D_{m,n}$), respectively.

The transfer matrix reads as

$$\begin{pmatrix} A_{m+1} \\ B_{m+1} \end{pmatrix} = \frac{1}{\tau v} \begin{pmatrix} (\tau^2 - \rho^2)\, v^2 & \rho v \\ -\rho v & 1 \end{pmatrix} \begin{pmatrix} A_m \\ B_m \end{pmatrix}, \tag{4-1}$$

where $v = \exp(\mathrm{i}k_0 n_\mathrm{h} a_\mathrm{z})$, with n_h the normalized propagation constant of the TE_{01} super-mode, a_z the longitudinal period of the fishnet and $k_0 = 2\pi/\lambda$ the vacuum wavevector. The periodicity along z requires that the field be pseudo-periodic

$$\begin{pmatrix} A_{m+1} \\ B_{m+1} \end{pmatrix} = \mathrm{e}^{\pm \mathrm{i}k_0 n_\mathrm{pc} a_\mathrm{z}} \begin{pmatrix} A_m \\ B_m \end{pmatrix}, \tag{4-2}$$

where n_pc is the effective index of the Bloch mode supported by the z-periodic hole chain. It can be easily derived from the sum of the transfer matrix eigenvalues $\exp(\pm \mathrm{i}k_0 n_\mathrm{pc} a_\mathrm{z})$, which is equal to the trace of the matrix in Eq. (4-1),

$$\cos(k_0 n_\mathrm{pc} a_\mathrm{z}) = \frac{\tau^2 v^2 - \rho^2 v^2 + 1}{2\tau v}. \tag{4-3}$$

Although it can be seen that n_pc (dashed blue curves in Fig. 4-6) and n_h are very similar, the longitudinal periodic structuring profoundly affects the nature of the energy transport. The super-mode of the hole chain (i1) and the Bloch mode of the z-periodic hole-chain (i2) are indeed different in nature. A key difference is that $\mathrm{Im}(n_\mathrm{h})$ is large because of the evanescent character of the TE_{01} mode below cut-off, whereas scattering losses due to the launching of gap-SPP modes into the transversal MIM waveguides is responsible for the large value of $\mathrm{Im}(n_\mathrm{pc})$. Moreover, for wavelengths larger than the cut-off of the TE_{01} mode, n_pc is negative (dashed blue curves), an effect that we attribute to the launching of gap-SPPs into the transversal MIM waveguides. However, n_pc is still far from the fishnet effective index n_eff, $|\mathrm{Re}(n_\mathrm{pc})| << |\mathrm{Re}(n_\mathrm{eff})|$ and $\mathrm{Im}(n_\mathrm{pc}) >> \mathrm{Im}(n_\mathrm{eff})$. We thus conclude that the longitudinal structuring cannot alone explain the low-loss negative index of the fishnet. This reveals the importance of another effect, namely a transversal resonant coupling that strengthens the gap-SPP excitation and that is responsible for the appearance of large negative n_eff values.

4.3.3 *Fishnet structure*

We finally consider the whole fishnet structure, which can be viewed as an array of z-periodic hole-chains that interact through the excitation of gap-SPPs, see inset (i3) in Fig. 4-6 and Fig. 4-7(b). Again a closed-form expression for the fishnet effective index n_{eff} can be analytically derived by assuming that the energy transfer in the dielectric gaps is solely mediated by the fundamental gap-SPP mode described in Fig. 4-4. According to the single mode approximation for both channels (longitudinal and transversal), the field in the metallic air holes and in the dielectric gaps is only formed by the superposition of two counter-propagating TE_{01} super-modes and gap-SPP modes, respectively. We denote by $A_{\mathrm{m,n}}$ and $B_{\mathrm{m,n}}$ the amplitudes of the down-going and up-going TE_{01} super-modes, and by $C_{\mathrm{m,n}}$ and $D_{\mathrm{m,n}}$ the amplitudes of the gap-SPP modes that propagate along the x-direction, leftward and rightward, see Fig. 4-7(b). The first subscript m refers to the period number in the z-direction (m^{th} metallic layer and m^{th} dielectric layer), m being incremented from top to bottom, and the second subscript n refers to the period number in the x-direction, n being incremented from left to right. With these notations, the coupling between the n^{th} hole chain and the m^{th} MIM waveguide is described by the four ingoing amplitudes $A_{\mathrm{m,n}}$, $B_{\mathrm{m+1,n}}$, $C_{\mathrm{m,n+1}}$, $D_{\mathrm{m,n}}$ and the four outgoing amplitudes $A_{\mathrm{m+1,n}}$, $B_{\mathrm{m,n}}$, $C_{\mathrm{m,n}}$ and $D_{\mathrm{m,n+1}}$, as shown in Fig. 4-7(b). Note that the coefficients $A_{\mathrm{m,n}}$ and $B_{\mathrm{m,n}}$ correspond to the amplitudes at the center of the m^{th} metallic layer, and the coefficients $C_{\mathrm{m,n}}$ and $D_{\mathrm{m,n}}$ correspond to the amplitudes in the middle of the n^{th} MIM section.

Using the five elementary scattering coefficients (α , r_{sp} , t_{sp} , ρ and τ), we can derive a four-port scattering matrix that describes the scattering process occurring at the intersection of the m^{th} MIM waveguide and the n^{th} hole chain

$$\begin{pmatrix} A_{m+1,n} \\ B_{m,n} \\ C_{m,n} \\ D_{m,n+1} \end{pmatrix} = \begin{pmatrix} \tau v & \rho v & \alpha u^{1/2} v^{1/2} & \alpha u^{1/2} v^{1/2} \\ \rho v & \tau v & \alpha u^{1/2} v^{1/2} & \alpha u^{1/2} v^{1/2} \\ \alpha u^{1/2} v^{1/2} & \alpha u^{1/2} v^{1/2} & t_{\mathrm{sp}} u & r_{\mathrm{sp}} u \\ \alpha u^{1/2} v^{1/2} & \alpha u^{1/2} v^{1/2} & r_{\mathrm{sp}} u & t_{\mathrm{sp}} u \end{pmatrix} \begin{pmatrix} A_{m,n} \\ B_{m+1,n} \\ C_{m,n+1} \\ D_{m,n} \end{pmatrix}, \tag{4-4}$$

where $v = \exp(\mathrm{i}k_0 n_{\mathrm{h}} a_{\mathrm{z}})$, $u = \exp(\mathrm{i}k_0 n_{\mathrm{sp}} a_{\mathrm{x}})$, n_{sp} is the normalized propagation constant of the gap-SPP and a_{x} is the transversal period of the fishnet. In this 4×4 scattering matrix, which involves both guided modes, the 2×2 top-left and bottom-right blocks represent the scattering along the longitudinal and transversal directions,

respectively. The off-diagonal 2×2 blocks represent the coupling between both channels. Note that, to be valid, in principle Eq. (4-4) does not require that the structure be periodic along *x* and/or *z*-directions, the proposed coupled mode formalism based on the scattering of SPP modes can be applied to any aperiodic structure.

In the case where the structure is periodic in the *x*-direction (period a_x), such as the fishnet structure, the Floquet-Bloch condition imposes the pseudo-periodicity of the field along *x*, which can be expressed as

$$C_{m,n} = \beta C_{m,n+1} \text{ and } D_{m,n} = \beta D_{m,n+1}, \tag{4-5}$$

where $\beta = \exp(ik_x a_x)$ with k_x the *x*-component of the wavevector of the incident plane wave. At normal incidence ($k_x = 0$, $\beta = 1$), the amplitudes in the transversal channel satisfy $C_{m,n} = C_{m,n+1}$ and $D_{m,n} = D_{m,n+1}$. Then the latter can be eliminated from Eq. (4-4) and the 4×4 scattering matrix reduces to a 2×2 scattering matrix that solely describes the longitudinal light propagation

$$\begin{pmatrix} A_{m+1,n} \\ B_{m,n} \end{pmatrix} = \begin{pmatrix} (\tau+\gamma)v & (\rho+\gamma)v \\ (\rho+\gamma)v & (\tau+\gamma)v \end{pmatrix} \begin{pmatrix} A_{m,n} \\ B_{m+1,n} \end{pmatrix}. \tag{4-6}$$

In addition, the following equation couples the amplitudes in the longitudinal and transversal channels

$$C_{m,n} = D_{m,n} = \frac{\gamma v^{1/2}}{2\alpha u^{1/2}} \left(A_{m,n} + B_{m+1,n} \right). \tag{4-7}$$

In Eqs. (4-6) and (4-7), the new parameter γ fully includes the transversal coupling between the adjacent hole chains through the MIM waveguides. It physically represents the multiple scattering of the gap-SPP in the dielectric layers and it is given by

$$\gamma = \frac{2\alpha^2 u}{1 - \left(t_{sp} + r_{sp} \right) u}. \tag{4-8}$$

As will be shown hereafter, this multiple scattering term plays a crucial role in the realization of negative refractive index in fishnet metamaterials.

Closed-form expression for the fishnet effective index n_{eff}. We are interested in calculating the fishnet Bloch mode propagating along the *z*-direction for a given k_x.

Therefore, the amplitudes $A_{m,n}$ and $B_{m,n}$ in the longitudinal channel have to satisfy a pseudo-periodic condition similar to Eq. (4-2)

$$\begin{pmatrix} A_{m+1,n} \\ B_{m+1,n} \end{pmatrix} = e^{\pm i k_0 n_{eff} a_z} \begin{pmatrix} A_{m,n} \\ B_{m,n} \end{pmatrix}, \tag{4-9}$$

where n_{eff} is the fishnet effective index, i.e., the normalized propagation constant of the fundamental Bloch mode. Equation (4-9) means that $\exp(\pm i k_0 n_{eff} a_z)$ are the two eigenvalues of the transfer matrix that links the amplitudes of the TE_{01} super-mode in two metallic layers separated by one period a_z. This transfer matrix is easily derived from the scattering matrix in Eq. (4-6) and reads as

$$\begin{pmatrix} A_{m+1,n} \\ B_{m+1,n} \end{pmatrix} = \frac{1}{(\tau+\gamma)v} \begin{pmatrix} [(\tau+\gamma)^2 - (\rho+\gamma)^2]v^2 & (\rho+\gamma)v \\ -(\rho+\gamma)v & 1 \end{pmatrix} \begin{pmatrix} A_{m,n} \\ B_{m,n} \end{pmatrix}. \tag{4-10}$$

The trace of the matrix is equal to the sum of its eigenvalues, so one straightforwardly obtains a closed-form expression for the fishnet effective index

$$\cos(k_0 n_{eff} a_z) = \frac{(\tau+\gamma)^2 v^2 - (\rho+\gamma)^2 v^2 + 1}{2(\tau+\gamma)v}. \tag{4-11}$$

The only difference with Eqs. (4-1) and (4-3) is the appearance of a new parameter γ; ρ and τ have been changed in ρ + γ and τ + γ. Mathematically the transversal coupling between the hole chains is fully described by a single parameter γ, which physically represents the multiple scattering of the gap-SPP in the transversal MIM layers. The model predictions for the fishnet effective index are shown with the solid red curves in Fig. 4-6. They are found to quantitatively capture all the major features of the rigorously calculated data (circles), such as the broadband negative n_{eff} for λ > 1.7 μm, the increase (in absolute value) of $\mathrm{Re}(n_{eff})$ with the wavelength, and the low-loss band for 1.8 < λ < 2 μm followed by a rapid increase of the loss at longer wavelengths. Even the band-gap for 1.45 < λ < 1.75 μm is accurately predicted.

Further simple algebraic derivations lead to the calculation of the transfer-matrix eigenvectors, i.e., the field of the fishnet Bloch modes. For the forward-propagating mode related to the $\exp(i k_0 n_{eff} a_z)$ eigenvalue, we obtain

$$\frac{B_{m,n}}{A_{m,n}} = \frac{(\rho+\gamma)v}{1-(\tau+\gamma)v\exp(i k_0 n_{eff} a_z)}, \tag{4-12a}$$

$$\frac{C_{m,n}}{A_{m,n}} = \frac{\gamma v^{1/2}}{2\alpha u^{1/2}}\left[1+\frac{B_{m,n}}{A_{m,n}}\exp\left(\mathrm{i}k_0 n_{\mathrm{eff}} a_{\mathrm{z}}\right)\right]. \qquad \text{(4-12b)}$$

These two equations fully characterize the field inside the holes and in the dielectric layers.

4.4 Origin of the negative index

In addition to providing semi-analytical expressions for the fishnet effective index, the main strength of the microscopic model is to separate the contributions from the longitudinal (vertical) and transversal (horizontal) channels.

4.4.1 *Longitudinal (vertical) channel*

The dispersion curve of a single *z*-periodic hole-chain, Eq. (4-3) and dashed blue curves in Fig. 4-6, only reflects the longitudinal contribution and shows a large damping with a small negative index. This contribution alone cannot explain the negative effective index of the fishnet given by the circles in Fig. 4-6.

4.4.2 *Transversal (horizontal) channel*

The transversal coupling mediated by gap-SPPs [described by the multiple-scattering parameter γ in Eq. (4-11)] clearly appears as the origin for the appearance of a negative index with low loss, see Fig. 4-6.

In the fluidic-like interpretation, the reduction of the damping, $\mathrm{Im}(n_{\mathrm{eff}}) << \mathrm{Im}(n_{\mathrm{pc}})$, is understood by considering that the gap-SPPs, which leak away in the case of a single *z*-periodic chain Fig. 4-6(i2), are recycled back into nearby chains in the fishnet Fig. 4-6(i3).

The increase (in absolute value) of $\mathrm{Re}(n_{\mathrm{eff}})$ is more delicate to analyze; it is due to a transversal resonance at $\lambda \approx 2$ μm that boosts the excitation of gap-SPPs and thus enhances the negativity that was only emerging in the hole-chain. Figure 4-8(a)

shows the resonant shape of $|\gamma|^2$; the pole of γ physically corresponds to the resonance of a periodic MIM waveguide coupled to two 2D-arrays of semi-infinite vertical holes, see the inset. The hole modes do not carry energy away since they are below cut-off and thus the quality factor of the resonance is only limited by absorption.

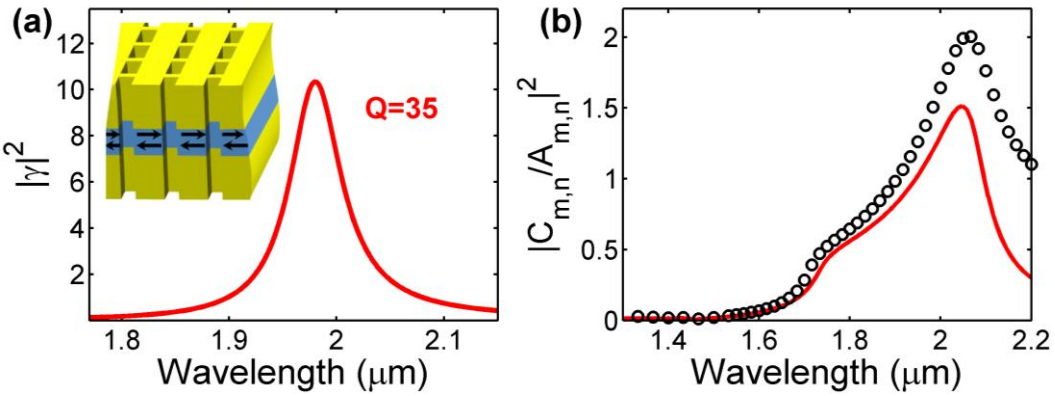

Figure 4-8. Transversal resonance responsible for the negative-index appearance. (**a**) Resonance spectrum of $|\gamma|^2$. Inset: periodic MIM waveguide perforated by semi-infinite metallic holes. (**b**) Spectrum of the normalized gap-SPP intensity $|C_{m,n}/A_{m,n}|^2$ of the fishnet Bloch mode. Good agreement is achieved between the model predictions (red curve) and the values extracted from a fully-vectorial calculation of the fishnet Bloch mode (circles).

For subwavelength scatterers (the hole chains in the present study) with nearly identical backward and forward scattering strengths, one has $r_{sp} \approx 1 - t_{sp}$ [Liu10b], thus $|r_{sp} + t_{sp}| \approx 1$ in the denominator of γ. So the quality factor Q of the resonance is mainly determined by the gap-SPP damping, and we have

$$Q \approx \frac{\mathrm{Re}(n_{sp})}{2\mathrm{Im}(n_{sp})}. \tag{4-13}$$

In the spectral range of interest, $\mathrm{Re}(n_{sp})$ and $\mathrm{Im}(n_{sp})$ are almost constant values close to 2 and 0.03, respectively, so that the Q is about 35. This quantitatively agrees with $\lambda_{peak}/\Delta\lambda$ of the $|\gamma|^2$ curve, where λ_{peak} is the resonant wavelength of $|\gamma|^2$ and $\Delta\lambda$ is the full-width-at-half-maximum (FWHM).

4.4.3 *Quantifying the "magnetic" resonance*

In the fishnet, every MIM waveguide is vertically coupled through the holes to two other adjacent MIM waveguides, and the narrow resonance of γ reflects into a broader enhancement of the gap-SPP field. This interpretation is supported by the red curve in Fig. 4-8(b), which shows the normalized gap-SPP intensity $|C_{m,n} / A_{m,n}|^2$, calculated with Eq. (4-12b), ($D_{m,n} = C_{m,n}$ for normal incidence). The model predicts that $|C_{m,n} / A_{m,n}|^2$ increases by a factor 10 as the wavelength varies from 1.7μm to 2μm, where a maximum is reached. This prediction is found to be in good agreement with fully-vectorial computations (circles) and quantitatively supports our classical understanding that attributes the "magnetic" response of fishnets to a resonant anti-symmetric current distribution in the MIM stack [Sha07, Val08, Mar08b, Zho09].

Although the role the gap-SPPs in the negative index of fishnet metamaterials has already been discussed in the literature [Mar08b], the microscopic model evidences that the gap-SPPs are resonantly excited (because of multiple scattering) and it allows to quantify this resonance. Additionally, the model allows us to calculate the $1/e^2$ decay length of the gap-SPP resonance, which is found to be delocalized over about 4 periods.

4.5 Numerical analysis

We provide in this section some technical elements concerning the numerical calculations presented in previous sections. Section 4.5.1 gathers technical elements on the three-dimensional (3D) fully-vectorial computations of the scattering coefficients used in the coupled-wave theory. We emphasize that such 3D calculations on subwavelength metallic structures is a difficult numerical task and we show in Section 4.5.2 some convergence tests that have been performed to check the accuracy of our results.

4.5.1 *Numerical analysis*

Our theoretical results rely on a series of computational results obtained with 3D fully-vectorial calculations. Technical elements and related references are provided hereafter. Our modeling of the fishnet mainly contains two kinds of calculations, one is the calculation of the fishnet Bloch mode, and the other is the calculation of scattering parameters (α, τ, ρ, t_{sp} and r_{sp}). Concerning the former, more details are provided in Section 2.2 of Chapter 2. In the following, the calculation of scattering coefficients is provided in details.

As discussed in the above, the scattering coefficients α, τ, ρ, t_{sp} and r_{sp} play a key role in our theoretical analysis. Actually, attention should also be paid to the numerical calculation of these coefficients, which involves some special numerical techniques.

The scattering processes are calculated with the aperiodic Fourier Modal Method (a-FMM) [Sil01]. In the computation, the forward- and backward-propagating TE_{01} and gap-SPP modes in the metallic hole chain and in the MIM waveguide are calculated as eigenstates of the transfer matrix associated to an artificially periodized structure surrounded by Perfectly-Matched-Layers (PMLs) [Hug05b, Che94]. The reflection and transmission coefficients ρ, τ, r_{sp} and t_{sp} are derived from a S-matrix calculation in the some artificially periodized structure.

To extract the coupling coefficient α, we refer to the completeness theorem of the normal modes set used in waveguide theory [Sny83, Vas91]. The theorem, which provides a potent electromagnetic representation of light propagation in systems composed of waveguide stacks, states firmly that any transverse field pattern of any waveguide can be decomposed as a linear combination of forward- and backward-traveling bounded and radiative modes of the section under consideration. Because of orthogonality relations between the modes [Sny83], we can obtain the contribution of the TE_{01} super-mode in the field scattered in the metallic hole chain for an incident gap-SPP mode by calculating an overlap-integral between the scattered field in the metallic hole chain and the normalized field of the TE_{01} super-mode

$$\alpha_2 = \iint_S (\mathbf{E}_{TE01}\times\mathbf{H}_{sca} - \mathbf{E}_{sca}\times\mathbf{H}_{TE01})\bullet d\mathbf{S}, \qquad (4\text{-}14)$$

where the integral is performed on the transverse cross-section of the metallic hole chain, the subscript 'TE01' and 'sca' denote the field of TE_{01} mode and the scattered field induced by the incident gap-SPP mode respectively. In Eq. (4-14) the TE_{01} super-mode and gap-SPP mode are both normalized so that $2 = \iint_S \mathbf{E}_{mode} \times \mathbf{H}_{mode} \bullet d\mathbf{S}$. The coupling coefficient α_1 of the reverse scattering process can be obtained by a similar overlap-integral between the scattered field in the dielectric gap for an incident TE_{01} super-mode and the field of the normalized field of the gap-SPP mode. Closely related details on the theoretical and numerical concepts supporting the calculation of SPP scattering coefficients can be found in [Lal05, Lal09].

Mode orthogonality and reciprocity in dissipative waveguides. We provide hereafter some theoretical points concerning waveguide mode orthogonality (WMO). For a more detailed derivation, one may refer to Section 3.3 of Chapter 3, where the Bloch mode orthogonality that is similar to the WMO has been established. The overlap-integral in Eq. (4-14) directly stems from Lorentz reciprocity theorem [Sny83]. Usually, this theorem is founded in the sense of the Poynting vector, i.e., with E×H* products that ensure energy conservation. Nevertheless, for dissipative materials such as noble metals at optical frequencies, the classical conjugated form of Lorentz reciprocity theorem is no longer sound and one has to lean on the unconjugated form with E×H pseudo-Poynting products [Sny83]. All modes considered in this work (those supported by the metallic hole chain as well as those supported by the MIM waveguide) satisfy orthogonality relations with E×H products. Note that normalization plays a pivotal role in the coupled-mode equations

$$1/2 \iint_S (\mathbf{E}_m \times \mathbf{H}_m) dS = 1, \qquad (4\text{-}15)$$

where $\mathbf{E}_m$ and $\mathbf{H}_m$ are the transverse electric and magnetic fields of the m^{th} waveguide mode and the surface integral runs over the waveguide cross-section S. The coupling coefficient α between the metallic hole-chain TE_{01} super-mode and the MIM channel gap-SPP mode is obtained for this specific normalization.

According to Lorentz reciprocity theorem, the two coupling coefficients α_1 and α_2 corresponding to the two opposite scattering process depicted in Figs. 4-1(b) and (c) should be equal. We have checked that our numerical results satisfy reciprocity with a relative error of 1%, see Fig. 4-5(c).

4.5.2 *Numerical accuracy and convergence*

There is a slight difference (see Fig. 4-6) between the model predictions for the fishnet effective index n_{eff} and the fully-vectorial computational results obtained with the RCWA. In this section we check that the difference does not result from any artifact due to numerical inaccuracies.

In our computations, numerical inaccuracies originate from the inevitable truncation of Fourier series for numerical purposes since we rely entirely on Fourier Modal Method (either periodic or aperiodic). In order to evaluate the precision of the computational results, convergence tests have been performed by progressively increasing the number N_x or N_y of Fourier coefficients retained in the computation [Fourier series goes from $-(N-1)/2$ to $+(N-1)/2$]. Figure 4-9 shows the convergence curve of Re(n_{eff}) and Im(n_{eff}) calculated by the microscopic model at $\lambda = 2$ µm (where we can observe clearly in Fig.4-6 the existence of minor difference between model prediction and fully-vectorial calculation). For $N_x \times N_y = 71 \times 51$ Fourier harmonics, the relative error can be expected to be in the range of 1%. We have checked that all computational results show similar numerical accuracy (not shown here). In order to achieve such good numerical performances for metallo-dielectric structures where the electromagnetic field varies very rapidly at the metal boundaries, the accuracy of the a-FMM has been improved by using real coordinate-transforms around the metal/dielectric interfaces, as described in [Bes07].

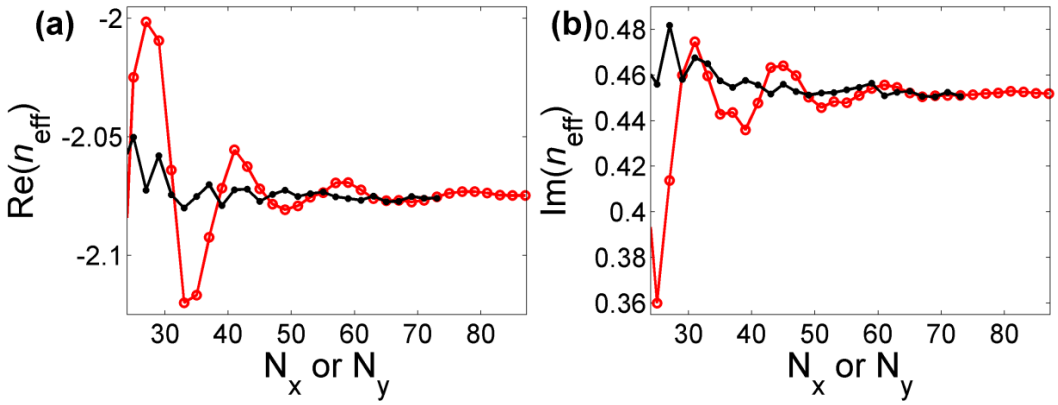

Figure 4-9. Convergence tests for Re(n_{eff}) (**a**) and Im(n_{eff}) (**b**). The red circles show the convergence as a function of N_x for $N_y = 41$ while the black dots show the convergence as a function of N_y for $N_x = 61$.

Since the slight difference between model prediction and fully-vectorial calculation does not come from any numerical inaccuracies, it should be due to the approximation made in the model derivation. We checked that this difference is mainly due to the finite thickness of the metallic layer of a realistic fishnet, through which the gap-SPP modes confined in different layers couple. This effect is not taken into account in the model, because in the model we assume the gap-SPP is confined in a MIM waveguide with infinitely thick metallic cladding. Details of this effect can be found in the following Chapter (Section 5.4), where we attempt to engineer the fishnet properties by varying the geometrical parameters.

4.6 Conclusion

In summary, light transport in fishnet negative-index metamaterials at optical frequencies has been analyzed with a comprehensive and accurate model. In addition to providing the first analytical treatment of negative-index metamaterials at optical frequencies, the model shines new light on how a negative index is formed. In contrast to previous works that rely on a direct extraction of macroscopic quantities [Smi06, Zha06, Roc08, Yan10, Pet08, Vyn09, Smi02], the present model relies on a "microscopic" formalism that tracks the local transport of electromagnetic fields in the structure. We hope that such an approach may be helpful not only to further design negative-index metamaterials at optical frequencies, but also to engineer complex metallo-dielectric surfaces in general [Kao11].

Chapter 5

Applications of the microscopic model: Engineering the optical properties of fishnet metamaterials

In Chapter 4, we have developed a "microscopic" model based on surface plasmon scattering that provides an accurate semi-analytical expression for the effective index n_{eff} of fishnet metamaterials. The microscopic model successfully explains the origin of low-loss negative-index in fishnets. Furthermore, it possesses a broad flexibility for tailoring geometric and material parameters. In this Chapter we use the microscopic model for engineering the optical properties of fishnet metamaterials. We especially focus on tuning the spectrum of negative index and on reducing the losses (the energy dissipated by absorption in the metal that reflects into the imaginary part of the effective index). In particular, for the purpose of loss reduction, we extend the microscopic theory to gain-assisted fishnets, i.e., fishnet structures that incorporate some amplification for compensating the absorption losses. We find that the intricate problem of loss-compensation in a fishnet metamaterial can be essentially reduced to the simpler problem of loss-compensation of gap-SPP modes supported by metal-insulator-metal waveguides. A discussion of the limitations of our microscopic model is included at the end of the Chapter as a complementary study.

5.1 Introduction

In general, the study of metamaterials comprises some important tasks: designing and engineering the metamaterial, understanding the underlying physics, fabricating the structure, characterizing its optical properties…. Among them, the former two are reciprocally beneficial. Particularly, once the physics of light propagation in a metamaterial is well understood, one is able to tailor, on purpose, the optical properties. For instance, when the fundamental principles of metaatoms are disclosed, the properties of the metamaterial formed with them can be intentionally engineered by tailoring the metaatoms. Well-known examples are the metamaterials made of split-ring resonators [Pen99]. The lumped elements model of these resonators [Bri02, Bri04, Zho05, Ish05, Jep11] has allowed people to grasp the key parameters that determine the resonance frequency, namely the resonator size. Thus, by shrinking the size of split-ring resonators, people have demonstrated strong magnetic response over a broad spectral range from microwaves [Smi00] to THz [Kat05] and more recently in the near-infrared [Liu08a, Ser09].

In Chapter 4, the physics of optical negative-index fishnet metamaterials has been quantitatively explained by a semi-analytical microscopic model relying on surface-plasmon coupled-mode equations. This model shines new light on the physical origin of negative refraction in fishnets by analytically handling the key parameters that impact the resonant excitation of gap-SPPs. According to the model, we can mainly attribute the broad-band negative index of fishnets to this plasmon resonance, which can be phenomenologically considered as a magnetic resonance inducing negative-valued permeability ($\mu_{eff} < 0$). We take advantage of the model analyticity for engineering the optical properties of fishnet metamaterials.

The model evidences that some parameters (the gap-SPP propagation constant n_{sp} and the x-period a_x) determine the strength and the spectral range of the magnetic resonance. Those parameters can be tuned by tailoring the fishnet geometry and the materials composing it. For any practical application, the functional spectrum and the absorption losses of optical metamaterials are two crucial issues, on which we mostly concentrate in the following. We demonstrate that, by varying the geometric parameters or the refractive index of the dielectric material, one can moderately shift the spectral range of negative index. On the other hand, we show that engineering the geometric and/or material parameters does not allow to

significantly reducing the absorption losses. The microscopic model clearly evidences that the only solution to reduce the fishnet losses is to compensate the attenuation of the gap-SPP modes propagating in the dielectric layers. In particular, this loss compensation can be realized by incorporating some optical amplification in the dielectric material [Xia10, Fan09, Wue09]. We investigate such active fishnets with the model.

Throughout the discussions in this Chapter, the microscopic model plays a key role. Its accuracy is further verified with a series of full-wave simulations. Note that we solely change the parameters of the dielectric layers (thickness, refractive index or incorporation of gain), leaving the size of metallic holes unvaried. In other words, we can say that the spectrum of negative permittivity ($\varepsilon<0$) is fixed [Mar08b, Gar09]. Passive fishnet structures with different geometric and material parameters are studied in Section 5.2 and the active fishnet structures containing a gain medium are investigated in Section 5.3. Finally, in Section 5.4, the limitations of the model are studied in details.

5.2 Engineering the fishnet geometrical parameters

In Chapter 4, the origin of the negative refraction in fishnet metamaterials has been analyzed with a microscopic model that provides a semi-analytical expression for the effective index n_{eff}

$$\cos(k_0 n_{\text{eff}} a_z)=\frac{(\tau+\gamma)^2 v^2 - (\rho+\gamma)^2 v^2 + 1}{2(\tau+\gamma)v}, \tag{5-1}$$

where the key parameter γ that gathers the multiple scattering of gap-SPPs in the dielectric layers is given by

$$\gamma = \frac{2\alpha^2 u}{1-\left(t_{sp}+r_{sp}\right)u}, \tag{5-2}$$

with $v = \exp(ik_0 n_h a_z)$ and $u = \exp(ik_0 n_{sp} a_x)$. In Eqs. (5-1) and (5-2), τ, ρ, α, r_{sp} and t_{sp} are the scattering coefficients of plasmonic modes inside the fishnet mesh. The normalized propagation constant of these modes (the TE_{01} supermode propagating in the metallic holes and the gap-SPP mode propagating in the dielectric layers) are

given by n_h and n_{sp} respectively and a_z and a_x are the fishnet periods along the z and x-directions. Details concerning the derivation of those equations can be found in Chapter 4.

The resonance of the parameter γ corresponds to a resonant excitation of gap-SPP modes in the dielectric layers. A very important parameter to evaluate the strength of this horizontal resonance is its quality factor

$$Q \approx \frac{\mathrm{Re}(n_{sp})}{2\mathrm{Im}(n_{sp})}. \tag{5-3}$$

In the denominator of γ, the propagation delay of gap-SPPs $u = \exp(ik_0 n_{sp} a_x)$, together with the phase of $(t_{sp} + r_{sp})$, determines the spectral position of the resonance. So the resonance can be shifted spectrally by tuning $\mathrm{Re}(n_{sp})$ or the period a_x. As we have seen in previous Chapter, the fishnet exhibits a negative index only in the spectral range where simultaneously the TE_{01} mode is below cutoff and the gap-SPPs resonate. As a result, one is allowed to tune the spectral range of negative index by tuning $\mathrm{Re}(n_{sp})$ or the period a_x. Additionally, the absorption losses in fishnets are directly related to the strength of the gap-SPP resonance. Thus by reducing $\mathrm{Im}(n_{sp})$, the Q-factor is increased and the losses associated to the negative index are reduced.

There exist different ways to change the propagation constant of a Metal-Insulator-Metal waveguide [Eco69], such as changing the thickness or the refractive index of the dielectric core. Note that a_x is a free parameter in the model, i.e., when all the scattering parameters are determined, we can obtain the effective index of fishnets with different periods a_x fully analytically without further calculations. On the other hand, in the case where we change the thickness or the refractive index of the dielectric layer, the scattering parameters need to be recalculated to get the new effective index.

5.2.1 *Impact of the transversal period a_x*

In the two scattering processes depicted in Figs.4-1(b) and (c), fixed parameters include the hole size (w_x and w_y), y-period a_y, dielectric spacer thickness h_d, and the constituent materials. Clearly the transversal x-period a_x is a free parameter, and its impact on the negative index can by studied analytically by the microscopic model. This can efficiently speed up the engineering process.

The period a_x only affects the delay-term u in the denominator of the multiple scattering term γ [Eq. (5-2)]; the wavelength of the resonance of $|\gamma|^2$ is determined by the phase matching condition $\arg(r_{sp} + t_{sp}) + k_0 n_{sp} a_x = 2\pi$. Applying the scattering parameters obtained in Chapter 4 into the microscopic model, we analytically calculate fishnets with three different x-periods, $a_x = 800$, 860 and 900 nm. The model predictions (solid curves) agree quantitatively with the fully-vectorial calculation results (circles), see Figs.5-1(a) and (b). Note that the fishnet with $a_x = 860$ nm is the one studied in Chapter 4.

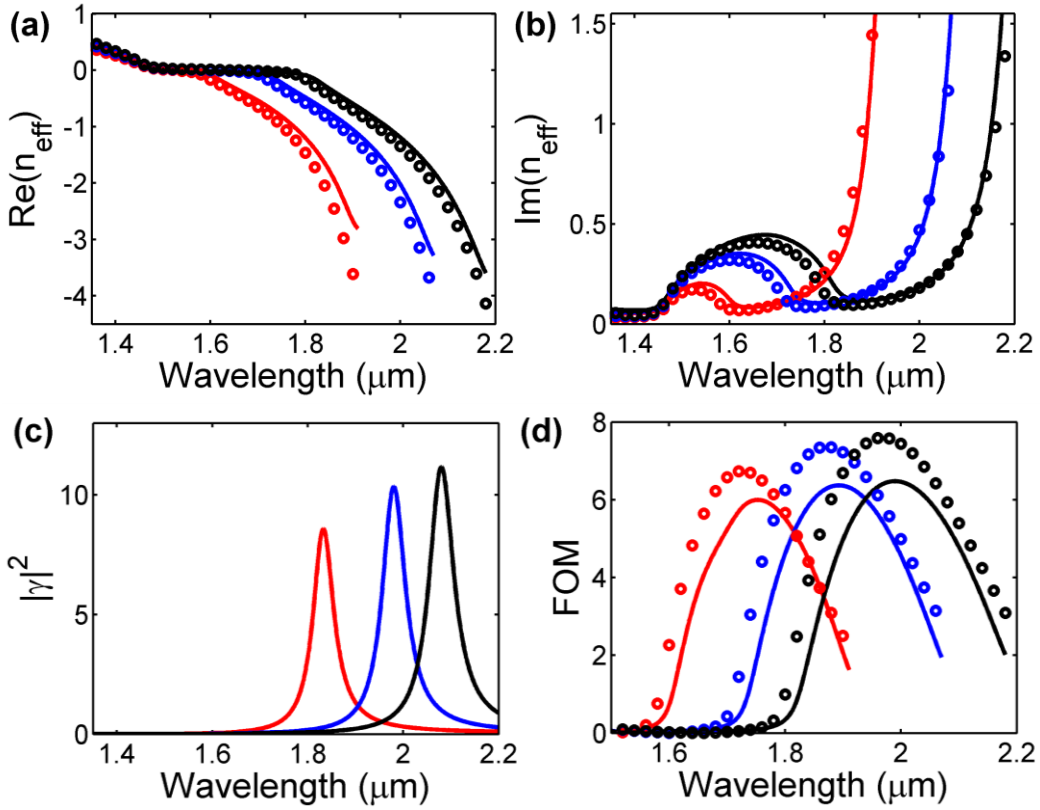

Figure 5-1. Real (**a**) and imaginary (**b**) parts of the fishnet effective index for different x-periods, $a_x = 800$ nm (red), 860 nm (blue) and 900 nm (black). Corresponding multiple-scattering parameter $|\gamma|^2$ (**c**) and Figures of Merit $|\mathrm{Re}(n_{eff})|/\mathrm{Im}(n_{eff})$ (**d**). In (c), the three curves have the same quality factor, $Q \approx 35$. In (a), (b) and (d), the model predictions and the results of fully-vectorial calculations are shown as solid curves and circles, respectively. Note that the fishnet with $a_x = 860$ nm is the one analyzed in Chapter 4.

Since n_{sp} is fixed for those three fishnet structures (the almost dispersionless n_{sp} is equal to 1.98+0.028i in the related spectrum), increasing (decreasing) the period a_x leads to a red (blue) shift of the resonance of γ [Fig.5-1(c)]. The spectral shift of the gap-SPP resonance finally changes the appearance of negative index in

the spectra as can be seen in Fig. 5-1(a). In addition, since the change of a_x does not affect the gap-SPP propagation constant n_{sp}, the Q factor of the $|\gamma|^2$ resonance and the peak value of the figure of merit [FOM=$|\mathrm{Re}(n_{eff})|/\mathrm{Im}(n_{eff})$] are roughly the same for the three fishnets, see Figs. 5-1(c) and (d). Additionally, when a_x (= 860 nm) decreases (or increases) by about 50 nm (~6%), the resonance wavelength shifts by about 100 nm, from 1.98 μm to 1.85 μm (or 2.1 μm) exhibiting a sensitive response.

As a brief conclusion, by tuning the transversal x-period a_x properly, a desired value of effective index n_{eff} can be obtained for a fixed wavelength. The microscopic model can help effectively in the search for such a proper value.

5.2.2 *Impact of the dielectric layer thickness*

An increase of the dielectric spacer thickness h_d induces a lowering of both $\mathrm{Re}(n_{sp})$ and $\mathrm{Im}(n_{sp})$, as a larger part of the SPP field is located in the dielectric region of the Metal-Insulator-Metal structure. Since the gap-SPP resonance is sensitively dependent on the propagation delay term u as observed in previous section, we can expect that varying h_d could shift the spectrum of negative effective index effectively and modify the level of loss in the meantime.

Calculations of the effective index of three fishnets with different dielectric (MgF_2) spacer thicknesses (h_d = 40, 50 and 75 nm) are performed see Figs. 5-2(a) and (b). The fishnet with h_d = 50 nm is the one discussed in Chapter 4 and the other two fishnets share the same parameters except for h_d. The model predictions and the rigorous calculations show a quantitative agreement. In the denominator of γ, the term ($t_{sp} + r_{sp}$) does not change much compared with the variation of normalized propagation constant n_{sp}, and as a result the spectral position of the $|\gamma|^2$ resonance is still mainly determined by the propagation delay term $u = \exp(ik_0 n_{sp} a_x)$. So the increase (or decrease) of the dielectric spacer thickness, which reduces (or raises) the value of n_{sp}, results in the blue (red)-shift of the $|\gamma|^2$ resonance [Fig. 5-2(c)] and accordingly the blue (red)-shift of the negative index spectrum.

For h_d=40, 50 and 75 nm, the nearly dispersionless gap-SPP propagation constant are n_{sp}=2.10+0.035i, 1.98+0.028i and 1.80+0.021i. Apparently, when h_d increases, the attenuation $\mathrm{Im}(n_{sp})$ of the gap-SPP drops more rapidly than $\mathrm{Re}(n_{sp})$. As a result the Q factor of the gap-SPP resonance increases, see Fig. 5-2(c). Accordingly, the FOM of fishnet with a thicker MgF_2 layer shows slightly larger peak values than

the fishnets with thinner ones; see Fig. 5-2(d). So by increasing the dielectric spacer thickness, one can slightly reduce the absorption losses in the fishnet.

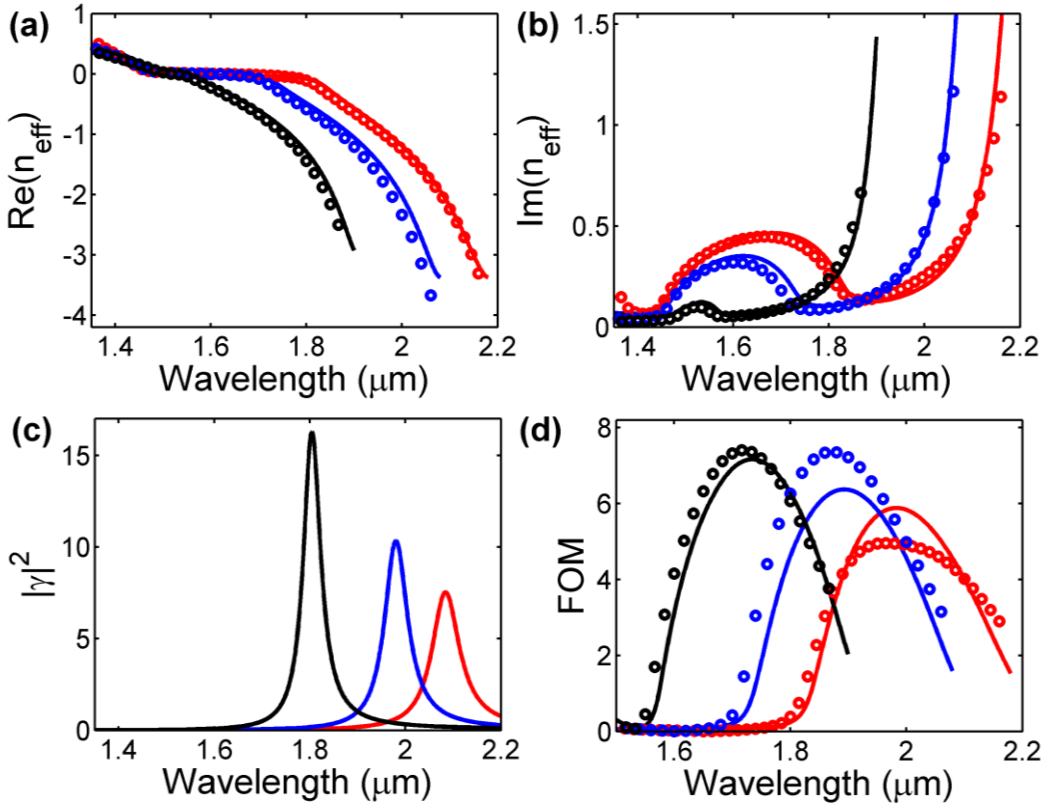

Figure 5-2. Real (**a**) and imaginary part (**b**) of the fishnet effective index for different dielectric spacer thickness h_d = 40 nm (red), 50 nm (blue) and 75 nm (black). The *x*-period is fixed as a_x = 860 nm. Corresponding multiple-scattering parameter $|\gamma|^2$ (**c**) and Figures of Merit $|\mathrm{Re}(n_{eff})|/\mathrm{Im}(n_{eff})$ (**d**). In (c), the three Q factors are 30 (red), 35 (blue) and 40 (black) respectively. In (a), (b) and (c), the model predictions and the fully-vectorial calculations are shown as solid curves and circles, respectively.

As already analyzed in Section 5.2.1, a change of the transversal *x*-period could shift the region of negative index. Thus if the *x*-period and the h_d are both changed in a proper manner, then the spectral range of negative index can remain unchanged but with a modified damping term $\mathrm{Im}(n_{eff})$. For example, three fishnet designs with geometrical parameters (a_x = 821 nm h_d = 40 nm), (a_x = 860 nm h_d = 50 nm) and (a_x = 941 nm h_d = 75 nm) show a negative index in the same spectrum, but with different attenuations $\mathrm{Im}(n_{eff})$. Note that the second fishnet is the same as the one studied in Chapter 4. Because the level of loss is generally determined by the Q factor of the gap-SPP resonance, the fishnet with larger h_d (= 75 nm) shows higher Q. Its loss is about 60% of the one with h_d = 40 nm in the spectral domain of negative index

(1.75 < λ < 1.95 μm). This indicates that the loss of a passive fishnet structure can be moderately optimized by modulating the geometrical parameters appropriately while keeping a desired Re(n_{eff}) value in a desired spectrum.

5.2.3 *Impact of the dielectric refractive index*

Like its thickness, the refractive index n_d of the dielectric spacer mainly affects the propagation constant n_{sp} of the gap-SPP mode. Hereafter calculations of a fishnet with SiO_2 as dielectric layer (n_d = 1.5) are compared with the fishnet analyzed in Section 5.2.2 with a MgF_2 dielectric spacer (n_d = 1.38). All the other parameters are the same as the fishnet in Chapter 4.

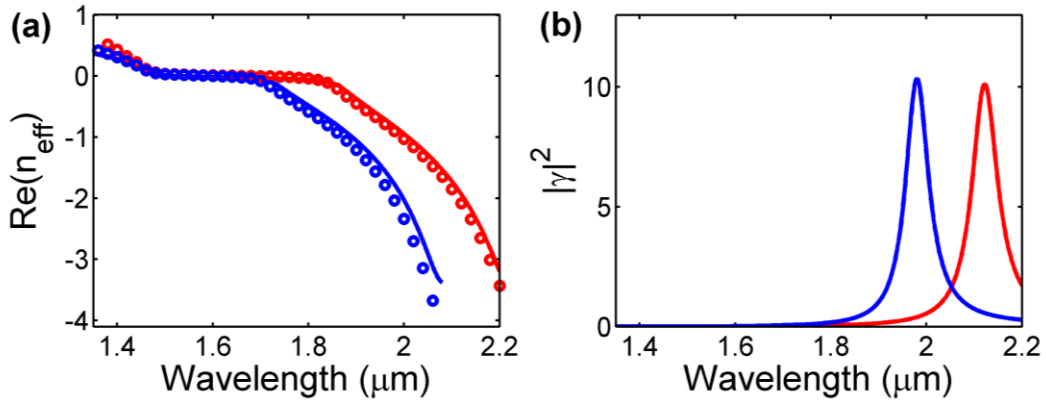

Figure 5-3. (**a**) Real part of the effective index of the fundamental Bloch mode for different dielectric materials, SiO_2 (n_d = 1.5, red) and MgF_2 (n_d = 1.38, blue). The model predictions and fully-vectorial calculations are shown as solid curves and circles, respectively. (**b**) Corresponding multiple-scattering parameter $|\gamma|^2$. The Q factors of the resonance are the same, Q ≈ 35.

When the MgF_2 dielectric layer is replaced by SiO_2, the normalized propagation constant n_{sp} of the gap-SPP mode increases slightly from n_{sp} = 1.98 + 0.028 to n_{sp} = 2.16 + 0.031. So the region of negative index experiences a red-shift, see Fig. 5-3(a). Basically, these two fishnets share the same level of dissipation because they possess the same Q factor (≈ 35) as shown in Fig. 5-3(b).

The modification of the dielectric material is a degree of freedom to design the fishnet with a desired effective index. Especially, when designing a super-cell fishnet

structure [Pau10], optimization of the spacer thickness and dielectric constant is more preferable and experimentally feasible.

To summarize Section 5.2, for passive fishnet metamaterials, geometric or material tailoring can tune the spectrum of negative index effectively since the gap-SPP resonance is sensitive to the phase delay of the gap-SPP in the transversal (horizontal) channel. However, loss engineering through this process is restricted by the inherent absorption in metals at visible and near-infrared frequencies. This implies that the loss of plasmonic nanostructures including metamaterials is an inevitable and tough problem. In the next section, gain-assisted fishnets are analyzed in detail, which may be considered as an ultimate solution to improve the performance of optical metamaterials.

5.3 Incorporation of gain medium for loss-compensation

Reducing the attenuation of negative-index metamaterials operating in the visible and near-infrared is crucial and the issue of loss compensation with gain media has recently received much attention [Sha10, Fan09, Wue09]. Because of the analytical treatment, the microscopic model constitutes a powerful tool to study and design negative-index fishnet metamaterials with embedded gain in the dielectric layers.

The microscopic model stresses the importance of the transversal resonance in the appearance of negative index. We therefore start by considering the impact of gain on the resonance lifetime of the multiple scattering parameter γ. Hereafter we restrict the study to the low-loss band, $1.75 < \lambda < 1.95$ μm, and we assume that the amplification process can be simply analyzed by a phenomenological MgF_2 refractive index $n_d = 1.38 - ig$ with a constant negative imaginary part. Consistently with previous studies [Sha10, Fan09, Wue09], we choose $0 < g < 0.02$. These values are small enough to ensure a linear operation for which self-consistent calculations are not strictly required [Fan09].

We first emphasize that, for small gain values considered in this work, all the scattering coefficients (τ, ρ, α, r_{sp}, t_{sp}) in Eq. (5-1) weakly depend on gain. This has been checked by numerical calculations (not shown here). The calculations performed in the passive case, see Chapter 4, can thus be directly used to analyze fishnets with embedded gain media and no further computations are needed. In

addition, the phase delay term in the metallic holes $v = \exp(ik_0 n_h a_z)$ is unaffected since we incorporate gain only in the dielectric layers. Therefore, the sole parameter that has to be calculated in the presence of amplification is the gap-SPP normalized propagation constant n_{sp}. Thanks to the model, the intricate problem of loss-compensation in a fishnet metamaterial essentially reduces to a much simpler problem of loss-compensation in a plasmonic waveguide, namely a Metal-Insulator-Metal slab waveguide.

As anticipated, due to the decrease of the gap-SPP attenuation $\mathrm{Im}(n_{sp})$, see Fig. 5-4(a), the transversal resonance is strengthened in the presence of small gain, and the Q-factor rapidly increases with g, see Fig. 5-4(b). It should be stressed that gain negligibly influences $\mathrm{Re}(n_{sp})$ but largely affects the characteristic length of the transversal resonance that extends over 30 cells for $g = 0.022$, instead of only 4 cells for a passive structure with $g = 0$.

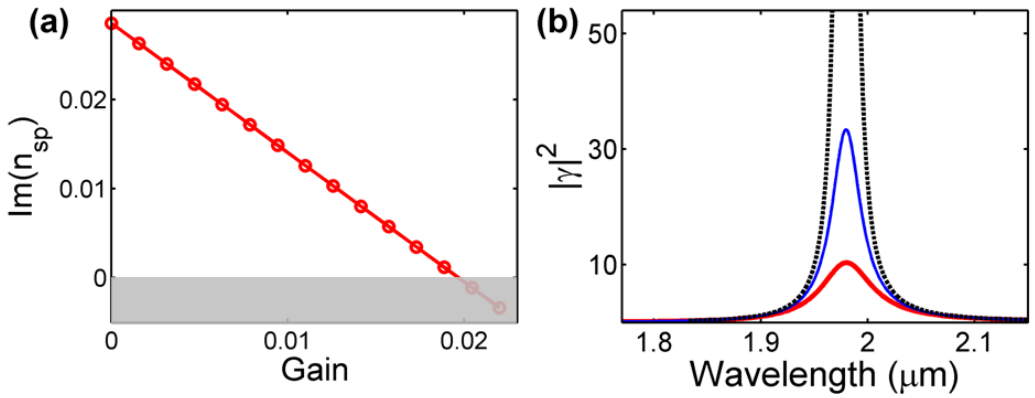

Figure 5-4. (a) Decrease of the gap-SPP attenuation with the gain parameter g ($\lambda = 1.9\mu m$). Amplified gap-SPPs are obtained for $\mathrm{Im}(n_{sp}) < 0$ in the grey region. (**b**) Impact of the gain g on the resonance of the multiple scattering parameter $|\gamma|^2$, $g = 0$ (bold red), $g = 0.01$ (thin blue) and $g = 0.022$ (dotted-black). The corresponding Q-factors are 35 (red), 60 (blue) and 800 (black) respectively.

We then study the loss-compensated fishnet effective index, which is still given by Eq. (5-1) in the presence of small gain. As shown in Fig. 5-5(a), $\mathrm{Re}(n_{eff})$ is insensitive to the modest gain increase and remains negative. More importantly, we find that the attenuation $\mathrm{Im}(n_{eff})$ is significantly lowered as g increases, see Fig. 5-5(b). When the absorption losses due to the gap-SPP propagation are exactly compensated by amplification, i.e., for $\mathrm{Im}(n_{sp}) \to 0$, the resonance linewidth of $|\gamma|^2$ becomes limited by the scattering losses. When increasing the gain further, the gap-SPP becomes slightly amplified, see Fig. 5-4(a), and can partly compensate the scattering losses. For $g = 0.022$, Eq. (5-1) predicts that the fishnet becomes an

amplifying medium [Im(n_{eff}) < 0] for 1.75 < λ < 1.85 μm, as shown by the black curve in Fig. 5-5(b). All these model predictions are confirmed by fully-vectorial calculations, as shown by circles in Fig. 5-5.

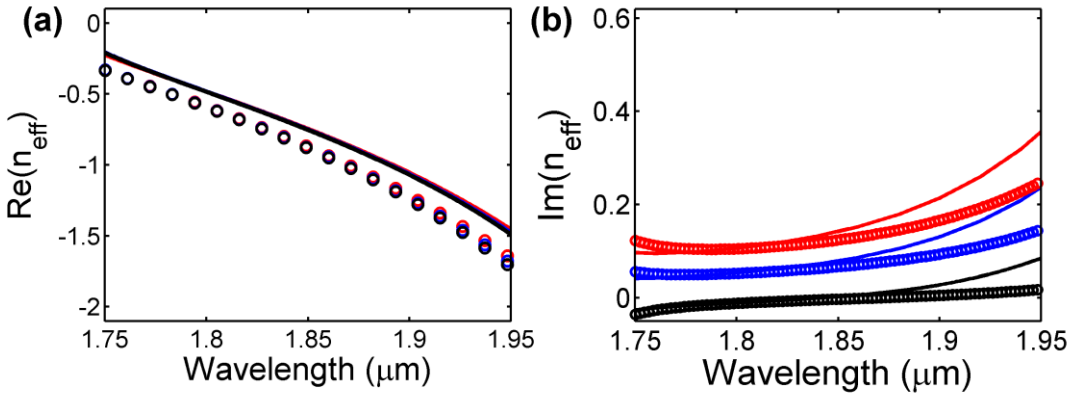

Figure 5-5. Real (**a**) and imaginary part (**b**) of the fishnet effective index for different gain values, g = 0 (red), g = 0.01 (blue) and g = 0.022 (black). The model predictions and fully-vectorial calculations are shown as solid curves and circles, respectively.

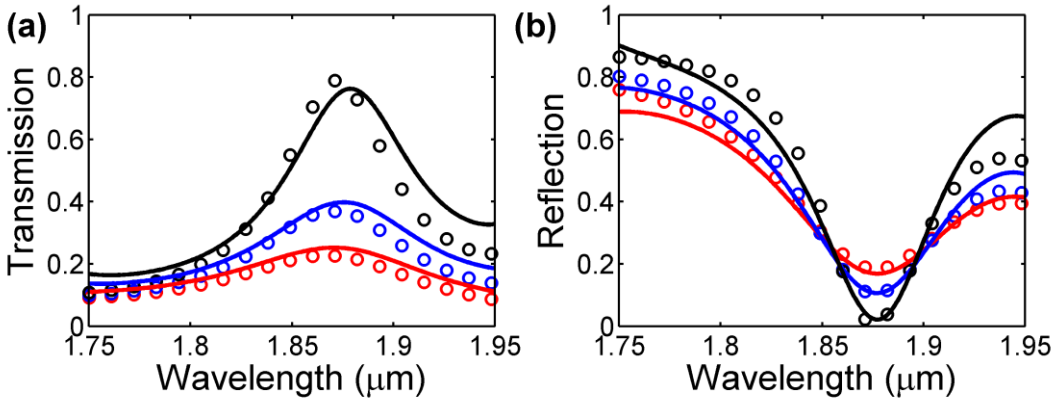

Figure 5-6. Loss compensation with gain in a finite-thickness fishnet slab composed of 5 unit cells ($d = 5a_z$). (**a**) Transmission and (**b**) reflection spectra for the same g's values as in Fig. 5-5. In (a) and (b), the model predictions are shown with solid curves and fully-vectorial calculations are shown with circles. For the sake of clarity, in (a) and (b), the model predictions are blue-shifted by 20 nm to compensate for the slight offset in Re(n_{eff}) due to the small metal thickness, see Fig. 5-5(a).

In a second step, we have tested all those predictions obtained for the fundamental Bloch mode of an infinite fishnet by analyzing a real situation with a finite-thickness fishnet slab composed of 5 unit cells stacked in the z-direction and

illuminated from air at normal incidence. Figure 5-6 compares the specular transmission T and reflection R, obtained either by a Fabry-Perot model (solid curves) assuming that the energy transport through the fishnet slab is solely mediated by the fundamental Bloch mode with an effective index $n_{\mathrm{eff}}(g)$ (see more details in Chapter 2 or in [Yan10]) or by fully-vectorial calculations (circles) obtained with the Rigorous Coupled Wave Analysis [Li97]. Except for a systematic spectral shift that has been removed and that is due to a slight offset of the model predictions for $\mathrm{Re}(n_{\mathrm{eff}})$ already seen in Figs. 5-5(a), the model is found to be highly accurate despite its simplicity.

5.4 Analysis of the main model limitation

As shown in previous Sections, the microscopic model is an accurate tool to analyze light transport and to disclose the origin of negative index of fishnet metamaterials. It also offers guidelines to engineer the spectrum of negative index and the energy dissipation in fishnets. Since it is based on some assumptions detailed in Chapter 4, the microscopic model is of course an approximation of the light transport in the fishnet mesh. Hereafter we discuss in more detail the main model limitations.

The propagations constants and the elementary scattering coefficients at the heart of our modeling are calculated for two plasmonic waveguides (the Metal-Insulator-Metal slab waveguide and the chain of metallic rectangular holes) with infinitely thick metallic cladding (see Section 4.5 for the relevant technical details). However, in realistic fishnets the metallic layer between two dielectric layers is of finite thickness; it is only slightly larger than (or even comparable with) the skin depth in noble metals: the thickness of the metallic layer $2h_{\mathrm{m}}$ is several tens of nanometers. For typical fishnet metamaterials, the separation in the x-direction between two neighbouring hole chains (several hundreds of nanometers) is much larger than the field penetration of the TE_{01} mode in the metal. Thus the coupling between Metal-Insulator-Metal (MIM) channels is more critical and is examined in details hereafter.

In the seminal experimental work in [Val08], the metallic layer thickness is only $2h_{\mathrm{m}} = 30$ nm, which is comparable with the skin depth. In this case, the MIM transversal channels become vertically coupled and cannot be considered as being

strictly independent. For this type of tightly cascaded fishnet structures, the microscopic model predictions become less accurate, as shown in Fig. 5-7.

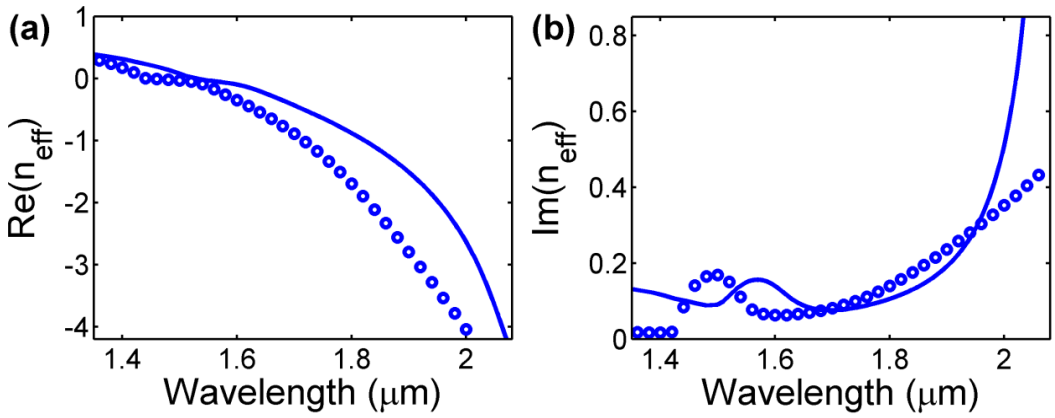

Figure 5-7. Real (**a**) and imaginary part (**b**) of the fishnet effective index for $2h_m = 30$ nm. The model predictions and the fully-vectorial calculations are shown as solid curves and circles respectively.

Clearly, the discrepancy between the model predictions and the rigorous calculations is much severer than for all the results shown in previous Sections obtained for a metallic thickness of $2h_m = 100$ nm. However, although the agreement is less quantitative, the model can still capture the main features of the fundamental Bloch mode: the negative index occurs at wavelengths larger than 1.5 μm, the damping $\mathrm{Im}(n_{eff})$ of the mode increases rapidly at long wavelengths. It can be seen that both the real and imaginary parts of n_{eff} predicted by the model are red-shifted with respect to fully-vectorial calculations. This red-shift can be understood as a result of the coupling between the gap-SPPs in different dielectric layers, as sketched in Figs. 5-8(a) and (b).

Due to the coupling of the adjacent MIM channels, less field concentrates in the metallic components and the real and imaginary parts of the gap-SPP propagation constant n_{sp} both decrease with respect to a single MIM waveguide with an infinite metallic cladding. We calculate n_{sp} for a periodic MIM stack as the function of the metallic layer thickness $2h_m$ at $\lambda = 1.8$ μm, see Fig. 5-8(c). For $2h_m = 30$ nm [Val08], the gap-SPP normalized propagation constant is $n_{sp} = 1.72 + 0.004i$, whereas for a single MIM waveguide, we have $n_{sp} = 1.98 + 0.028i$ (value used in the model). Clearly, the fact that the model predictions are less quantitative for small metallic thicknesses can be ascribed to the large difference between n_{sp} [especially $\mathrm{Re}(n_{sp})$] of a single MIM waveguide and that of a periodic MIM stack. We can conclude that

optically "thick" metallic layers that provides a good isolation between different dielectric layers allow for a more accurate modelling.

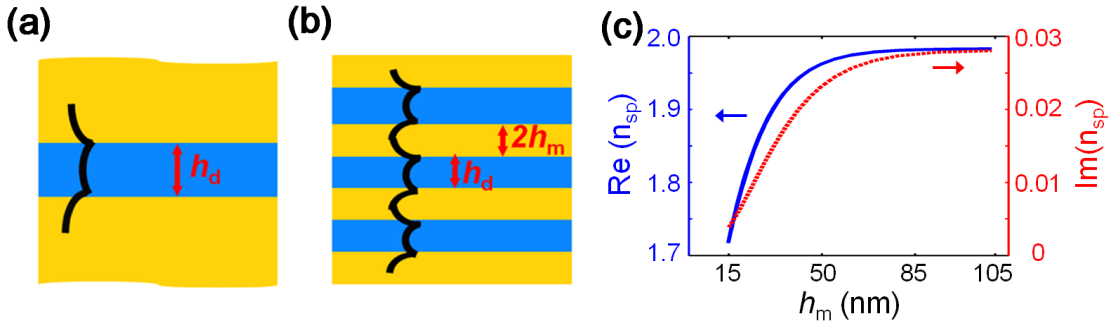

Figure 5-8. Single (**a**) and coupled (**b**) Metal-Insulator-Metal (MIM) waveguide(s). The single MIM waveguide has infinitely thick metallic cladding ($h_m = \infty$), and the periodic stack of MIM waveguides possesses finite metallic thickness h_m. (**c**) Normalized propagation constant n_{sp} of the gap-SPP supported by a periodic MIM stack at $\lambda = 1.8$ μm. In (c), the solid blue and dashed red curves represent Re(n_{sp}) and Im(n_{sp}), respectively. In the MIM stack, the field tunnels through the metallic layers and couple with nearby dielectric layers, resulting in a coupled gap-SPP supermode with a smaller propagation constant. This coupled mode is not considered in the model, resulting in the red shift observed in Fig. 5-7.

Finally, we have checked that, when Re(n_{sp}) is decreased intentionally to match the value of the gap-SPP supermode of a periodic MIM stack, the model predictions for Re(n_{eff}) of fishnets with small metallic thickness $2h_m = 30$ nm become more accurate (not shown here). Nevertheless, the discrepancy at long wavelengths ($\lambda > 1.8$ μm) is still substantial, which indicates that the model can only partially captures the light transport in the long wavelength band. In fact, because of the tiny thickness of the metal films (30 nm) in this fishnet structure, the vertical transport could be also partially mediated by higher order modes of the metallic holes, which are neglected in the model.

5.5 Conclusion

In this Chapter, we have taken advantage of the analyticity of the microscopic model to analyze the impact of various geometrical and material parameters on the negative index of fishnet metamaterials. In particular, the model provides guidelines

for engineering the position of the negative-index band. We have also shown that, unfortunately, parameter optimisation only leads to small improvements of the high loss level. It therefore seems that the large absorption losses from which the performance of optical metamaterials suffer can only be significantly reduced by incorporating some gain in the structure. The resulting light amplification allows for a compensation of the absorption over some spectral range where the effective index can stay negative.

We have shown that the microscopic model is a powerful tool to analyze fishnet metamaterials that incorporate gain media. Indeed, only a few calculations need to be performed with amplification; most of the required calculations (in particular those of the scattering coefficients of the plasmonic modes) can be done with a passive structure. This clearly allows for a lightened modeling of the intricate problem of light amplification inside a complex three-dimensional structure. We have evidenced that the introduction of gain in the dielectric layers mainly affects the imaginary part of the fishnet effective index, leaving the real part unchanged. However, at the transparency threshold, the transversal gap-SPP resonance becomes delocalized over a few tens of unit cells and fishnets with gain should not be considered as 3D metamaterials, but rather as 1D layered system. We finally emphasize that the theoretical semi-analytical approach relying on tracking the local transport of electromagnetic fields can be very helpful for designing and modeling complex plasmonic nanostructures for various applications, not only negative-index metamaterials.

Chapter 6

Ultra-small 3D Metal-Insulator-Metal (MIM) resonators: slow retardation effects in the quasi-static limit

Magnetic resonances are at the heart of metamaterial design. At visible and near-infrared frequencies, such resonances have been demonstrated in metallo-dielectric nanostructures, such as split-ring resonators [Liu08a, Ser09] and nanorod (or cut-wire) pairs [Sha05, Dol05]. The latter consists of alternating metal and dielectric layers with finite dimensions and we will refer to these structures with the generic term Metal-Insulator-Metal (MIM) resonator. As discussed in Chapter 4, MIM geometries also play a crucial role in the negative refractive index of fishnet metamaterials. The objective of this chapter is to understand in details the optical properties of a single three-dimensional (3D) MIM resonator with ultra-small dimensions. We study the quality factor variation of MIM nanoresonators when their volume is shrunk from the diffraction limit $(\lambda/2n)^3$ down to a deep subwavelength scale $(\lambda/50)^3$. In addition to rigorous fully-vectorial calculations, we provide a comprehensive study of the cavity mode and a semi-analytical expression of the quality factor Q obtained with a Fabry-Perot model. The latter quantitatively predicts the absorption and radiation losses of the nanoresonator and provides an in-depth understanding of the mode lifetime that cannot be obtained with brute-force computations. In particular, it highlights the impact of slow-wave effects on the Q-factor as the size of the resonator is decreased. The Fabry-Perot model also evidences that, unexpectedly wave retardation effects are present in metallic nanoparticles, even for deep subwavelength dimensions in the quasi-static regime.

6.1 Introduction

Optical nanoresonators with ultra-small volumes are a key ingredient for numerous nanophotonics applications. They are the building blocks (the so-called meta-atoms) of metamaterials [Sha07, Sou11], high performance sensors [Ank08, Liu11, Cat11], photovoltaic cells [Atw10], solid-state non-classical light sources [Mak10, Cho11] or nanolasers [Nez10]. Confining light in three-dimensional (3D) volumes well below the diffraction limit can be achieved by taking advantage of the large wavevectors of surface plasmon polaritons (SPPs) that result from the coupling between light and free electrons in metals [Rae88]. Among numerous types of plasmonic resonators, Metal-Insulator-Metal (MIM) structures, i.e., alternating metal and dielectric layers with finite dimensions, show promising performance. In addition to ultra-small confinement volumes and high field enhancements [Miy06, Lev06, Kut10], MIM resonators (also known as cut-wire pairs in the metamaterials community [Dol05]) can support a magnetic resonance that is involved in the appearance of artificial magnetism at optical frequencies [Dol05, Sha05, Zha05, Mar08, Yan11]. Consequently, arrays of MIM resonators have been studied for achieving either a negative effective index [Dol05, Sha05] or an efficient absorption for sensor or photodetector applications [Cat11, Lin08, Per09, Liu10a, Hao10, Wu11, Koe11].

In view of potential applications of MIM resonators in a variety of areas ranging from metamaterials to photovoltaics, it is important to obtain a deep understanding of their optical properties, in particular when their size is scaled down to deep subwavelength dimensions. Indeed, ultra-small resonators are of major importance both for metamaterials, where meta-atoms should be much smaller than the wavelength, and for photodetector applications, where several resonators can be associated within a subwavelength cell to engineer multi-resonant structures [Koe11]. The tunability of the resonance wavelength of MIM resonators with the resonator dimensions being well-known [Miy06, Lev06, Kur07, Boz07, Jun07], we will mainly focus on the analysis of the quality factor (Q-factor) variation as the resonator size is scaled down.

We study the resonance with the lowest energy supported by a single 3D MIM resonator, see Fig.6-1. This fundamental resonance is crucial in the context of ultra-small resonators because it has no cut-off and can be scaled down to deep subwavelength dimensions in the quasi-static regime. Moreover, this resonance

presents a "magnetic" character and can be used to engineer negative-index metamaterials [Dol05, Sha05, Gar06, Roc11]. We especially quantify the variation of the Q-factor when the resonator volume is shrunk from the diffraction limit $V = (\lambda/2n)^3$ down to a deep subwavelength scale $V = (\lambda/50)^3$. As shown by 3D fully-vectorial calculations, the main trend is a significant increase of the Q-factor by one order of magnitude when the size is reduced. To explain this increase, we use an approximate Fabry-Perot model, which allows us to derive semi-analytical expressions of the quality factor, of the absorption and of the radiation losses. The model thus provides a real understanding of the physics governing the mode lifetime at deep subwavelength scales. In particular, it evidences the crucial role played by the slowness of the SPP modes that are bouncing back and forth inside the resonator, a physical effect that is completely hidden in brute-force computations. Over the past ten years, Fabry-Perot models have been successfully applied to a variety of micro- and nanoresonators, including photonic-crystal microcavities and micropilars [Sau05, Lal08], and plasmonic nanowire resonators with a longitudinal length of a few wavelengths [Dit05, Nov07, Bar08, Dor09, Tam11]. Hereafter we evidence that such a useful picture remains valid and helpful even for analyzing nanoresonators that are operating far below the diffraction limit in the quasi-static regime.

We note that in the present context a Fabry-Perot model has already been used for studying two-dimensional (2D) MIM resonators [Boz07]. However, the authors in [Boz07] do not consider any slow-wave effect and consequently some of their conclusions are erroneous. For instance, their Q-factor expression is not consistent with the asymptotic value derived in the quasi-static limit for metallic nanoparticles of arbitrary shape [Wan06]. We correct this discrepancy by correctly taking into account slow-wave effects in the Fabry-Perot model. Indeed, as we show in sections 6.3 and 6.4, a correct Fabry-Perot expression for the Q-factor is highly accurate and fully consistent with other asymptotic expressions derived in the quasi-static limit [Wan06]. In Section 6.3 we highlight three different regimes for the Q-factor variation with the resonator size. As the volume shrinks from the diffraction limit $V = (\lambda/2n)^3$ to $V = (\lambda/20)^3$, the Q-factor first increases because of a reduction of the radiation losses. Then, from $V = (\lambda/20)^3$ to $V = (\lambda/35)^3$, the radiation losses reduction is balanced by an increase of the absorption and one would intuitively expect a drop of the Q-factor as predicted in [Boz07]. However, the Q-factor keeps on increasing because of the slowdown of the SPP mode that bounces back and forth inside the resonator. This slow-wave effect, which is similar to the one classically encountered in photonic crystal microcavities [Sau05, Lal08], results in an increase of the cavity-mode lifetime. Finally, for ultrasmall resonators, the Fabry-Perot model correctly

predicts the quality factor saturation toward the asymptotic value obtained in the quasi-static limit [Wan06].

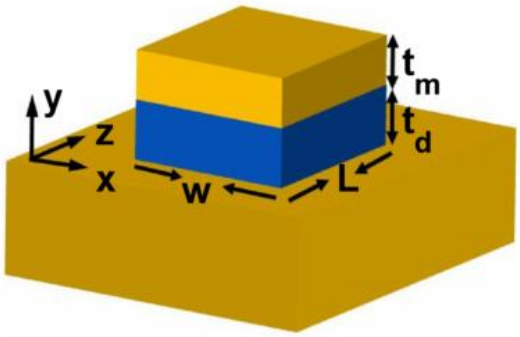

Figure 6-1. Geometry of the 3D MIM resonantor. The nanoresonator consists of a dielectric rectangular nanoparticle (width w, length L and thickness t_d) sandwiched between a metal substrate and a metal layer of thickness t_m. The metal is silver and the dielectric material is a semiconductor (such as GaAs) with a high refractive index of 3.5 in the spectral range of interest (around λ=950nm).

6.2 Magnetic resonance of a single 3D MIM resonator

The 3D MIM resonator under study consists of a dielectric rectangular nanoparticle (width w, length L and thickness t_d) sandwiched between a metal substrate and a metal layer with the same width and length and with a thickness denoted by t_m, see Fig. 6-1. Calculations have been performed for silver, whose permittivity has been taken from the data tabulated in [Joh72]. In order to maximize the confinement and the Q-factor, the dielectric material has been chosen to be a semiconductor with a high refractive index (GaAs, n = 3.5). Since it has only a weak impact on the resonator properties as long as it remains larger than the skin depth, the thickness t_m of the top metallic layer is fixed in the following and we take t_m = 25 nm. All rigorous fully-vectorial calculations are performed with a 3D frequency-domain fully-vectorial modal method known as the aperiodic Fourier Modal Method (a-FMM) [Sil01]. Stretching of the numerical space through coordinate transforms is additionally incorporated for improving the computational accuracy, see the method MM3 in the benchmark article [Bes07] for more details.

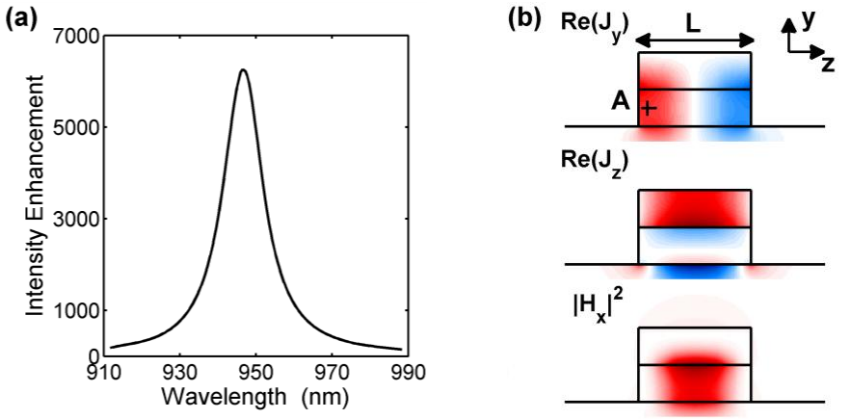

Figure 6-2. Magnetic resonance of a single MIM nanoresonator. (**a**) Spectrum of the intensity enhancement $|E|^2/|E_{inc}|^2$ at the point A in (**b**) for a resonator (w = 40 nm, t_d = 20 nm and L = 70 nm) illuminated by a plane wave impinging from air at normal incidence and polarized along the z-direction. (**b**) Distribution of the induced current **J** (see the text for its definition) and of the magnetic field $|H_x|^2$ at resonance in the (y, z) plane (x = 0). Blue and red colors correspond to negative and positive values. The induced current is localized under the resonator and forms a loop in the (y, z) plane.

Figure 6-2(a) presents the spectrum of the electric field enhancement inside the MIM resonator (dimensions are provided in the figure caption) when the latter is illuminated from air by a plane wave at normal incidence and polarized along the z-direction. Figure 6-2(b) shows the distribution of the magnetic field $|H_x|^2$ and of the electric current density $\mathbf{J}(\boldsymbol{r})$ induced in the nanoresonator by the incident plane wave at resonance, λ = 947 nm. From the curl Maxwell equations, the induced current is proportional to the total electric field $\mathbf{E}(\boldsymbol{r})$,

$$\mathbf{J}(\boldsymbol{r}) = -i\omega\,[\varepsilon(\boldsymbol{r}) - \varepsilon_{ref}(\boldsymbol{r})]\,\mathbf{E}(\boldsymbol{r}), \qquad (6\text{-}1)$$

with ω the frequency, ε_0 the vacuum permittivity, $\varepsilon(\boldsymbol{r})$ the relative permittivity distribution defining the resonator and $\varepsilon_{ref}(\boldsymbol{r})$ the relative permittivity of a reference background. For a nanoresonator in a uniform background, the natural choice for $\varepsilon_{ref}(\boldsymbol{r})$ is the homogeneous relative permittivity of the background. In the present case, the natural choice would be to choose the air/metal interface as the reference background. Then the induced current would be interpreted as an equivalent current source localized near the interface, which radiates a field that is similar to the field scattered by the actual resonator illuminated by the plane wave. Doing that, the induced current would be restricted to a volume defined by the dielectric and metallic rectangular nanoparticles. The inconvenience of this choice is that the

induced current in the metal substrate just below the resonator is not highlighted. Consequently, we chose a uniform background $\varepsilon_{ref}(\boldsymbol{r}) = 1$. As can be seen from Fig. 6-2(b), at the resonance wavelength, the electric current density $\mathbf{J}(\boldsymbol{r})$ induced by the incident plane wave essentially forms a loop in the (y, z) plane, $\mathrm{Re}(J_x) << \mathrm{Re}(J_y)$ and $\mathrm{Re}(J_x) << \mathrm{Re}(J_z)$, and the resonant magnetic field is perpendicular to the loop. This evidences the magnetic character of the fundamental MIM resonance, as previously discussed in the literature [Dol05, Sha05, Gar06, Roc11].

In the following, we thoroughly study the quality factor Q of this magnetic resonance. Note that, throughout the chapter, the resonance wavelength $\lambda_0 = 950$ nm is maintained constant. In order to fulfill this condition as the two transverse resonator dimensions (the width w and the dielectric thickness t_d) are varied, one simply adjusts the length L of the MIM particle. The quality factor can be directly derived from the full-width-at-half-maximum of a Lorentzian fit of the intensity enhancement spectrum shown in Fig. 6-2(a). However, in order to get more physical insight, we analyze the MIM resonator as a Fabry-Perot cavity (Fig. 6-3).

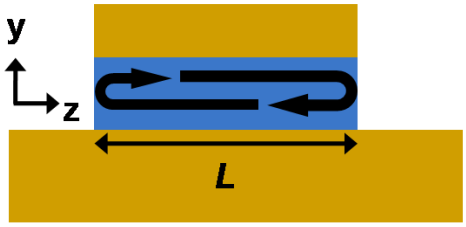

Figure 6-3. Fabry-Perot picture of the MIM resonator. The energy inside the resonator is assumed to be carried only by the fundamental plasmonic mode of the MIM waveguide. Under this assumption, the resonance is created by the bouncing of the mode between the resonator facets.

6.3 Fabry-Perot model of the magnetic resonance

Within the Fabry-Perot picture (Fig. 6-3), the resonance is described as a standing wave pattern along the z-direction created by the bouncing between the nanoparticle facets at $z = -L/2$ and $z = L/2$ of a single mode, the fundamental plasmonic mode of the MIM waveguide, whose cross-section in the (x, y) plane is represented in Fig. 6-4. The single mode approximation amounts to assume that all higher-order modes of the MIM waveguide play a negligible role to build the resonance. The validity of the assumption is discussed in more details in the following; as will be shown, it depends mostly on the transversal size of the MIM

waveguide. The key parameters of the Fabry-Perot model are thus the propagation constant $\beta = k_0 n_{eff} + i\alpha/2$ of the fundamental plasmonic mode supported by the MIM waveguide and its complex reflection coefficient $r = \sqrt{R}\exp(i\phi_r)$ at the facet.

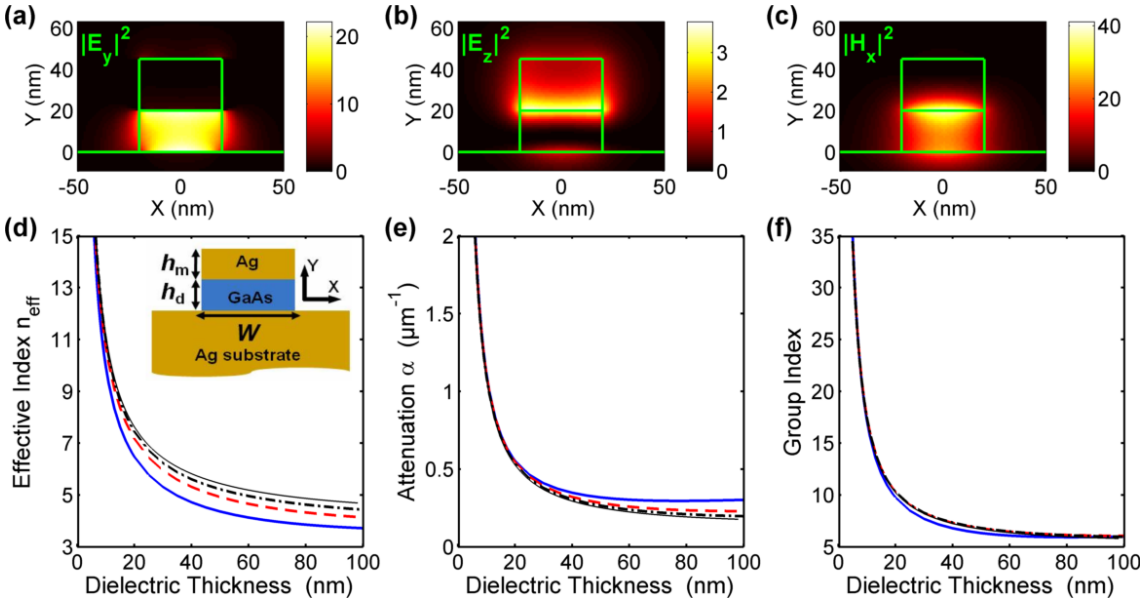

Figure 6-4. Fundamental plasmonic mode of the MIM waveguide for $\lambda = 950$ nm. (**a**)-(**c**) Main field components $|E_y|^2$, $|E_z|^2$ and $|H_x|^2$ of the mode for $w = 40$ nm and $t_d = 20$ nm. (**d**) Dependence on the dielectric thickness t_d of the effective index $n_{eff} = \mathrm{Re}(\beta)/k_0$, (**e**) of the attenuation $\alpha = 2\mathrm{Im}(\beta)$ and (**f**) of the group index $n_g = n_{eff} - \lambda \partial n_{eff}/\partial\lambda$. In (**d**)-(**f**), four different widths are considered, $w = 40$ nm (solid blue), 100 nm (dashed red), 350 nm (dashed-dotted black) and ∞ (planar waveguide, thin solid line).

We first calculate and discuss these two important physical quantities in Section 6.3.1. Then we provide in Section 6.3.2 closed-form expressions for the resonance length L and the quality factor Q. These formulae are validated against fully-vectorial calculations and the gained physical understanding for the Q-factor variation with the resonator volume is discussed in Section 6.3.3.

6.3.1 *Fabry-Perot model parameters: fundamental mode of the MIM waveguide and facet reflectivity*

The three main field components of the fundamental mode of the MIM waveguide, $|E_y|^2$, $|E_z|^2$ and $|H_x|^2$, are shown in Figs. 6-4(a)-(c) for $w = 40$ nm and $t_d = 20$ nm. For $w \to \infty$ (planar MIM stack) and $t_m \to \infty$, this mode results from the coupling with a symmetric magnetic field H_x of two metal/insulator SPPs [Eco69]. The H_x-symmetric

mode of a planar MIM stack has no cut-off as the insulator thickness decreases, unlike the antisymmetric mode that is cut-off at roughly $\lambda_0/(2n)$. Therefore, for the thicknesses of interest, $t_d < 100$ nm, the planar MIM stack is monomode. Reducing the top metal thickness to $t_m = 25$ nm does not change the nature of the fundamental mode, except that the symmetry is slightly broken, see Figs. 6-4(a)-(c). As the dielectric thickness t_d decreases, the symmetric mode of the MIM stack interacts more strongly with the metal and presents a rapid increase of both its effective index $n_{eff} = \mathrm{Re}(\beta)/k_0$ and its attenuation $\alpha = 2\mathrm{Im}(\beta)$, as shown by the thin-solid curves in Figs. 6-4(d)-(e).

The fundamental mode of the MIM waveguide with a finite width follows a similar trend. As can be seen from Figs. 6-4(d)-(e), the impact of the width w on the propagation constant is much weaker than the impact of the thickness t_d; the propagation constant of the 2D waveguide is almost equal to that of the planar stack, especially for small thickness. Let us emphasize that the mode group index $n_g = c/v_g$, with v_g the group velocity, also increases as the dielectric thickness is reduced, see Fig. 6-4(f). As will be shown hereafter, the slowdown of the plasmonic mode supported by thin MIM waveguides directly impacts the resonator lifetime. Finally, it is noteworthy that for finite widths higher-order modes with the same symmetry along y as the fundamental plasmonic mode may exist. They are determined by a total-internal-reflection condition at the air/dielectric interfaces and possess an increasing number of nodes along x, see the insets in Fig. 6-5(c).

The large increase of the effective index is a key ingredient to build ultra-small resonators since the resonator length L corresponding to the fundamental resonance is of the order of $\lambda_0/(2n_{eff})$. However, the price to pay for a reduction of the resonator volume is an enhanced dissipation in the metal. In order to accurately quantify the impact on the quality factor of the absorption increase, we need to thoroughly evaluate the variation of the radiation losses with the size. In the Fabry-Perot picture, the normalized power dissipated by radiation per round-trip is simply equal to $1 - R$, with R the reflectivity of the fundamental mode at the MIM facets.

We have performed fully-vectorial calculations of the modal reflection coefficient $r = \sqrt{R}\exp(i\phi_r)$ as a function of w and t_d with the a-FMM. The results are presented in Fig. 6-5(a). The reflectivity strongly increases as the waveguide cross-section is reduced because of the increased mode confinement. For $w = t_d = 100$ nm, the facets only weakly reflect the fundamental plasmonic mode, $R = 0.7$, whereas for $w = 40$ nm and $t_d = 10$ nm R is as large as 0.999. Figure 6-5(b) shows the dependence of the reflectivity with the thickness t_d for $w = 40$, 100, 350 nm and ∞. The four

curves show the same main trend, namely a significant enhancement of R as t_d is reduced. The width dependence is highlighted in Fig. 6-5(c) for t_d = 20, 35 and 50 nm. It is important to note the non-monotonous variation of the reflectivity. The narrow dips correspond to a strong backscattering into higher-order MIM waveguide modes that are cut-off at the dip wavelength. The insets in Fig. 6-5(c) show the profile of the first two x-symmetric higher-order modes (because of symmetry reasons, anti-symmetric higher-order modes do not impact the reflectivity of the symmetric fundamental mode). When a higher-order mode passes its cut-off and becomes propagative, the total density of states is modified by the appearance of a new mode (often with a small group velocity) and this causes a sharp dip in the modal reflectivity of the fundamental mode. The dip is especially pronounced for the appearance of the first higher-order mode. Finally, it is noteworthy that even extremely tiny waveguides with transverse dimensions as small as w < 100 nm and t_d < 10 nm are not monomode. This unexpected observation can be intuitively understood from the large value of the effective index n_{eff}^{1D} of planar MIM stacks (w infinite) with a small dielectric thickness t_d; the cut-off width of higher-order modes is indeed linked to the value of $\lambda_0/(2n_{eff}^{1D})$, which becomes smaller and smaller as t_d is decreased.

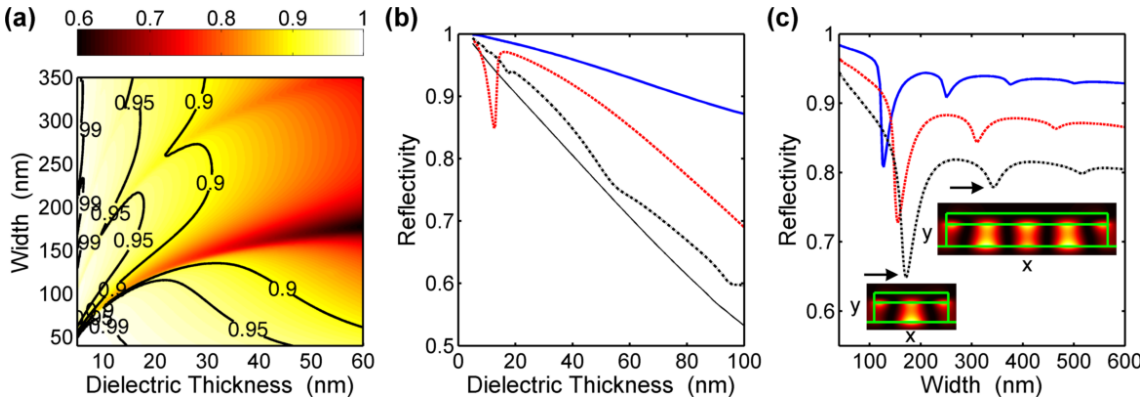

Figure 6-5. Reflectivity at the MIM facet for λ = 950 nm. (**a**) Map of the reflectivity as a function of the width w and the dielectric thickness t_d. (**b**) Reflectivity as a function of t_d for w = 40 nm (solid blue), 100 nm (dashed red), 350 nm (dashed-dotted black) and ∞ (planar waveguide, thin solid line). (**c**) Reflectivity as a function of w for t_d = 20 nm (solid blue), 35 nm (dashed red) and 50 nm (dashed-dotted black). The insets show the distribution of $|H_x|^2$ in the (x, y) plane for the first two symmetric higher-order waveguide modes for t_d = 50 nm. The first two drops in the reflectivity curves identified by arrows correspond to the cut-off of these modes (w = 190 nm and w = 370 nm).

6.3.2 *Fabry-Perot equations: phase-matching condition and quality factor*

Since we have fixed the resonance wavelength to $\lambda_0 = 950$ nm, the length L of the resonator is easily obtained from the phase-matching condition

$$L = \frac{\lambda_0}{2n_{\text{eff}}}\left(m - \frac{\phi_r}{\pi}\right), \tag{6-2}$$

with $m = 1, 2, \ldots$, n_{eff} the effective index of the waveguide mode given in Fig. 6-4(d) and ϕ_r the phase of the modal reflection coefficient at the MIM facet. Here we do not consider the unusual Fabry-Perot resonance with $m = 0$ that may exist in subwavelength metallic structures [Fei08]. For this situation to occur, the positive propagation phase has to be fully compensated by a negative reflection phase. Such a resonance does not exist in the MIM resonators under study since $\phi_r \approx 0$. We are interested hereafter in the fundamental resonance $m = 1$. The reflection phase varies between $\phi_r = \pi/8$ for the largest waveguide cross-section ($w = 350$ nm and $t_d = 100$ nm) and $\phi_r = -\pi/20$ for the smallest cross-section ($w = 40$ nm and $t_d = 5$ nm) and therefore, with a good approximation, one may consider that Eq. (6-2) leads to $L = \lambda_0/(2n_{\text{eff}})$, corresponding to the classical half-wavelength condition for the resonator length. Figure 6-6(a) shows the resonator length obtained from Eq. (6-2) as a function of the dielectric thickness t_d for $w = 40$, 100 and 350 nm. Because of the strong increase of n_{eff}, L rapidly decreases as t_d decreases. On the other hand, the resonator width w is found to weakly impact the length.

Within the Fabry-Perot picture, and under the assumption of a narrow resonance, the quality factor Q can be derived analytically as [Lal08]

$$Q = \frac{k_0 n_g L_{\text{eff}}}{1 - R_{\text{eff}}}, \tag{6-3}$$

with $k_0 = 2\pi/\lambda_0$, $n_g = n_{\text{eff}} - \lambda\frac{\partial n_{\text{eff}}}{\partial\lambda}$ the group index of the MIM waveguide mode, $R_{\text{eff}} = R\exp(-\alpha L)$ the effective reflectivity of the facet that includes the absorption loss over one-half round-trip, and $L_{\text{eff}} = L + 2L_p$ the effective resonator length that includes the facet penetration length $L_p = -\frac{\lambda^2}{4\pi n_g}\frac{\partial\phi_r}{\partial\lambda}$. The penetration length represents less than 10% of the effective length L_{eff}. For instance, for large

waveguide cross-sections (w = 100 nm and t_d = 100 nm) $L_p \approx 5\text{nm} << L \approx 100$ nm and for small cross-sections (w = 40 nm and t_d < 25 nm) $L_p < 1\text{ nm} << L \approx 30$ nm. Thus L_p can be safely neglected for all values of w and t_d considered in the present work.

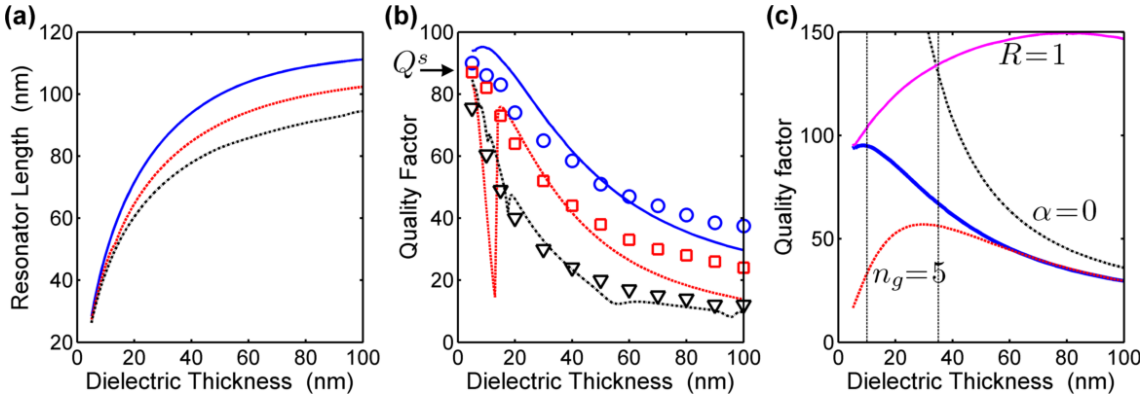

Figure 6-6. Fabry-Perot model predictions for the resonance at λ_0 = 950 nm for w = 40 nm (solid blue), 100 nm (dashed red) and 350 nm (dashed-dotted black). (**a**) Length of the nanoresonator predicted with Eq. (6-2). (**b**) The solid curves show the quality factors predicted with the Fabry-Perot model given by Eq. (6-3), $Q = k_0 n_g L_{eff}/[1 - R\exp(-\alpha L)]$. The markers represent the Q-factor values extracted from fully-vectorial a-FMM calculations of intensity enhancement spectrums [see Fig. 6-2(a)] for the same widths, w = 40 nm (blue circles), 100 nm (red squares) and 350 nm (black triangles). The horizontal arrow shows the quasi-static Q-factor Q^s given by Eq. (6-4). (**c**) Quality factor predicted with the Fabry-Perot model for w = 40 nm (thick solid blue). The Q-factors predicted without radiation [R = 1 in Eq. (6-3), solid magenta], without absorption [α = 0 in Eq. (6-3), dashed-dotted black] and without slow light effect [n_g = 5 in Eq. (6-3), dashed red] are also presented. The vertical dashed lines mark the different regimes of the Q-factor variation.

The predictions of Eq. (6-3) are shown in Fig. 6-6(b) for w = 40, 100 and 350 nm together with fully-vectorial calculations of the Q-factor, extracted from Lorentzian fits of the intensity enhancement spectra and shown with various markers. The analytical formula of Eq. (6-3) accurately predicts the Q-factor increase. When the resonator volume is shrunk from roughly the diffraction limit $V \approx (\lambda/2n)^3$ (w = 120 nm, t_d = 100 nm and L = 100 nm) down to a deep subwavelength scale $V = (\lambda/50)^3$ (w = 40 nm, t_d = 5 nm and L = 30 nm), the Q factor is significantly enhanced by one order of magnitude.

Strictly speaking, the Fabry-Perot model should be applied only when all higher-order modes are evanescent. For instance, for w = 100 nm, the MIM is monomode only for t_d > 15 nm, and for w = 350 nm, the MIM is multimode whatever

the value of t_d. Hopefully, the presence of higher-order modes does not alter the model predictions, except close to their cut-off where a drop of Q is inaccurately predicted in Fig. 6-6(b) because of the rapid change of the facet reflectivity. Note that the deviation between the model predictions and rigorous calculations vanishes as the waveguide width increases.

6.3.3 *Analysis of the Q factor increase*

Because of its analytical treatment, the model allows us to provide a comprehensive analysis of the Q-factor limitations. As shown by Eq. (6-3), the cavity-mode lifetime is impacted both by absorption (α in R_{eff}) and radiation ($1-R$). In order to separate the contributions of these two loss channels and to clarify the impact of the SPP slowdown, Fig. 6-6(c) shows the Q-factor predicted by Eq. (6-3) for $w = 40$ nm (thick solid blue curve) together with the Q-factor values that would have been achieved for $\alpha = 0$, $R = 1$ and $n_g = 5$. Taking $\alpha = 0$ in Eq. (6-3) amounts to remove the absorption; the black dashed-dotted curve thus gives an approximation of the radiation-limited Q. Then, considering the particle facets as perfect reflectors, $R = 1$ in Eq. (6-3), amounts to neglect the radiation losses and gives an approximation of the absorption-limited Q. Consistently with the fact that the absorption and the scattering of small particles respectively scale as the particle volume and as the particle volume squared [Boh83], we find that the Q-factor of large MIM resonators with $V \approx (\lambda/2n)^3$ is mostly limited by radiation, $Q \approx Q_{\alpha = 0}$, whereas the Q-factor of small resonators in the quasi-static limit with $V \approx (\lambda/50)^3$ is completely limited by absorption, $Q \approx Q_{R = 1}$. Radiation and absorption losses are balanced for $t_d = 35$ nm. Finally, the impact on the resonance lifetime of the slowdown of the MIM waveguide mode is unraveled by considering Eq. (6-3) with a constant group index $n_g = 5$, a value corresponding to thick MIM waveguides with $t_d = 100$ nm (red dashed curve).

Three different regimes of Q-factor variation can be considered. They are marked by vertical dashed lines in Fig. 6-6(c). The first regime concerns large resonator thicknesses, $t_d > 35$ nm. The absorption L and the group index n_g are roughly constant and the increase of the quality factor is purely due to a reduction of the radiation losses (increase of the reflectivity R). In the second regime, $10 < t_d < 35$ nm, the Q-factor increases (solid thick blue curve) due to the slowdown of the SPP mode bouncing inside the resonator. Indeed, it is noticeable that a resonator with the actual absorption and radiation but with a constant group index (red dashed curve) would see its Q-factor decreasing because the radiation-loss reduction is balanced by an increase of the absorption. Finally, for extremely thin

dielectric layers, $t_d < 10$ nm, we enter the quasi-static regime where the resonator performance is purely limited by absorption. The validity of the Fabry-Perot model in this last regime is discussed in the next Section.

6.4 Fabry-Perot model in the quasi-static limit

In the quasi-static limit, i.e., for dimensions much smaller than the wavelength, the quality factor Q^s of any metallo-dielectric resonant nanoparticle composed of a single lossy metal is completely determined from the relative permittivity of the metal $\varepsilon_m = \varepsilon_m' + i\varepsilon_m''$ [Wan06],

$$Q^s = \frac{\omega_0 \frac{\partial \varepsilon_m'}{\partial \omega}}{2\varepsilon_m''}. \qquad (6\text{-}4)$$

In this limit, the specific structure of the particle is not important and the Q-factor depends neither on the geometric shape nor on the dielectric media, provided that the latter are dispersionless and lossless. This universal result has been derived in [Wan06] by assuming a nanoparticle built in a noble metal ($|\varepsilon_m'| >> \varepsilon_m''$) that supports a purely electrostatic resonance ($\nabla \times \mathbf{E} = 0$) whose damping is solely due to absorption (no radiation losses). This last assumption can be justified by the fact that the scattering of small particles scales as the particle volume squared whereas the absorption scales only as the particle volume [Boh83].

The quasi-static regime is usually associated to the absence of wave retardation effects because $k_0 L << 1$ for small size-to-wavelength ratios. On the other hand, the Fabry-Perot model describes a resonance as the result of a round-trip retardation accumulation of $2m\pi$, $m = 1, 2, \ldots$ Thus, at first sight, the Fabry-Perot picture seems inappropriate to describe a resonance in the quasi-static limit. This intuitive conclusion is in contradiction with Fig. 6-6(b) that evidences the accuracy of the Fabry-Perot predictions even for ultrasmall resonators with $V \approx (\lambda/50)^3$. In order to clarify whether a nanoparticle can be described by a non-vanishing wave retardation in the quasi-static limit, we now analytically study the asymptotic behavior of Fabry-Perot models as resonator sizes tend toward zero. We emphasize that retardation effects are present in very small objects and that MIM nanoparticles, even in the quasi-static limit, are equivalent to half-wavelength antennas. This

equivalence has been recently discussed for the resonance wavelength [Has11], and hereafter, we additionally evidence that it applies also quantitatively to the quality factor of the resonance. In particular, we show that the closed-form expression of the Q-factor given by Eq. (6-3) reduces to Eq. (6-4) in the quasi-static limit.

We consider a Fabry-Perot resonance with a Q-factor given by Eq. (6-3). As in [Wan06], we assume that the resonance damping in the quasi-static limit is purely due to absorption. This amounts to consider $R = 1$ in Eq. (6-3), an assumption legitimated for the geometry under study by the numerical results of Fig. 6-6(c). Moreover, the resonator length is small and the absorption term in the Q-factor can be approximated by $\exp(-\alpha L) \sim 1 - \alpha L$. With these two approximations, Eq. (6-3) leads to

$$Q = k_0 n_g / \alpha. \tag{6-5}$$

To obtain this result, we have considered that $L_p << L$ and $L_{eff} \approx L$. Equation (6-5) emphasizes that, in the absence of radiation losses, the Q-factor is purely driven by the guided SPP mode bouncing back and forth inside the particle. This important parameter is the group-index-to-attenuation ratio, and not only the attenuation as concluded in [Boz07].

Next we examine the asymptotic value of the propagation constant of MIM waveguides as their transverse dimensions become much smaller than the wavelength. We note from Fig. 6-4 that the normalized propagation constant of the fundamental mode of 2D MIM waveguides with finite widths w becomes independent of the width as $t_d/\lambda \to 0$ and asymptotically tends toward the effective index n_{eff}^{1D} of planar MIM stacks. This is easily understood by realizing that for any fixed value of the width w, we can have $w >> \lambda/(2n_{eff}^{1D})$ as t_d is reduced. Actually, the limit of n_{eff}^{1D} as $t_d/\lambda \to 0$ is known analytically [Boz07]

$$n_{eff}^{1D} \to -\varepsilon_d \lambda_0 / (\pi \varepsilon_m t_d), \tag{6-6}$$

with ε_d the relative permittivity of the dielectric layer. Thus Eq. (6-6) can be safely used to derive the limit of the n_g/α ratio for any 2D MIM waveguide. The expressions of $n_g = n_{eff}^{1D} - \lambda \partial n_{eff}^{1D}/\partial\lambda$ and $\alpha = 2k_0 \mathrm{Im}(n_{eff}^{1D})$ are easily derived from Eq. (6-6), and by inserting them into Eq. (6-5), the asymptotic value Q^{s}_{FP} of the Fabry-Perot Q-factor in the quasi-static limit is found to be given by

$$Q^{s}_{FP} = \frac{\omega_0 \frac{\partial \varepsilon_m'}{\partial \omega}}{2\varepsilon_m''}, \tag{6-7}$$

which is exactly the Q^s value of Eq. (6-4) derived in [Wan06]. Note that to derive Eq. (6-7), we assumed that $|\varepsilon_m'| >> \varepsilon_m''$. The prediction of Eq. (6-7) is represented by the horizontal arrow in Fig. 6-6(b). It is noteworthy that the 3D MIM nanoparticle under study enters the quasi-static regime only for very small dielectric thicknesses, $t_d < 10$ nm.

The derivation of Eq. (6-7) leads to two important conclusions. First, it evidences that the Fabry-Perot resonator model can be appropriately used to describe a resonance in the quasi-static limit. In other words, the quasi-static regime does include wave retardation effects linked to the propagation *inside* the particle of plasmonic modes whose wavevector diverges as the length shrinks (actually the product $k_0 n_{eff} L = \pi$ is fixed by the Fabry-Perot phase-matching condition). The second important conclusion concerns the properties of plasmonic waveguides in the quasi-static limit. Indeed, the Q-factor expressions of Eqs. (6-4) and (6-5) should be identical as the transverse cross-section shrinks, whatever the cross-section of the plasmonic waveguide. We can therefore deduce that, in the limit of small transverse dimensions compared to the wavelength, the propagation constant of any plasmonic waveguide should satisfy

$$k_0 \left(\frac{n_g}{\alpha} \right)^S = \frac{\omega_0 \frac{\partial \varepsilon_m'}{\partial \omega}}{2\varepsilon_m''}, \tag{6-8}$$

regardless of the geometric shape of the waveguide cross-section or of the dielectric media composing it, provided that they are dispersionless and lossless.

6.5 Conclusion

In summary, we have studied the quality factor of the fundamental resonance supported by MIM nanoresonators when their volume is shrunk from the diffraction limit $V = (\lambda/2n)^3$ down to a deep subwavelength scale $V = (\lambda/50)^3$. The ten-fold increase of the Q-factor given by rigorous fully-vectorial calculations has been accurately predicted with a Fabry-Perot model of the resonance, which provides

analytical expressions of the quality factor, of the absorption and of the radiation losses. These expressions allow for a comprehensive analysis of the increase of the mode lifetime as the dimensions of the resonator are shrunk. The main reasons are a reduction of the radiation losses and a slowdown of the plasmonic mode bouncing back and forth inside the resonator. The slow-wave effect is responsible for the Q-factor increase even when the radiation-loss decrease is fully balanced by an increase of the absorption.

A second important result of this work is to show that the Fabry-Perot model remains quantitatively valid down to very small dimensions far below the diffraction limit. This evidences that the localized plasmon resonances of MIM nanoparticles in the quasi-static limit can be quantitatively analyzed with the same wave retardation effects as the delocalized resonance of nanowires with a length of a few wavelengths. The nanoparticle is indeed an half-wavelength antenna but with a vanishing effective wavelength $\lambda_0/(2n_{\text{eff}})$ [Nov07].

We hope that the Fabry-Perot analytical treatment of the magnetic resonance supported by MIM nanoparticles will be helpful for further “bottom-up” approaches for the design of optical metamaterials starting from the optical properties of single meta-atoms.

Chapter 7

Conclusion and Perspectives

7.1 Summary

In this thesis, we mainly focused on theoretical investigations of optical fishnet metamaterials, which are a prominent type of negative-index metamaterials at visible and near-infrared frequencies. Throughout the work, we tried to establish theories relying on semi-analytical methods. Thanks to simple and well-controlled approximations, it is indeed possible to develop accurate models that provide more physical insight than brute-force simulations of Maxwell's equations. The thesis is summarized as follows.

In *Chapter 2*, we have shown that the knowledge of the problem of light scattering at a *single* air/metamaterial interface allows for an in-depth test of the homogenization validity. Moreover, we have proposed an innovative approach for retrieving the effective optical parameters (ε_{eff} and μ_{eff}). This new retrieval procedure emphasizes the central role played by the fundamental Bloch mode supported by the metamaterial and it provides results that are more accurate or stable than those obtained by the widely-used S-parameter method [Smi02].

In *Chapter 3*, we have derived simple and accurate closed-form expressions for the scattering at an interface between two different periodic media. These expressions, which apply to weak periodicity differences, are based on Bloch mode orthogonality and allow one to calculate the scattering when only the fundamental Bloch modes of the two media are known. The high accuracy of those expressions has been verified by thoroughly testing for two different geometries, dielectric periodic waveguides and optical fishnet metamaterials.

In *Chapters 4 and 5*, we have successfully derived an accurate semi-analytical model for light propagation in optical fishnet metamaterials. Instead of looking at the energy transport from a macroscopic point of view, as is the case in homogenization procedures, we track light as it propagates inside the fishnet mesh, as fluid flows in a multi-channel system. This microscopic model promotes a description of light propagation that is based on a flow in a complex network, rather than on a flow in a homogenized material. The model reveals that the negative index mainly originates from a magnetic-type SPP resonance, and that this resonance can be tuned spectrally by geometric or material tailoring. As a result, the spectrum of negative index can be shifted. Importantly too, the microscopic model shines new light on how the

inevitable Ohmic losses of the fishnet can be compensated by incorporation of gain in the dielectric layers. We have explicitly shown that gain mainly affects the imaginary part of the fishnet effective index, leaving the negative-valued real part unchanged. However, at the transparency threshold, the magnetic resonance becomes delocalized over a few tens of transversal periods, and fishnets with gain should not be considered as 3D metamaterials but rather as 1D thin film stacks.

In *Chapter 6*, we have studied the quality factor Q of the fundamental resonance of Metal-Insulator-Metal (MIM) nanoresonators with an accurate semi-analytical Fabry-Perot model. The model, in which the distinct contributions of radiation loss, absorption and slow plasmonic waves, have been carefully taken into account, allows for a comprehensive analysis of the increase of the Q factor as the resonator volume is shrunk from the diffraction limit to the *quasi-static limit* (size $\sim \lambda/50$). We have found that surprisingly the Fabry-Perot description remains quantitatively valid even in the quasi-static regime. This observation indicates that both strongly localized resonances in plasmonic nanoparticles and delocalized resonance in elongated plasmonic nanowires may be possibly understood under the same conceptual umbrella, a wave-retardation based antenna problem.

An important conclusion is that the main optical properties of a fishnet metamaterial arise from the fishnet fundamental Bloch mode, and we have thoroughly studied the *propagation* and the *scattering* of the Bloch mode at an air/metamaterial interface. We have adopted two different points of view in our studies. On the one hand, we have looked at the metamaterial macroscopically and analyzed under which conditions it can be homogenized, starting from the knowledge of the fundamental Bloch mode and its scattering coefficient at an interface. On the other hand, we have looked “inside” the Bloch mode with an approximate semi-analytical model. The latter allowed us to literally build the mode from its elementary constituents, namely plasmonic modes that propagates and scatters in the fishnet circuitry. Since this approach obviously handle physical processes at a scale smaller than the metamaterial period, we have used the term microscopic model.

Although optical fishnet metamaterials exhibit extraordinary properties such as a broad-band negative refractive index with rather low losses compared to other types of optical metamaterials, they possess strong spectral dispersion as presented in this thesis and strong spatial dispersion [Roc08]. Because of these unwanted

properties, fishnet metamaterials still lie far away from some applications such as high-resolution imaging. The inevitable energy dissipation in metals at optical frequencies further hinders true applications.

7.2 Possible extensions of the work

Altogether, I hope that this work, and more particularly the methods and formalisms that were developed, could open up some interesting trails for future studies. I discuss hereafter some possible extensions of the work performed during this thesis, in the metamaterials domain and in the more general context of nanophotonics.

The expressions of the scattering coefficients at an interface separating two different periodic media derived in Chapter 3 could be applied to design graded periodic structures. They could also provide a powerful tool to calculate light scattering by a small imperfection in a periodic waveguide, a key problem to analyze light propagation in disordered periodic structures [Maz09].

The semi-analytical microscopic model developed in Chapter 4 could easily be generalized for analyzing/designing aperiodic structure. Indeed, studying a periodic structure such as a fishnet metamaterial constitutes only one particular case for the use of the model. Moreover, the philosophy of the microscopic model, i.e., analyzing complex metallo-dielectric nanostructures by tracking the local transport of electromagnetic waves in the system, could be applied (perhaps with a weaker analyticity) to other metamaterials based on localized resonators, such as paired nanorods [Sha07], split rings [Rod09] or metallic pillar arrays [Ver10, Yao08]. It should also be highlighted that, the microscopic formalism can possibly serve as a robust tool for studying light localization at low dimensions [Rüt03].

Finally, the Fabry-Perot model used to describe the magnetic resonance of Metal-Insulator-Metal nanoparticles in Chapter 6 could be used to derive closed-form expressions for the multipole moments associated to the resonance, in particular the electric and magnetic dipole moments. These expressions could be a starting point for a semi-analytical derivation of the effective optical parameters ε_{eff} and μ_{eff} of a metamaterial composed of MIM resonators [Roc11].

Bibliography

[Ank08] J. Anker, W. Hall, O. Lyandres, N. Shah, J. Zhao, R. van Duyne, ''Biosensing with plasmonic nanosensors'', Nature Mater. **7**, 442-453 (2008).

[Atw10] H. Atwater and A. Polman, ''Plasmonic for improved photovoltaic devices'', Nature Mater. **9**, 205-213 (2010).

[Bab08] T. Baba, ''Slow light in photonic crystals'', Nature Photon. **2**, 465 (2008).

[Bar08] E. Barnard, J. White, A Chandran and M. Brongersma, ''Spectral properties of plasmonic resonator antennas'', Opt. Express **16**, 16529-16537 (2008).

[Bel03] P. Belov, R. Marques, S. Maslovski, I. Nefedov, M. Silveirinha, C. Simovski and S. Tretyakov, ''Strong spatial dispersion in wire media in the very large wavelength limit'', Phys. Rev. B **67**, 113103 (2003).

[Bes07] M. Besbes, J.P. Hugonin, P. Lalanne, S. van Haver, O. Janssen, A. Nugrowati, M. Xu, S. Pereira, H. Urbach, A. van de Nes , P. Bienstman, G. Granet, A. Moreau, S. Helfert, M. Sukharev, T. Seideman, F. Baida, B. Guizal, D. van Labeke, ''Numerical analysis of a slit-groove diffraction problem'', J. Europ. Opt. Soc. Rap. Public. **2**, 07022 (2007).

[Bis04] R. Biswas, Z. Li and K. Ho, ''Impedance of photonic crystals and photonic crystal waveguides'', Appl. Phys. Lett. **84**, 1254-1256 (2004).

[Boc10] P. Bock, P. Cheben, J. Schmid, J. Lapointe, A. Delâge, S. Janz, G. Aers, D. Xu, A. Densmore and T. Hall, ''Subwavelength grating crossings for silicon wire waveguides'', Opt. Express **18**, 16146-16155 (2010).

[Boh83] C. Bohren and D.R. Huffman, Absorption and Scattering of Light by Small Particles. (Wiley, New York, 1983).

[Boz07] S. Bozhevolnyi and T. Søndergaard, ''General properties of slow-plasmon resonant nanostructures: nano-antennas and resonators'', Opt. Express **15**, 10869-10877 (2007).

[Bri02] S. O'Brien and J. Pendry, ''Magnetic activity at infrared frequencies in structured metallic photonic crystals'', J. Phys. Condens. Matter **14**, 6383 (2002).

[Bri04] S. O'Brien, D. McPeake, S. Ramakrishna and J. Pendry, ''Near-infrared photonic band gaps and nonlinear effects in negative magnetic metamaterials'', Phys. Rev. B **69**, R241101 (2004).

[Bur10] S. Burgos, R. de Waele, A. Polman and H. Atwater, "A single-layer wide-angle negative-index metamaterials at visible frequencies", Nature Mater. **9**, 407-412 (2010).

[Cak09] A. Cakmak, E. Colak, H. Caglayan, H. Kurtand E. Ozbay, ''High efficiency of graded index photonic crystal as an input coupler'', J. Appl. Phys. **105**, 103708 (2009).

[Cao02] Q. Cao, P. Lalanne and J. Hugonin, "Stable and efficient Bloch-mode computational method for one-dimensional grating waveguides," J. Opt. Soc. Am. A **19**, 335-338 (2002).

[Cat11] A. Cattoni, P. Ghenuche, A. Haghiri-Gosnet, D. Decanini, J. Chen, J. Pelouard and S. Collin, ''λ3/1000 plasmonic nanocavities for biosensing fabricated by soft UV nanoimprint lithography'', Nano Lett. **11**, 3557-3563 (2011).

[Cen05] E. Centeno and D. Cassagne, ''Graded photonic crystals'', Opt. Lett. **30**, 2278 (2005).

[Cha11] D. Chanda, K. Shigeta, S. Gupta, T. Cain, A. Carlson, A. Mihi, A. Baca, G. Bogart, P. Braun and J. Rogers, ''Large-area flexible 3D optical negative index metamaterial formed by nanotransfer printing'', Nat. Nano. **6**, 402-407 (2011).

[Che94] W. Chew and W. Weedon, ''A 3D perfectly matched medium from modified maxwell's equations with stretched coordinates'', Microw. Opt. Techn. Lett. **7**, 599 (1994).

[Cho11] J.T. Choy, B. Hausmann, T. Babinec, I. Bulu, M. Khan, P. Maletinsky, A. Yacoby and M. Loncar, ''Enhanced single-photon emission from a diamond-silver aperture'', Nature Photon. **5**, 738-743 (2011).

[Dit05] H. Ditlbacher, A. Hohenau, D. Wagner, U. Kreibig, M. Rogers, F. Hofer, F. Aussenegg and J. Krenn, ''Silver nanowires as surface plasmon resonators'', Phys. Rev. Lett. **95**, 257403 (2005).

[Dol05] G. Dolling, C. Enkrich, M. Wegener, J. Zhou, C. Soukoulis and S. Linden, ''Cut-wire pairs and plate pairs as magnetic atoms for optical metamaterials'', Opt. Lett. **30**, 3198-3200 (2005).

[Dol07] G. Dolling, M. Wegener and S. Linden, ''Realization of a three-functional-layer negative-index photonic metamaterial'', Opt. Lett. **32**, 551–553 (2007).

[Dor09] J. Dorfmüller, R. Vogelgesang, R. Weitz, C. Rockstuhl, C. Etrich, T. Pertsch, F. Lederer and K. Kern, ''Fabry-Perot resonances in one-dimensional plasmonic nanostructures'', Nano Lett. **9**, 2372-2377 (2009).

[Dos06] K. Dossou, M. Byrne and L. Botten, ''Finite element computation of grating scattering matrices and application to photonic crystal band calculations'', J.

Comput. Phys. **219**, 120-143 (2006).

[Eco69] E. Economou, ''Surface plasmons in thin films'', Phys. Rev. **182**, 539-554 (1969).

[Eme97] D. Emerson, ''The works of Jagadis Chandra Bose: 100 years of mm-wave research'', IEEE Trans. on Microwave Theory and Tech. **45**, 2267 (1997).

[Fal10] A. Fallahi and C. Hafner, ''Analysis of semi-infinite periodic structures using a domain reduction technique'', J. Opt. Soc. Am. A **27**, 40-49 (2010).

[Fan06] N. Fang, D. Xi, J. Xu, M. Ambati, W. Srituravanich, C. Sun and X. Zhang, ''Ultrasonic metamaterials with negative modulus'', Nature Mater. **5**, 452 - 456 (2006).

[Fan09] A. Fang, Th. Koschny, M. Wegener and C. Soukoulis, ''Self-consistent calculation of metamaterials with gain'', Phys. Rev. B **79**, 241104(R) (2009).

[Fan10] A. Fang, Th. Koschny and C. Soukoulis, ''Self-consistent calculation of loss-compensated fishnet metamaterials'', Phys. Rev. B **82**, 121102(R) (2010).

[Fei08] E. Feigenbaum and M. Orenstein, ''Ultrasmall volume plasmons, yet with complete retardation effects'', Phys. Rev. Lett. **101**, 163902 (2008).

[Fru23] J. Fruanhofer, ''Kurtzer Bericht von den Resultaten neuerer Versuche ber die Sesetze des lichtes, und die Theorie erselbem'', Annalen Der Physik **74**, 337 (1823).

[Gar02] N. Garcia, and M. Nieto-Vesperinas, ''Is there an experimental verification of a negative index of refraction yet ?'', Opt. Lett. **27**, 885-887 (2002).

[Gar06] F. Garwe, C. Rockstuhl, C. Etrich, U. Hübner, U. Bauerschäfer, F. Setzpfandt, M. Augustin, T. Pertsch, A. Tünnermann and F. Lederer, ''Evaluation of gold nanowire pairs as a potential negative index material'', Appl. Phys. B **84**, 139-148 (2006).

[Gar07] F. García de Abajo, ''Light scattering by particle and hole arrays'', Rev. Mod. Phys. **79**, 1267 (2007).

[Gar09] C. García-Meca, R. Ortuño, F.J. Rodríguez-Fortuño, J. Martí and A. Martínez, ''Negative refractive index metamaterials aided by extraordinary optical transmission'', Opt. Express **17**, 6026-6031 (2009).

[Gar11] C. García-Meca, J. Hurtado, J. Martí, A. Martínez, W. Dickson and A. Zayats, ''Low-Loss multilayered metamaterial exhibiting a negative index of refraction at visible wavelengths'', Phys. Rev. Lett. **106**, 067402 (2011).

[Gen07] C. Genet and T.W. Ebbesen, ''Light in tiny holes'', Nature (London) **445**, 39 (2007).

[Gil61] H. Gilbert, *Miniaturization*, (Reinhold, New York, 1961).

[Gor05] R. Gordon and A. Brolo, ''Increased cut-off wavelength for a subwavelength hole in a real metal'', Opt. Express **13**, 1933-1938 (2005).

[Gre03] R. Greegor, C. Parazzoli, K. Li, B. Koltenbah and M. Tanielian, ''Experimental determination and numerical simulation of the properties of negative index of refraction materials'', Opt. Express **11**, 688-695 (2003).

[Hao10] J. Hao, J. Wang, X. Liu, W.J. Padilla, L. Zhou and M. Qiu, ''High performance optical absorber based on a plasmonic metamaterial'', Appl. Phys. Lett. **96**, 251104 (2010).

[Has11] S. Hasan, R. Filter, A. Ahmed, R. Vogelgesang, R. Gordon, C. Rockstuhl and F. Lederer, ''Relating localized nanoparticle resonances to an associated antenna problem'', Phys. Rev. B **84**, 195405 (2011).

[Hen07] J. Henzie, M. H. Lee, and T.W. Odom, ''Multiscale patterning of plasmonic metamaterials'', Nature Nano. **2**, 549 (2007).

[Hug05a] J. Hugonin and P. Lalanne, Reticolo software for grating analysis, Institut d'Optique, Palaiseau, France (2005).

[Hug05b] J. Hugonin and P. Lalanne, ''Perfectly matched layers as nonlinear coordinate transforms: a generalized formalization'', J. Opt. Soc. Am. A **22**, 1844-1849 (2005).

[Ham11] J. Hamm, S. Wuestner, K. Tsakmakidis and O. Hess, ''Theory of light amplification in active fishnet metamaterials'', Phys. Rev. Lett. **107**, 167405 (2011)

[Ish05] A. Ishikawa, T. Tanaka and S. Kawata, ''Negative magnetic permeability in the visible light region'', Phys. Rev. Lett. **95**, 237401 (2005).

[Jac98] J. Jackson, Classical Electrodynamics, 3rd edition. (John Wiley & Sons, New Yok, 1998)

[Jep11] C. Jeppesen, S. Xiao, N. Mortensen and A. Kristensen, ''Extended verification of scaling behavior in split-ring resonators'', Opt. Commun. **284**, 799–801 (2011)

[Joa08] John D. Joannopoulos, Steven G. Johnson, Joshua N. Winn and Robert D. Meade, Photonic Crystals: Molding the Flow of Light, 2nd edition. (Princeton University Press, 2008)

[Joh72] P. Johnson and R. Christy, ''Optical constants of the noble metals'', Phys. Rev. B **6**, 4370 (1972).

[Joh87] S. John, ''Strong localization of photons in certain disordered dielectric superlattices'', Phys. Rev. Lett. **58**, 2486 (1987).

[Jun07] J. Jung, T. Søndergaard and S. Bozhevolnyi, ''Gap plasmon-polariton nanoresonators: scattering enhancement and launching of surface plasmon

polaritons'', Phys. Rev. B **79**, 035401 (2007).

[Kad12] M. Kadic, T. Bückmann, N. Stenger, M. Thiel and M. Wegener, ''On the practicability of pentamode mechanical metamaterials'', Appl. Phys. Lett. **100**, 191901 (2012)

[Kao11] T. Kao, S. Jenkins, J. Ruostekoski and N. Zheludev, ''Coherent control of nanoscale light localization in metamaterial: creating and positioning isolated subwavelength energy hot spots'', Phys. Rev. Lett. **106**, 085501 (2011).

[Kat05] N. Katsarakis, G. Konstantinidis, A. Kostopoulos, R. Penciu, T. Gundogdu, M. Kafesaki, E. Economou, Th. Koschny and C. Soukoulis, ''Magnetic response of split-ring resonators in the far-infrared frequency regime'', Opt. Lett. **30**, 1348 (2005).

[Kit05] C. Kittel, Introduction to Solid State Physics, 8th Edition. (John Wiley & Sons, New Yok, 2005)

[Kle06] M. Klein, C. Enkrich, M. Wegener, C. Soukoulis and S. Linden, ''Single-slit split-ring resonators at optical frequencies: limits of size scaling'', Opt. Lett. **31**, 1259-1261 (2006)

[Koe11] C. Koechlin, P. Bouchon, F. Pardo, J. Jaeck, X. Lafosse, J. Pelouard and R. Haidar, ''Total routing and absorption of photons in dual color plasmonic antennas'', Appl. Phys. Lett. **99**, 241104 (2011).

[Kos05] Th. Koschny, P. Markoš, E. Economou, D. Smith, D. Vier and C. Soukoulis, ''Impact of inherent periodic structure on effective medium description of left-handed and related metamaterials'', Phys. Rev. B **71**, 245105 (2005).

[Kra96] T. Krauss, R. DeLaRue and S. Brand, ''Two-dimensional photonic-bandgap structures operating at near-infrared wavelengths'', Nature **383**, 699 (1996).

[Kur07] H. Kurt and D. Citrin, ''Graded index photonic crystals'', Opt. Express **15**, 1240-1253 (2007).

[Kur07] Y. Kurokawa and H. Miyazaki, ''Metal-insulator-metal plasmon nanocavities: analysis of optical properties'', Phys. Rev. B.**75**, 035411 (2007).

[Kut10] M. Kuttge, F. Garcia de Abajo and A. Polman, ''Ultrasmall mode volume plasmonic nanodisk resonators'' Nano Lett. **10**, 1537-1541 (2010).

[Lal98] P. Lalanne, S. Astilean, P. Chavel, E. Cambril and H. Launois, ''Blazed binary subwavelength gratings with efficiencies larger than those of conventional échelette gratings'', Opt. Lett. **23**, 1081-1083 (1998).

[Lal02] P. Lalanne and A. Talneau, ''Modal conversion with artificial materials for photonic-crystal waveguides'', Opt. Express **10**, 354-359 (2002).

[Lal05] P. Lalanne, J. Hugonin and J. Rodier, ''Theory of surface plasmon generation at nanoslit aperture'', Phys.Rev. Lett. **95**, 263902 (2005)

[Lal08] P. Lalanne, C. Sauvan and J. Hugonin, ''Photon confinement in photonic crystal nanocavities'', Laser & Photon. Rev. **2**, 514-526 (2008).

[Lal09] P. Lalanne, J. Hugonin, H. Liu and B. Wang, ''A microscopic view of the electromagnetic properties of sub-λ metallic surfaces'', Sur. Sci. Rep. **64**, 453-469, (2009).

[Lan60] L. D. Landau and E. M. Lifshitz, Electrodynamics of Continuous Media. (Pergamon, Oxford, 1960)

[Lec07] G. Lecamp, J. Hugonin and P. Lalanne, ''Theoretical and computational concepts for periodic optical waveguides'', Opt. Express **15**, 11042-60 (2007).

[Leo06] U. Leonhardt, ''Optical Conformal Mapping'', Science **312**, 1777 (2006).

[Leo07] U. Leonhardt. ''Optical metamaterials: invisibility cup'', Nature Photon. **1**, 207-208 (2007).

[Lev06] G. Leveque and O. Martin, ''Tunable composite nanoparticle for plasmonics'', Opt. Lett. **31**, 2750-2752 (2006).

[Li97] L. Li, ''New formulation of the Fourier modal method for crossed surface-relief gratings'', J.Opt. Soc. Am. A **14**, 2758-2767 (1997).

[Lin05] G. Dolling, C. Enkrich, M. Wegener, J. F. Zhou, C. Soukoulis and S. Linden, ''Cut-wire pairs and plate pairs as magnetic atoms for optical metamaterials'', Opt. Lett. **30**, 3198-3200 (2005).

[Lin06] S. Linden, C. Enkrich, G. Dolling, M. Klein, J. Zhou, Th. Koschny, C. Soukoulis, S. Burger, F. Schmidt and M. Wegener, ''Photonic metamaterials: magnetism at optical frequencies'', IEEE J. Sel. Top. Quant. Electron. **12**, 1097-1105 (2006)

[Lin08] L. Lindquist, W. Luhman, S. Oh and R. Holmes, ''Plasmonic nanocavity arrays for enhanced efficiency in organic photovoltaic cells'', Appl. Phys. Lett. **93**, 123308 (2008).

[Liu08a] N. Liu, H. Guo, L. Fu, S. Kaiser, H. Schweizer and H. Giessen, ''Three-dimensional photonic metamaterials at optical frequencies'', Nature Mater. **7**, 31–37 (2008).

[Liu08b] H. Liu and P. Lalanne, ''Microscopic theory of the extraordinary optical transmission'', Nature **452**, 728-731 (2008).

[Liu10a] N. Liu, M. Mesch, T. Weiss, M. Hentschel and H. Giessen, ''Infrared perfect absorber and its application as plasmonic sensor'', Nano Lett. **10**, 2342-2348 (2010).

[Liu10b] H. Liu, ''Symmetry in the elementary scattering of surface plasmon polaritons and a generalized symmetry principle'', Opt. Lett. **35**, 2876 (2010).

[Liu11] N. Liu, M. Tang, M. Hentschel, H. Giessen, A. Alivisatos, ''Nanoantenna-enhanced gas sensing in a single tailored nanofocus'', Nature Mater. **10**, 631-636 (2011).

[Mak10] I. Maksymov, M. Besbes, J. Hugonin, J. Yang, A. Beveratos, I. Sagnes, I. Robert-Philip and P. Lalanne, ''Metal-coated nanocylinder cavity for broadband nonclassical light emission'', Phys. Rev. Lett. **105**, 180502 (2010).

[Mar08a] R. Marqués, F. Martín and M. Sorolla, Metamaterials with negative parameters: theory, design and microwave applications. (Wiley, New Jersey, 2008)

[Mar08b] A. Mary, S. Rodrigo, F. Garcia-Vidal and L. Martin-Moreno, ''Theory of negative-refractive-index response of double-fishnet structures'', Phys. Rev. Lett. **101**, 103902 (2008).

[Mar09] R. Marqués, L. Jelinek, F. Mesa and F. Medina, ''Analytical theory of wave propagation through stacked fishnet metamaterials'', Opt. Express **17**, 11582-11593 (2009).

[Max73] J. Maxwell, A treatise on electricity and magnetism, (Clarendon Press, Oxford, 1873).

[Maz09] S. Mazoyer, J. Hugonin and P. Lalanne, ''Disorder-induced multiple scattering in photonic-crystal waveguides'', Phys. Rev. Lett. **103**, 063903 (2009).

[Med08] F. Medina, F. Mesa and R. Marques, IEEE Trans. Microwave Theory Tech. **56**, 3108 (2008);

[Mei99] M. Meier, A. Mekis, A. Dodabalapur, A. Timko and R. Slusher, ''Laser action from two-dimensional distributed feedback in photonic crystals'', Appl. Phys. Lett. **74**, 7 (1999).

[Men10] C. Menzel, T. Paul, C. Rockstuhl, T. Pertsch, S. Tretyakov and F. Lederer, ''Validity of effective material parameters for optical fishnet metamaterials'', Phys. Rev. B **81** 035320 (2010).

[Mer09] R. Merlin, ''Metamaterials and the Landau–Lifshitz permeability argument: Large permittivity begets high-frequency magnetism'', Proc. Natl. Acad. Sci. **106**, 1693-1698 (2009).

[Miy06] H. Miyazaki and Y. Kurokawa, ''Squeezing visible light waves into a 3-nm-thick and 55-nm-long plasmon cavity'', Phys. Rev. Lett. **96**, 097401 (2006).

[Mom07] B. Momeni, A. Eftekhar and A. Adibi, ''Effective impedance model for analysis of reflection at the interfaces of photonic crystals'', Opt. Lett. **32**, 778-780 (2007).

[Nez10] M. Nezhad, A. Simic, O. Bondarenko, B. Slutsky, A. Mizrahi, L. Feng, V. Lomakin and Y. Fainman, ''Room-temperature subwavelength metallo-dielectric lasers'', Nature Photon. **4**, 395-399 (2010).

[Nov07] L. Novotny, ''Effective wavelength scaling for optical antennas'', Phys. Rev. Lett. **98**, 266802 (2007).

[Pal85] E. Palik, Handbook of optical constants of solids. (Academic Press, New York, 1985)

[Pal01] M. Palamaru and P. Lalanne, ''Photonic crystal waveguides: out-of-plane losses and adiabatic modal conversion'', Appl. Phys. Lett. **78**, 1466-69 (2001).

[Pap03] A. Papakostas, A. Potts, D. M. Bagnall, S. L. Prosvirnin, H. J. Coles and N. I. Zheludev, ''Optical manifestations of planar chirality'', Phys. Rev. Lett.**90**, 107404 (2003).

[Par03] C. Parazzoli, R. Greegor, K. Li, B. Koltenbah and M. Tanielian, ''Experimental verification and simulation of negative index of refraction using Snell's law'', Phys. Rev. Lett. **90**, 107401 (2003).

[Pau10] T. Paul, C. Menzel, C. Rockstuhl and F. Lederer, ''Advanced optical metamaterials'', Adv. Mater., **22**, 2354–2357 (2010).

[Pen96] J. Pendry, A. Holden, W. Stewart and I. Youngs, ''Extremely low frequency plasmons in metallic mesostructures'', Phys. Rev. Lett. **76**, 4773-4776 (1996).

[Pen98] J. Pendry, A. Holden, D. Robbins and W. Stewart, ''Low frequency plasmons in thin-wire structures'', J. Phys. Condens. Matter **10**, 4785 (1998)

[Pen99] J. Pendry, A. Holden, D. Robbins and W. Stewart, ''Magnetism from conductors and enhanced nonlinear phenomena'', IEEE Transactions on Microwave Theory and Tech. **47**, 2075 (1999).

[Pen00] J. Pendry, ''Negative refraction makes a perfect lens'', Phys. Rev. Lett. **85**, 3966- 3969 (2000).

[Pen03] J. Pendry, ''Optics: Positively negative'', Nature **423**, 22-23 (2003).

[Pen06] J. Pendry, D. Schurig and D. Smith, ''Controlling electromagnetic fields'', Science **312**, 1780–1782(2006).

[Pen10] R. S. Penciu, M. Kafesaki, Th. Koschny, E. Economou and C. Soukoulis, ''Magnetic response of nanoscale left-handed metamaterials'', Phys. Rev. B **81**, 235111 (2010).

[Per09] J. Le Perchec, Y. Desieres and R. Espiau de Lamaestre, ''Plasmon-based photosensors comprising a very thin semiconducting region'', Appl. Phys. Lett. **94**, 181104 (2009).

[Pet08] J. Petschulat, C. Menzel, A. Chipouline, C. Rockstuhl, A. Tünnermann, F. Lederer and T. Pertsch, ''Multipole approach to metamaterials'', Phys. Rev. A **78**, 043811 (2008).

[Pod03] V. Podolskiy, A. Sarychev and V. Shalaev, ''Plasmon modes and negative refraction in metal nanowire composites'', Opt. Express. **11**, 735 (2003).

[Pok02] A. Pokrovsky, and A. Efros, ''Electrodynamics of metallic photonic crystals and the problem of left-handed materials'', Phys. Rev. Lett. **89**, 093901 (2002).

[Pok04] A. Pokrovsky, ''Analytical and numerical studies of wire-mesh metallic photonic crystals'', Phys. Rev. B **69**, 195108 (2004).

[Rae88] H. Raether, Surface plasmons on smooth and rough surfaces and on gratings. (Springer, Berlin, 1988)

[Ram05] S. Ramakrishna, ''Physics of negative refractive index materials'', Rep. Prog. Phys. **68**, 449-521 (2005).

[Roc08] C. Rockstuhl, C. Menzel, T. Paul, T. Pertsch and F. Lederer, ''Light propagation in a fishnet metamaterial'', Phys. Rev. B **78**, 155102 (2008).

[Roc11] C. Rockstuhl, C. Menzel, S. Mühlig, J. Petschulat, C. Helgert, C. Etrich, A. Chipouline, T. Pertsch and F. Lederer, ''Scattering properties of meta-atoms'', Phys. Rev. B **83**, 245119 (2011).

[Rod09] F. Rodríguez-Fortuño, C. García-Meca, R. Ortuño, J. Martí and A. Martínez, ''Modeling high-order plasmon resonances of a U-shaped nanowire used to build a negative-index metamaterial'', Phys. Rev. B **79**, 075103 (2009).

[Rus03] P. Russel, ''Photonic crystal fibers'', Science **299**, 358 (2003).

[Rüt03] F. Rüting, P. Huidobro and F. García-Vidal, ''Emergence of Anderson localization in plasmonic waveguides'', Opt. Lett. **36**, 4341 (2011).

[Sau05] C. Sauvan, P. Lalanne and J.P. Hugonin, ''Slow-wave effect and mode-profile matching in photonic crystal microcavities'', Phys. Rev. B **71**, 165118 (2005).

[Sch06] D. Schurig, J. Mock, B. Justice, S. Cummer, J. Pendry, A. Starr and D. Smith, ''Metamaterial electromagnetic cloak at microwave frequencies'', Science **314**, 977-980 (2006).

[See05] D. Seetharamdoo, R. Sauleau, K. Mahdjoubi and A. Tarot, ''Effective parameters of resonant negative refractive index metamaterials: interpretation and validity'', J. Appl. Phys. **98**, 063505 (2005).

[Ser09] I. Sersic, M. Frimmer, E. Verhagen and A. Koenderink, ''Electric and magnetic dipole coupling in near-infrared split-ring metamaterial arrays'', Phys. Rev. Lett. **103**, 213902 (2009)

[Sha05] V. Shalaev, W. Cai, U. Chettiar, H. Yuan, A. Sarychev, V. Drachev and A. Kildishev, ''Negative index of refraction in optical metamaterials'', Opt. Lett. **30**, 3356-3358 (2005).

[Sha07] V. Shalaev, ''Optical negative-index metamterials'', Nature Photon. **1**, 41 (2007).

[She01] R. Shelby, D. Smith and S. Schultz, ''Experimental verification of a negative index of refraction'', Science **292**, 77 (2001).

[Sie96] D. Sievenpiper, M. Sickmiller and E. Yablonovitch, ''3D wire mesh photonic crystals'', Phys. Rev. Lett. **76**, 2480-2483 (1996).

[Sil01] E. Silberstein, P. Lalanne, J. Hugonin and Q. Cao, ''Use of grating theories in integrated optics'', J. Opt. Soc. Am. A **18**, 2865-2875 (2001).

[Smi99] D. Smith, D. Vier, W. Padilla, S. Nemat-Nasser and S. Schultz, ''Loop-wire medium for investigating plasmons at microwave frequencies'', Appl. Phys. Lett. **75**, 1425 (1999)

[Smi00] D. Smith, W. Padilla, D. Vier, S. Nemat-Nasser and S. Schultz, ''Composite medium with simultaneously negative permeability and permittivity'', Phys. Rev. Lett., **84**, 4184 (2000).

[Smi02] D. Smith, S. Schultz, P. Markoš, and C. Soukoulis, ''Determination of effective permittivity and permeability of metamaterials from reflection and transmission coefficients'', Phys. Rev. B **65**, 195104 (2002).

[Smi06] D. Smith and J. Pendry, ''Homogenization of metamaterials by field averaging'', J. Opt. Soc. Am. B **23**, 391 (2006).

[Śmi08] W. Śmigaj and B. Gralak, ''Validity of the effective-medium approximation of photonic crystals'', Phys. Rev. B **77**, 235445 (2008).

[Sny83] A. Snyder and J. Love, Optical Waveguide Theory, (Chapman and Hall, NY, 1983).

[Sou07] C. Soukoulis, S. Linden and M. Wegener, ''Negative refractive index at optical wavelengths'', Science **315**, 47 – 49 (2007).

[Sol09] L. Solymar and E. Shamonina, Waves in Metamaterials, (Oxford University Press, New York, 2009).

[Sou11] C. Soukoulis and M. Wegener, ''Past achievements and future challenges in the development of three-dimensional photonic metamaterials'', Nature Photon. **5**, 523-530 (2011).

[Str87] J. Strutt, ''On the maintenance of vibrations by forces of double frequency,

and on the propagation of waves through a medium endowed with a periodic structure'', Philosophical Magazine **24**, 145 (1887).

[Tam11] T. Taminiau, F.D. Stefani and N.F. van Hulst, ''Optical nanorod antennas modeled as cavities for dipolar emitters: evolution of sub- and super-radiant modes'', Nano Lett. **11**, 1020-1024 (2011).

[Tan74] N. Taniguchi, "On the Basic Concept of 'Nano-Technology'," Proc. Intl. Conf. Prod. Eng. Tokyo, Part II, Japan Society of Precision Engineering, (1974).

[Vas91] C. Vassallo, Optical Waveguide Concepts, (Elsevier, Amsterdam, 1991).

[Val02] P. Valanju, R. Walser and A. Valanju, ''Wave refraction in negative-index media: Always positive and very inhomogeneous'', Phys. Rev. Lett. **88**, 187401 (2002)

[Val08] J. Valentine, S. Zhang, T. Zentgraf, E. Ulin-Avila, D. Genov, G. Bartal and X. Zhang, ''Three-dimensional optical metamaterial with a negative refractive index'', Nature (London) **455**, 376 (2008).

[Ver10] L. Verslegers, P. Catrysse, Z. Yu, W. Shin, Z. Ruan and S. Fan, ''Phase front design with metallic pillar arrays'', Opt. Lett. **35**, 844 (2010).

[Ves68] V. Veselago, ''The electrodynamics of substances with simultaneously negative values of ε and μ'', Soviet Physics Uspekhi **10**, 509 (1968).

[Vuk03] P. Vukusic and J. Sambles, ''Photonic structures in biology'', Nature **424**, 852- 855 (2003).

[Vyn09] K. Vynck, D. Felbacq, E. Centeno, A. Căbuz, D. Cassagne and B. Guizal, ''All-dielectric rod-type metamaterials at optical frequencies'', Phys. Rev. Lett. **102**, 133901 (2009).

[Wan06] F. Wang and Y.R. Shen, ''General properties of local plasmons in metal nanostructures'', Phys. Rev. Lett. **97**, 206806 (2006).

[Web01] British Museum, http://www.britishmuseum.org/

[Web02] http://en.wikipedia.org/wiki/Morpho

[Wei92] T Z. Weissman and A. Hardy, ''2-D mode tapering via tapered channel waveguide segmentation'', Electron. Lett. **28**, 1514-1516 (1992).

[Wu11] C. Wu, B. Neuner III, G. Shvets, J. John, A. Milder, B. Zollars and S. Savoy, ''Large-area wide-angle spectrally selective plasmonic absorber'', Phys. Rev. B **84**, 075102 (2011).

[Wue09] S. Wuestner, A. Pusch, K. Tsakmakidis, J. Hamm and O. Hess, ''Overcoming losses with gain in a negative refractive index metamaterial'', Phys. Rev. Lett. **105**, 127401 (2010)

[Xia10] S. Xiao, V. P. Drachev, A. V. Kildishev, X. Ni, U. K. Chettiar, H. Yuan and V. M.

Shalaev, ''Loss-free and active optical negative-index metamaterials'', Nature **466**, 735-738 (2010).

[Yab87] E. Yablonovitch, ''Inhibited spontaneous emission in solid-state physics and electronics'', Phys. Rev. Lett. **58**, 2059 (1987).

[Yab91] E. Yablonovitch, T. J. Gmitter and K. M. Leung, ''Photonic band structure: the face-centered-cubic case employing nonspherical atoms'', Phys. Rev. Lett. **67**, 2295 (1991).

[Yan10] J. Yang, C. Sauvan, T. Paul, C. Rockstuhl, F. Lederer and P. Lalanne, ''Retrieving the effective parameters of metamaterials from the single interface scattering problem'', Appl. Phys. Lett. **97**, 061102 (2010).

[Yan11] J. Yang, C. Sauvan, H.T. Liu and P. Lalanne, ''Theory of fishnet negative-index optical metamaterials'', Phys. Rev. Lett. **107**, 043903 (2011).

[Yao08] J. Yao, Z. Liu, Y. Liu, Y. Wang, C. Sun, G. Bartal, A. Stacy and X. Zhang, "Optical negative refraction in bulk metamaterials", Science **321**, 930 (2008).

[Zai08] A.R. Md Zain, N.P. Johnson, M. Sorel and R.M. De La Rue, ''Ultra high quality factor one dimensional photonic crystal/photonic wire micro-cavities in silicon-on-insulator (SOI) '', Opt. Express **16**, 12084-12089 (2008).

[Zha05] S. Zhang, W. Fan, N.C. Panoiu, K.J. Malloy, R.M. Osgood and S.R.J. Brueck, ''Experimental demonstration of near-infrared negative-index metamaterials'', Phys. Rev. Lett. **95**, 137404 (2005).

[Zha06] S. Zhang, W. Fan, N.C. Panoiu, K.J. Malloy, R.M. Osgood and S.R.J. Brueck, ''Optical negative-index bulk metamaterials consisting of 2D perforated metal-dielectric stacks'', Opt. Express **14**, 6778 (2006).

[Zha11] S. Zhang, C. Xia and N. Fang, ''Broadband acoustic cloak for ultrasound waves'', Phys. Rev. Lett. **106**, 024301 (2011).

[Zho05] J. Zhou, Th. Koschny, M. Kafesaki, E. N. Economou, J. B. Pendry and C. M. Soukoulis, ''Saturation of the magnetic response of split-ring resonators at optical frequencies'', Phys. Rev. Lett. **95**, 223902 (2005)

[Zho09] J. Zhou, Th. Koschny, M. Kafesaki, and C. M. Soukoulis, ''Negative refractive index response of weakly and strongly coupled optical metamaterials'', Phys.Rev. B **80**, 035109 (2009).